The distortion of turbulence by a low Reynolds number UAV propeller and the effect on aeroacoustics

An experimental and analytical study.

Luc van Beek

MSc thesis report

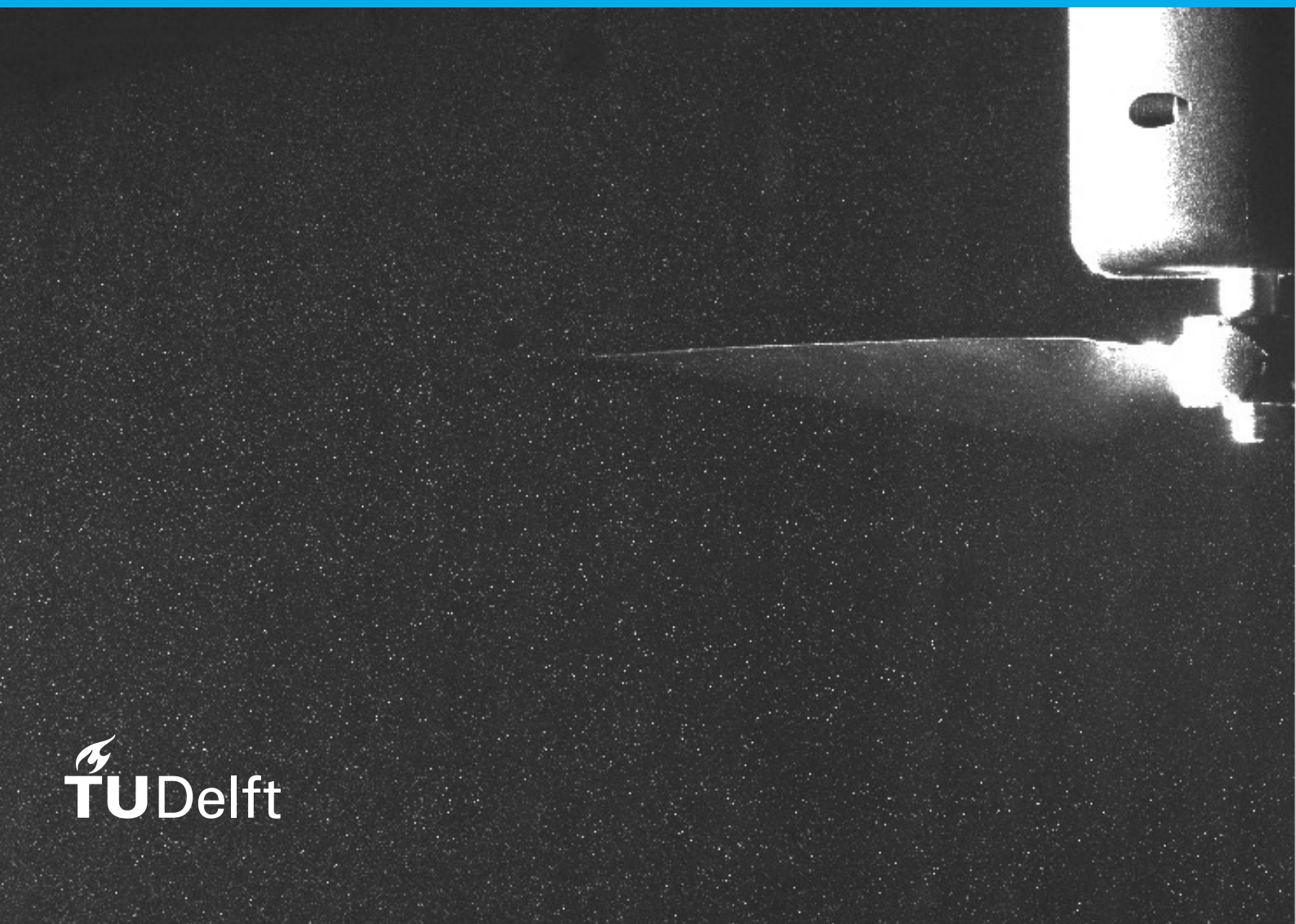

TU Delft

The distortion of turbulence by a low Reynolds number UAV propeller and the effect on aeroacoustics

An experimental and analytical study.

by

Luc van Beek

to obtain the degree of Master of Science
at the Delft University of Technology,
to be defended publicly on 14-07-2021.

Student number:	4359038	
Project duration:	June 1, 2020 – July 1, 2021	
Thesis committee:	Dr. D. Ragni,	TU Delft, chair
	Dr. F. Avallone,	TU Delft, supervisor
	Ir. E. Grande,	TU Delft, daily supervisor
	Dr. S. Hulshoff,	TU Delft, external examiner

An electronic version of this thesis is available at http://repository.tudelft.nl/.

TU Delft

Abstract

This work presents an experimental and analytical investigation of the distortion of grid generated turbulence and its relation to the aeroacoustics of a low Reynolds number propeller. The propeller has a chord based Reynolds number of $10^4 \leq Re_c \leq 10^5$ and operates at an advance ratio of 0.225. The mean flow model of Hough and Ordway ($H\&O$) is used to compute the streamtube upstream of the propeller. This allows the distortion of turbulence due to streamtube contraction to be predicted by means of Paterson and Amiet's distortion model. The distortion of turbulence by the leading edge of the blade is modelled with the asymptotic solution of Hunt. Amiet's propeller turbulence ingestion noise model is used to couple the distorted turbulence to noise. The models are validated by means of an experiment. A square bar grid with mesh size $0.1m$ and bar width $0.01m$ is placed upstream to generate turbulence. A load-torque cell measures the thrust which serves as input for the analytical mean flow model. Using particle image velocimetry (PIV) and hotwire anemometry the turbulence statistics upstream and up to the propeller plane are measured. PIV is also used to measure the distortion of turbulence by the leading edge of the propeller blade. The experiment is done in the TU Delft A-tunnel, where acoustic measurements are performed using a microphone array. Results reveal that the model of $H\&O$ overpredicts the induced velocities and a correction has to be applied such that the experimental results are matched. The analytical model and flow measurements show that the isotropic turbulence is not distorted due to the contraction of the streamtube and isotropy is conserved. The turbulence intensity and integral lengthscale do change and this is ascribed to the decay of turbulence behind a grid. Turbulence is distorted by the leading edge and an increase of the turbulent upwash velocity of 25% is observed. It is found that by using the decayed turbulence statistics, the tones at the blade passing frequency harmonics are best resembled. The correction for the distortion by the leading edge does not improve the predictions.

Nomenclature

Acronyms

eVTOL	Electrical vertical take off and landing
UAV	Unmanned aerial vehicle
BPF	Blade passing frequency
$OASPL$	Overall sound pressure level
PIV	Particle image velocimetry
PSD	Power spectral density
RDT	Rapid distortion theory
SPL	Sound pressure level

Greek symbols

β	Blade twist [°]
β_{pg}	Prandtl-Glaeurt correction [−]
η	Kolmogorov microscale [m]
$\Gamma()$	Gamma function [−]
Γ	Circulation [m^2/s]
γ	Azimuthal agnle [rad]
λ	ω/U_c [$1/m$]
μ	Dynamic viscosity [$Pa*s$]
∇	Del operator [−]
ω'	vorticity fluctuation[m^2/s]
$\omega(k,x)$	Fourier vorticity gust[−]
Ω	Rotor rotational velocity [RPM]
ω	acoustic/turbulence frequency[rad/s]
$\overline{\Omega}$	Mean vorticity [$1/s$]
Φ_{uu}	Turbulence upwash spectrum [m^5/s^2]
ρ	Air density [kg/m^3]
σ	Geometric parameter [−]
τ	Turbulence integral timescale [s]
θ	Observer angle [rad]
ξ	Distance from leading edge [−]

Roman symbols

$\mathbf{E}$	Lagrangian strain tensor [−]
$\mathbf{I}$	Identity matrix [−]
$\mathscr{L}$	Lift response function [−]
$\overline{u'}$	Mean turbulent velocity [m/s]
$\mathbf{V}$	Velocity vector [m/s]
B	Blade number [B]
b	blade semichord [m]
C	Contraction ratio [−]
c	Chord [m]
c_0	Speed of sound [m/s]
C_q	Torque coefficient [-]
C_t	Thrust coefficient [-]
D	Propeller diameter [m]
d	blade span [m]
$E(k)$	Turbulence kinetic energy [m^3/s^2]
$E^\star$	Fresnell integral [−]
f	Frequency [Hz]
J	Advance ratio [-]
J_0	Bessel function [−]

J_1	Bessel function [−]
k	Wavenumber [m^{-1}]
k_e	Largest eddy wavenumber [m^{-1}]
K_x	ω/U_c [$1/m$]
K_y	$\mu\beta^2 y/\sigma$ [$1/m$]
L	Characteristic body length [m]
L_{ij}^m	Turbulence integral lengthscale [m]
M	Mach number [-]
n	rotational frequency [Hz]
$q(k,x)$	Fourier velocity gust [−]
Q	Torque [Nm]
$Q_n()$	Legendre function [−]
R	Propeller radius [m]
r	radial location [m]
r_{le}	Leading edge radius [m]
Re_c	chordwise Reynolds number [-]
$S(k)$	Sears function [−]
S_{pp}	Power spectral density [dB/Hz]
T	Thrust [N]
T_{trace}	Streamline traceback time [s]
U_∞	Free stream velocity [m/s]
U_a	Advection velocity [m/s]
U_d	Disk velocity [m/s]
U_r	Radial velocity [m/s]
U_z	Axial velocity [m/s]

Contents

1 Introduction

1.1. Background

The use and development of unmanned aerial vehicles (UAVs) has experienced a rapid increase over the last decades and the growth is expected to continue [1]. One of the major contributions to this growth is the variety of applications for which these vehicles can be used. For example, UAVs can be used for inspection of large structures that are hard to access such as offshore windturbines and on-land oil pipelines.

UAVs can also be used for real time monitoring of traffic or for surveillance purposes [64]. Yet another application is the use of UAVs for parcel delivery. UAVs are in particular suitable to account for the first/last mile delivery which is known to be the least efficient and most expensive part of parcel delivery [15]. The UAV often needs to operate in confined areas with limited space for these applications. Therefore, the UAV has to have vertical take-off and landing (VTOL) capabilities. The most popular choice for the propulsion of UAVs to achieve this, are propellers and these are most commonly powered by electrical engines.

One of the aspects that can stall the rise of UAVs in urban areas is the noise hindrance experienced by people. For example, the FAA, although not prescribing noise levels yet, has been investigating the psychoacoustics effects of UAVs [20]. The European equivalent, EASA, has already prescribed noise level requirements [26]. Furthermore, NASA set out the Design Environment for Novel Vertical Lift Vehicles (DELIVER) to implement noise hindrance, amongst others, into a design framework.

These projects all highlight the importance of noise for eVTOL UAVs. It is therefore important to understand the mechanisms of noise generation of these rotary wing vehicles.

1.2. Problem statement

For large rotorcraft, such as helicopters, the noise generation mechanisms have been thoroughly studied [17]. The same noise generating mechanisms apply to UAV propellers. However, it is important to realise that there are fundamental differences between helicopter rotors and UAV propellers. That is, helicopter rotors typically have $0.75R$ chord Reynolds numbers, Re_c, of $\mathcal{O}(10^6)$, whereas for UAVs $10^4 < Re_c < 10^5$ [80]. Hence, both vehicles are operating in a different flow regime [65]. This indicates, for example, whether or not a laminar separation bubble is found on the blade. The acoustic spectrum changes accordingly. Similarly, high-speed impulsive noise, which is associated with transonic flow over the blade, is relevant for helicopters. UAVs will not experience transonic flow and therefore this mechanism is not important.

Another noise generating mechanism is turbulence ingestion noise, which is one of the main noise sources for helicopters [31, 39]. An UAV will undoubtedly encounter turbulence when operating in the urban environment, as shown by Murray and Anderson [51]. The source can be atmospheric turbulence, but obstacles such as trees or buildings have a turbulent wake as well, in which the UAV might operate.

Therefore, the aim of this study is to understand the flow physics associated with turbulence ingestion noise for UAVs i.e. low Reynolds number propellers. It is known that the structure of turbulence, which can be described by the turbulent kinetic energy distribution over turbulent wavenumbers, determines the emitted sound. So, it is important to accurately model the turbulence that interacts with the blade. An incoming turbulence field can be distorted by the streamtube of the rotor and by the leading edge of the rotor blade before it interacts with the blade. Both effects are studied in this thesis. The importance of both distortion mechanisms is assessed. An experimental campaign is set-up to shed more light on both mechanisms and the

results are compared with an analytical model. The scope is limited to the most generic case of an upstream isotropic spectrum.

1.3. Structure of report

This report is structured as follows: In chapter 2 the governing physics are described followed by a literature review of the state of art of turbulence ingestion noise and turbulence distortion. Following, the research objectives and research questions are posed. In chapter 3 the theoretical models are presented. Chapter 4 describes the test set-up to answer the research questions. The analytical model is analysed and the results are presented and discussed in chapter 5. The report is concluded in chapter 6 and recommendations for further study are given.

2

Literature survey

This chapter serves to introduce the various physical concepts of turbulence ingestion noise to the reader. Then, state-of-the-art research is presented. The chapter is concluded with the set of research questions.

2.1. Propeller performance metrics

Given thrust T, torque Q, propeller diameter D, freestream density ρ and n, the rotational frequency in Hz, the thrust and torque coefficients can be defined. A third quantity is the advance ratio J, which defines the ratio between the freestream U_∞ and the rotor tip speed.

$$C_T = \frac{T}{\rho n^2 D^4} \tag{2.1}$$

$$C_Q = \frac{Q}{\rho n^2 D^5} \tag{2.2}$$

$$J = \frac{U_\infty}{nD} \tag{2.3}$$

The thrust coefficient is related to loading noise and is in general a function of the propeller design, J, Mach number and Reynolds number. The freestream Mach number is the ratio of the freestream velocity divided by the speed of sound c_0. The Reynolds number symbolises the ratio of the inertial forces divided by the viscous forces. See eq. (2.4) and eq. (2.5).

$$M = \frac{U_\infty}{c_0} \tag{2.4}$$

$$Re = \frac{\rho U_\infty L}{\mu} \tag{2.5}$$

The former is a measure for the compressibility of the flow, which dictates how, for example, pressure fluctuations are propagated, see section 3.4. The latter indicates whether the flow is laminar or turbulent and governs the type of noise generating mechanisms. For example, laminar separation bubble noise only occurs at low Reynolds numbers [71, 75].

2.2. Turbulence

Turbulence is the random motion of vortical structures in rotational regions of flows [34]. These structures are referred to as vortices or eddies. Turbulence is found in the wake of bodies moving through a medium, but also in the atmospheric boundary layer.

A flow with turbulence can be characterised by the integral lengthscale L_{ij}^m, where $m \in x, y, z$ and $i.j \in W, V, U$. This is interpreted as the lengthscale in direction m of the fluctuation velocity components i, j. Hence, the streamwise longitudinal lengthscale is denoted as L_{uu}^z. See fig. 3.3 for the coordinate system used in this thesis.

The integral timescale of these structures is related to the lengthscale as $\tau = \frac{L^m_{ii}}{U_a}$, where U_a is the advective velocity. This relation holds only if frozen turbulence assumption is valid, which is typically the case if the turbulence intensity < 10% [34, 76]. The eddies of size L^m_{ij} break down into smaller structures until molecular viscosity becomes important. The smallest scale, η_i, is called the Kolmogorov microscale. In this way, the energy of the largest structures is eventually dissipated into heat in a process called energy cascade.

The aforementioned turbulence intensity is another statistical quantity describing turbulence. It is defined as the mean velocity fluctuation in a certain flow direction divided by the mean flow velocity. Hence, in the z-direction this is $\frac{\overline{u'}}{U_a}$. Together with the integral lengthscale, the intensity is one of the key parameters to describe a turbulence field.

A turbulence field is said to be isotropic if the turbulence intensities are equal in all three three directions. Isotropic turbulence implies the following relation for the integral length scale $L^z_{vv} = L^z_{ww} = L^z_{uu}/2$. For the microscales it implies $\eta_x = \eta_y = \eta_z/\sqrt{2}$. Furthermore, the ratio $\frac{L^x_{vv}}{L^z_{uu}}$ is unity [30]. Homogeneity means that the turbulence characteristics remain the same under arbitrary translations of the coordinate axis.

Von Kármán [47] derived a semi-empirical relationship for the energy spectrum function $E(k)$, see eq. (2.6), which gives the kinetic turbulent energy as a function of turbulent wavenumber. This holds for a homogeneous turbulence field.

$$E(k) = \frac{55}{9\sqrt{\pi}} \frac{\Gamma(5/6)}{\Gamma(1/3)} \frac{\overline{u'}^2}{k_e} \frac{(k/k_e)^4}{[1+(k/k_e)^2]^{17/6}} \tag{2.6}$$

Here $\Gamma()$ is the Gamma function and the wavenumber of the largest eddies, k_e, is defined as

$$k_e = \frac{\sqrt{\pi}}{L^z_{uu}} \frac{\Gamma(5/6)}{\Gamma(1/3)} \tag{2.7}$$

The turbulence integral lengthscale and turbulence intensity are the parameters that determine the shape of the energy function. So, through these two variables it is possible to define a turbulence spectrum. The effect of each of these variables is depicted in fig. 2.1. Clearly, the whole spectrum shifts up i.e. more energy over all wavenumbers if the intensity is increased. Decreasing the lengthscale increases the energy contained in the higher wavenumber range. The Von Kármán spectrum accurately describes turbulence spectra in boundary layers and wakes as well as behind turbulence generating grids [34, 60].

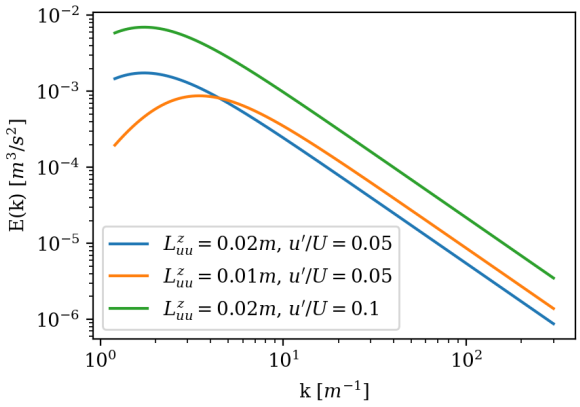

Figure 2.1: Von Karman energy spectrum for various combinations of lengthscale L^z_{uu} and mean intensity $\overline{u'}$ as function of turbulence wavenumber k. Mean flow velocity $U_\infty = 10m/s$.

In 1938 Taylor stated "If the velocity of the air stream which carries the eddies is very much greater than the turbulent velocity, one may assume that the sequence of changes in u at the fixed point are simply due to the passage of an unchanging pattern of turbulent motion over the point.. "(Taylor [72], p478). This implies that the eddies do not increase the velocity by which they are advected. This is only reasonable accurate for fluctuations much smaller than the advection velocity $\frac{\overline{u'}}{U_a} << 1$. This is referred to as Taylor's frozen hypothesis. Using this hypothesis, the integral time- and lengthscale are related through the local velocity of the flow at which the eddies are moving.

2.2.1. Turbulence distortion

Turbulence distortion is of importance in the modelling of turbulence ingestion noise as it alters the incoming turbulence spectrum and hence affects the unsteady loading, see section 2.3. Turbulence distortion in the case of rotors happens due to the contraction/expansion of the streamtube depending on the operating condition [37]. For propellers, the flow is accelerated and the upstream streamtube contracts. This stretches the turbulent structures and changes their characteristics [50]. See fig. 2.2 for the representation of this process. Generally, the change of turbulent eddies is accounted for using Rapid Distortion Theory (RDT). The following is assumed in RDT, as described by Hunt [43].

- $\frac{\overline{u'}}{U_\infty} << 1$,
- $\frac{\overline{u'}D}{U_a L^z_{uu}} \leq 1$

The first is Taylor's frozen hypothesis. That is, eddies are advected with the mean flow and do not change it. This is necessary to linearise the governing equations which serve as a basis for RDT. It also means that the turbulence velocities do not transport the eddies. The second requirement states that the eddy turnover time must be larger than timescale of the distortion. In other words, the eddy cannot be dissipated before the distortion has happened. It has to be 'rapid'.

The distortion of turbulence can have two origins. One is the change in mean flow streamlines caused by a body, which will turn and stretch the turbulent eddies. The other mechanism is the blocking effect of a body. This effect forces velocities on the surface to be zero and in order to conserve momentum, the velocities parallel to the blocking surface must increase. Hence, the eddies are distorted. A more detailed explanation is found in section 3.3.

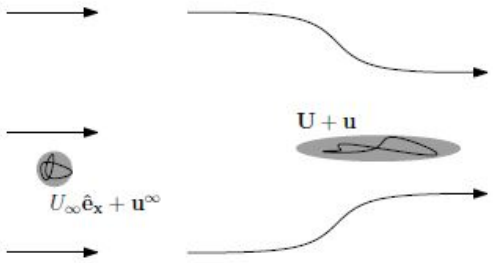

Figure 2.2: Graphical representation of the stretching of a turbulent eddy by streamtube contraction [23]. U_∞ and $\mathbf{u}^\infty$ denote the upstream axial and turbulent velocity, respectively. **U** and **u** represent the mean flow and turbulent velocity near the rotor, respectively.

2.3. Turbulence and loading noise

Turbulence is the unsteady random motion of vortical structures, as mentioned in section 2.2. Suppose such a structure is approaching an airfoil as in fig. 2.3. As the airfoil is approached, the angle of attack of the airfoil is changed due to the induced velocity . This changes the pressure distribution over the airfoil, which is observed as noise.

In this way, the incoming turbulence is related to noise. Since turbulence is per definition an unsteady phenomenon, it is a source of unsteady loading noise meaning it acts as a dipole. Depending on the operating conditions of the propeller and the characteristics of the turbulence spectrum, either broadband noise, tonal noise or a combination of the two is observed.

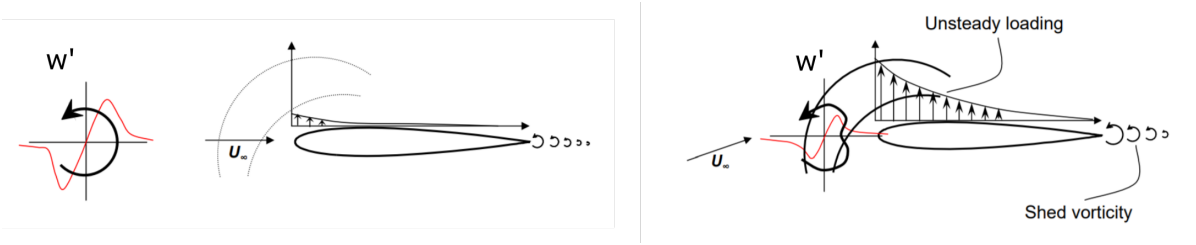

Figure 2.3: A turbulent eddy gives rise to an upwash velocity. As the eddy reaches the leading edge, the upwash changes the angle of attack which in turn changes the lift and drag forces. The pressure change is directly propagated as sound. This figure is a modified version. Original version obtained from [69]

An important phenomenon observed in rotor turbulence interaction noise is haystacking [34]. Eddies of a certain size can be cut by more than one propeller blade when advecting through the propeller plane. Then, the same unsteady velocity fluctuation is seen by multiple blades. This is referred to as unsteady loading blade-to-blade coherence. An eddy is cut at the blade passing frequency (BPF). Since the response of the blades to this fluctuation is the same, the observed spectrum will not be strictly broadband anymore but will show tonal peaks at multiples of the BPF. The process of acoustic energy centring at the BPF harmonics because a single eddy is cut multiple times is called haystacking and is depicted in fig. 2.4. A time signal and spectrum for a small and large eddy are depicted in fig. 2.5. It can be seen that the larger eddy interacts more often with the blades. Subsequently, the energy is centred around the BPFs.

The coherence between the loading of the blades depends on the operating condition and on the upstream turbulence spectrum. The first one is characterised by J. Typically, a lower advance ratio leads to a larger streamtube contraction and vice versa. In turn, a larger contraction leads to more elongation of the eddies. This increases the blade-to-blade coherence. This distortion process is described in more detail in section 3.3.

Even when the turbulence is not distorted, the blade-to-blade coherence can be large. The size of the eddies upstream can be sufficiently large such that a single eddy interacts with multiple blades [32, 33]. An estimation of the turbulent frequency above which no coherence is found is given by eq. (2.8).

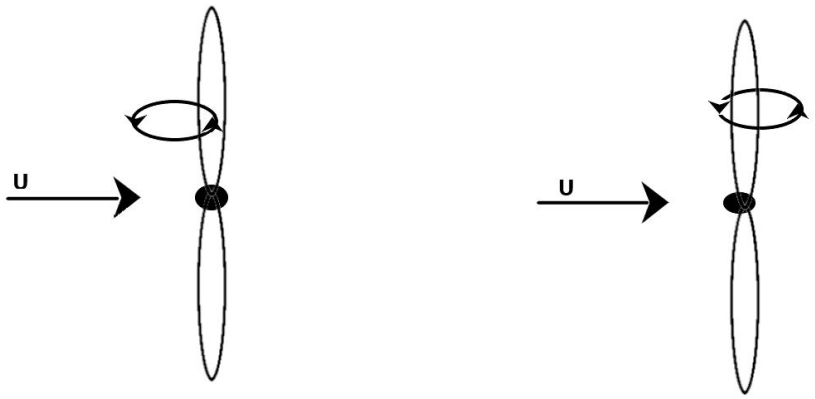

Figure 2.4: An eddy is convected with mean velocity U and is cut at $t = 0$ on the left. At $t = t'$ the blade has rotated and is still cutting the same eddy. This leads to coherence in unsteady loading, and results in haystacking.

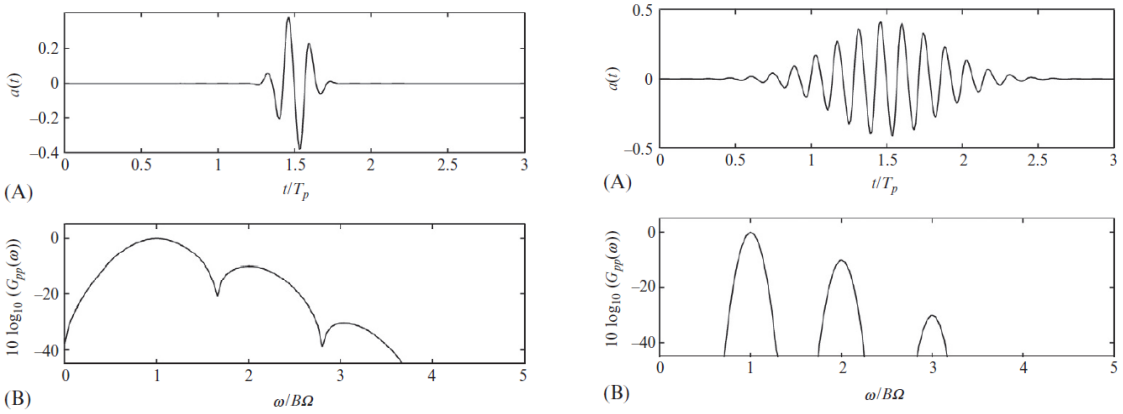

Figure 2.5: Time signal and spectra from interactions of rotor blade with (a) a small eddy (b) a large eddy. A larger eddy leads to more blade interactions, albeit with a changing amplitude. Hence, the centring of energy around the BPFs is observed. Retrieved from Aeroacoustics of Low Mach Number Flows [34].

2.3.1. Broadband noise

The broadband part of turbulence interaction noise is caused by turbulent structures which are interacting only once with the propeller blades. An estimation of turbulent frequency above which broadband noise is expected is given by eq. (2.8).

$$f = \frac{\Omega B(1 + M_0/M_a)}{2(1 - M_0 cos(\theta)} \tag{2.8}$$

Here, Ω is the rotational velocity of the rotor in rad/s, B is blade number, M_0 and M_a are the turbulence rotational and advective Mach numbers respectively and θ is the angle of the observer with respect to the rotor plane [33].

2.4. State of the art

Sevik [63] was one of the first to investigate the effect of turbulence on the unsteady loading noise of a propeller. A 10-bladed open-rotor was subjected to a stream with grid generated turbulence. At multiples of the blade passing frequency humps in the spectrum were observed which could not be explained for homogeneous and isotropic turbulence. Sevik posed the hypothesis that these humps are caused by blade-to-blade coherence of unsteady loading and referred to this phenomenon as haystacking. This effect is depicted in fig. 2.6. It follows that the unsteady loading, and therefore the turbulence, has been modelled incorrectly.

In his model Sevik assumed the chord to be acoustically compact. For an integral lengthscale L^z_{uu} of at most $10.16cm$ (derived from mesh size, see Roach [57]), the $2.54cm$ chord can not be assumed acoustically compact. Together with the incorrect turbulence model, it can explain the observed discrepancy between experiment and theory.

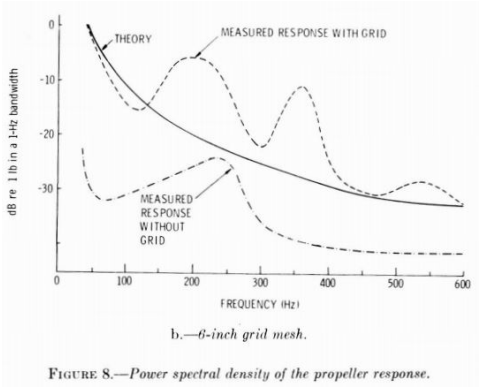

Figure 2.6: Results from Sevik [63]. Humps in the spectrum were observed while these were not expected

Hanson [40] argues that the haystacking was caused by the elongation of turbulent eddies. The elongation of turbulent structures is, in the case of propellers, rotors and fans, caused by the contraction of a streamtube. An elongated eddy will interact more often with the blades, leading to a coherence in unsteady loading of the blades. Hanson's research focused on examining how the turbulence characteristics are related to the features of the narrow-band noise spectra. The experimental results showed that the elongation of turbulent structures inside a rotor fan is significant with the ratio of streamwise to transverse lengthscale of $\frac{L^z_{uu}}{L^z_{vv}} = 400$, see fig. 2.7. This illustrated that the incoming, close to isotropic, atmospheric turbulence field was heavily distorted and consequently became anisotropic.

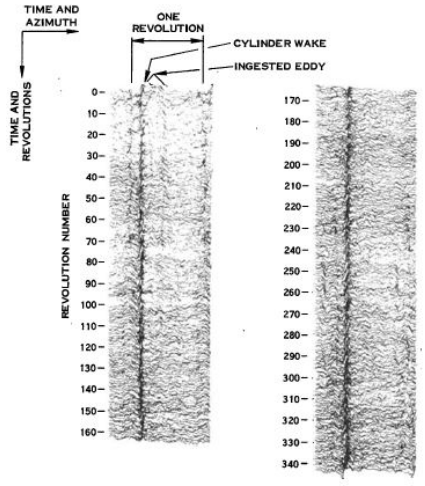

FIG. 12. Inlet distortion history using blade pressure signals.

Figure 2.7: Result from Hanson[40] where the black line illustrates an elongated eddy interacting with the rotor for a significant amount of revolutions

Aravamudan and Harris [11] performed experiments with a $1.27m$ diameter helicopter rotor inside an anechoic windtunnel where two turbulence generating grids were installed, each giving a different integral length scale. The intensity of the turbulence was increased from 1.7% for the clean inflow conditions to 11.0% and 6.25% with the grids installed. Their research focused on the broadband part of the noise spectrum caused by turbulence. This essentially boils down to the part of the incoming turbulence spectrum which would not lead to blade-to-blade coherence. It was found that the low-frequency (ranging up to $2000Hz$) broadband noise intensity depends on the rotor-tip velocity scaling with M^4_{tip}. The low-frequency noise peak intensity scaled with the streamwise turbulence integral lengthscale as $(L^z_{uu})^{-.33}$. A numerical reasoning was presented to assess the influence of turbulence intensity. Indeed, with increasing intensity, the noise increases as well with $\overline{u'}^2$, but this was not verified with experiments.

Hagen et al. [39] investigated the effect of ingesting atmospheric turbulence into an isolated tail rotor of a helicopter. By correlating upstream turbulence to the turbulence experienced by the rotor they found that the maximum stretching ratio of the eddies in streamwise direction is approximately nine. This indicates anisotropic turbulence. Interestingly, they did not measure an increased overall sound pressure level when the upstream integral length was increased. They speculate that above a certain eddy length, leading to a certain number of successive chops by the blade, the coherence will not increase significantly any more. It is said that this threshold is around 80 chops for an eddy. Turbulence intensity was varied during the experiments as well. It was found that the peaks of the of the spectrum increased at the lower blade passing frequency harmonics and remained the same at higher harmonics. The broadband floor raised across the whole spectrum. For the lower frequencies (up to $1000Hz$) this increase was $2dB$. The broadband floor of the high frequencies ($1000Hz$ to $3000Hz$) rose with $5dB$.

Small scale turbulence was added to the atmospheric turbulence by means of a grid. The atmospheric turbulence intensity was equal to 5%. The authors explicitly state that no measurements are available with the grid in the flow. Nevertheless, the size of the eddies resulting from the grid can be estimated. That is, the size will be comparable to the mesh size of the grid which was $7.6cm$. Hence, the ratio of lengthscale to rotor diameter equals $\frac{L^z_{uu}}{D} = \frac{7.6}{223} \approx 0.035$. Since the grid adds small turbulent structures with respect to the rotor diameter most effect is observed in the higher frequency range, as can be seen in fig. 2.9. The small eddies are

interacting with the blade with little or no coherence between the blades. These gave rise to the broadband floor of the sound spectrum.

In fig. 2.10 the effect of thrust on the noise spectrum is depicted. It was found that as the thrust increases by changing the pitch, the noise increases as well. This opposed the authors expectations as it was assumed that the mean loading, and therefore thrust, does not influence turbulence ingestion noise. However, the authors fail to address the fact that by increasing the blade loading, the steady tonal component of the spectrum is increased. This might explain the observed differences. Furthermore, the blade is operating under different conditions and an increase in blade-self noise might be observed. For example, stall noise. This effect can account for the increase in the broadband part of the spectrum.

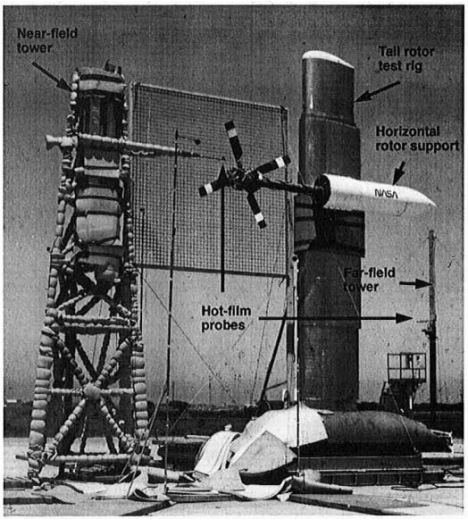

Figure 2.8: Test setup of experiment with turbulence grid installed, as presented by Hagen et al. [39].

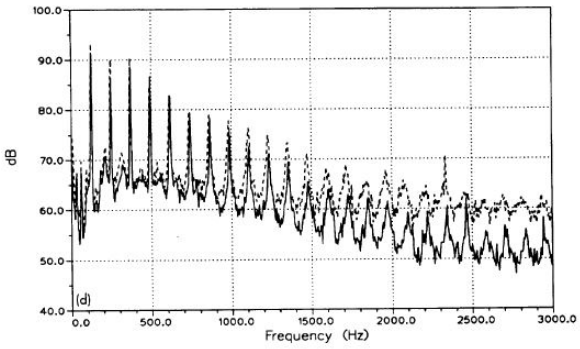

Figure 2.9: Acoustic measurements with (dotted line) and without (solid line) grid installed, as presented by Hagen et al. [39].

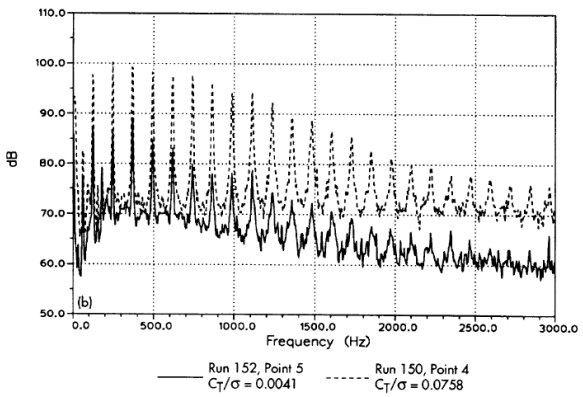

Figure 2.10: The effect of thrust on the noise spectrum [39].

Paterson and Amiet [55] set out an elaborate experimental campaign to obtain noise data of a model helicopter rotor with turbulence ingested. The model rotor was first subjected to isotropic turbulence which was generated by a grid inside a wind tunnel. Both vertical ascent and forward flight manoeuvres were simulated in the wind tunnel by varying the windtunnel speed from $8m/s$ to $23m/s$, respectively, whilst maintaining the rotor rotational velocity $\Omega = 360RPM$. The effect of turbulence for the rotor in ascent became visible above the second harmonic of the blade passing frequency. There the spectrum rapidly transforms into a smooth broadband type for a smooth inflow. However, the spectrum with turbulence ingested remains quasi-tonal up to the 20^{th} harmonic ($5000Hz$). Additionally, the noise level is approximately $10dB$ higher for frequencies above the second harmonic indicating the importance of turbulence ingestion noise.

Moreover, the turbulence intensity was varied and it was found that the noise increases as the intensity increases. The test conditions while varying the intensity were the same, except the tip speed which was

changed with a factor 1.1. As the inflow became increasingly non-axial, i.e. the forward flight case, it was observed that the tonal characteristic of the spectrum was damped.

Physically, this is a result of the azimuthal drift of an inflowing eddy leading to blade chops at irregular time intervals. The drift reduces the blade-to-blade coherence of unsteady loading, hence a less tonal spectrum. On the other hand, the half harmonics of the BPF were found to increase and this was ascribed to the drift phenomenon. The effect of blade pitch was investigated as well. Only a minor effect was observed. The small differences were ascribed to the change of noise directivity while the microphones remained fixed. Note that these findings oppose the ones of Hagen et al. who observed a significant increase in the amplitude of the tonal components after changing the pitch.

Paterson and Amiet do not mention the effect of pitch on distortion. Changing the pitch of an airfoil will affect the streamlines, both the mean flow streamlines which define the streamtube as well as the streamlines in airfoil frame of reference. In turn, the distortion process is affected. This might explain the differences.

Scharpf and Mueller [61] investigated the effect of turbulence on a marine propeller using a wind-tunnel setup. The authors expected to measure the stretching of eddies, but they did not found any evidence of this process. At least, not at $6 inches (\approx 15.2 cm)$ in front of the rotor where the measurements were taken. It was argued that the stretching occurs closer to the rotor. The grids used in the experiment generated turbulence fields with similar integral length scales but a varying intensity. It was found that the increased intensity gives rise to an increase in sound power level, as consistent with Paterson and Amiet [55]. The sound spectra were predominantly of broadband nature.

No significant eddy stretching was observed, even not at just $15 cm$ in front of the rotor. Additionally, the integral length scale characterising the turbulence was around $0.34 inches$ or $0.86 cm$. The ratio $\frac{L^z_{uu}}{D} = \frac{0.34 inch}{10 inch} = 0.034 < 0.1$, is considered to be small [45] , although no real consensus regarding the terminology is found in literature. Little blade-to-blade coherence is found as a single eddy will only interact with one blade as it advects through the rotor plane. Therefore, these small eddies appear as random fluctuations to the blade, which results in a broadband spectrum.

Up till now it has become evident that turbulent eddies can be distorted when approaching a rotor. The stretching of turbulent eddies leads to more blade to blade coherence. Its implication can be significant, for example the dependence of acoustic energy on the intensity as found by Scharpf and Mueller [61] and Paterson and Amiet [55]. Or the occurrence of haystacks, as described by Sevik [63].

2.4.1. Experiments related to UAV propellers

To the best of the author's knowledge only three experiments have been performed that characterise the effect of turbulence ingestion on small-scale UAV propellers. Yauwenas et al. [77] conducted an experiment where a propeller with a diameter of $30 cm$ was subjected to a grid-generated turbulence field. Additionally, the propeller was submerged in the wake of a cylinder shedding periodic vortices. The resulting spectra are presented in fig. 2.11. It was observed that the tones at BPF 1 and BPF 2 remain unaffected by the turbulence. However, the spectra of the flow with the cylinder wake had significantly more power at the third and fourth harmonic. It was concluded that the wake of the cylinder lead to unsteady impulsive loads. The effect of the turbulence grid is evident from BPF 10 to BPF 20 ($3000 Hz$ to $6000 Hz$). Here, increased tonal behaviour was observed when compared to the clean inflow conditions. The effect of the flow disturbances becomes evident from the right picture in fig. 2.11 where the phase-averaged waveform is presented.

The second experiment was performed by Stephenson et al. [70]. Their experiment focused on showing the effect of flow recirculation inside a closed anechoic chamber. The resemblance of the experiments for small scale UAV propellers experiencing turbulent inflow noise is quite remarkable though. A 9.4 $inch$ ($\approx 23.8 cm$) diameter propeller was put inside an anechoic chamber and noise spectra were obtained before and after the recirculation had established. Although the detailed characteristics of the flow were not measured, it is for sure that the reingested flow is turbulent. The effect of recirculation and thereby turbulence ingestion is depicted in fig. 2.12. The first blade passing harmonic appeared unaffected by the recirculation for all three microphones. The largest differences were observed for the out of plane microphones, which indicates the increase in loading noise which is ascribed to turbulence ingestion. Differences as large as $30 dB$ are observed at higher harmonics and the overall trend shows an increase in noise level. This effect is less, although still present, for the in plane microphone.

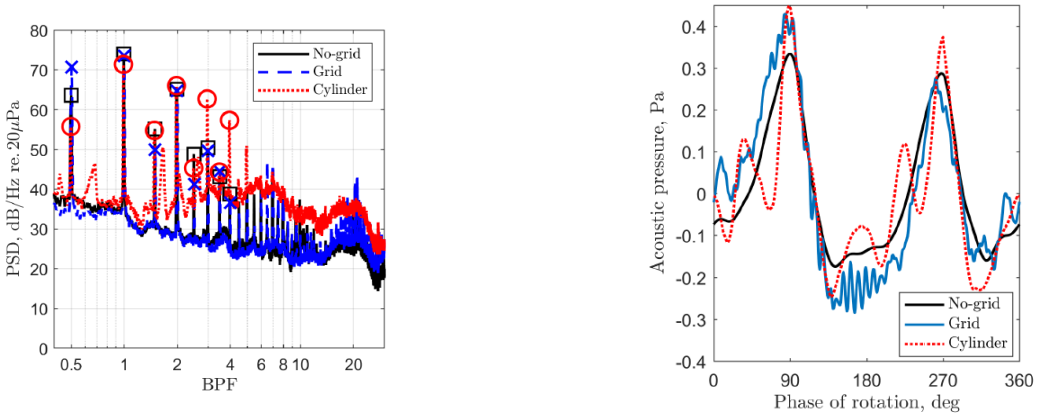

(a) (b)

Figure 2.11: (a) Farfield PSD and (b) phase-averaged waveform for the various inflow conditions as retrieved from [77]. ◯ indicates the cylinder inflow disturbance, □ the grid and × the clean inflow. Tested at a freestream velocity of $20 m/s$ and $9000 RPM$

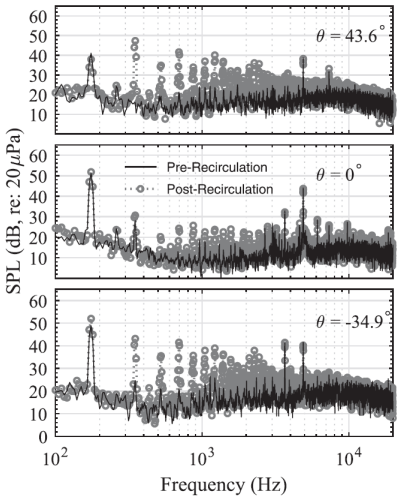

Figure 2.12: Spectra before and after circulation for measurements in front (top), in (middle) and behind (bottom) the rotor plane. From Stephenson et al. [70].

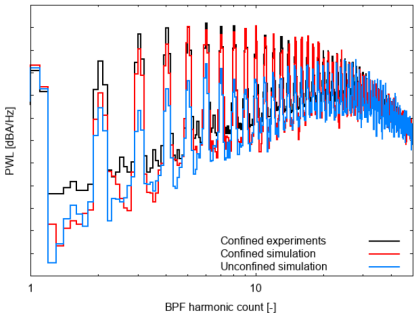

Figure 2.13: PWL spectrum for the simulation with(out) recirculation and experiment [52]. The y-axis tics are 5dBA/Hz apart.

Similar results were obtained by Nardari et al. [52]. An UAV propeller was operated in an anechoic chamber with $Re_c = 2.6 * 10^5$. This value lies within the range of relevant Reynolds numbers that was specified previously. Along with the experiment a numerical effort was undertaken to investigate the effect of recirculation. Figure 2.13 shows the comparison of the simulations and the experiment. The tone at the first harmonic is caused by steady loading and does not vary. It is observed that between the BPF 2 and BPF 30 the effect of recirculation is large. The increase in noise level is ascribed to unsteady loading, hence turbulent inflow. It is interesting that the range of relevant BPF harmonics caused by turbulence has close resemblance with what was observed by Yauwenas et al. [77] and also with Paterson and Amiet [55, 77]. In fig. 2.13 no experimental result of the PWL spectrum before recirculation is presented, but the simulations predict a significant contribution to the noise, as what was found by Stephenson et al. [70] and Paterson and Amiet [55]. Namely, that the contribution of blade self-noise is said to become the dominant noise source from BPF 30 onward.

2.4.2. Turbulence Distortion

Simonich et al. [66] and Amiet et al. [9] presented a model that is able to account for the effect of distortion in the noise prediction. An upper limit for the size of distorted eddies is defined by the rotor diameter. The lower limit is defined by the blade thickness. Their theory predicts the ingestion noise to be relevant

for frequencies up to the 30^{th} harmonic of the BPF after which self noise becomes more important. This is consistent with the previously presented experimental results. The theory predicts higher noise levels when a streamtube expands and the eddies are compressed. This leads to a higher upwash velocity as experienced by the blade. The same conclusion was drawn by Batchelor and Proudman in their early work on turbulence deformation [14]. The compression also tends to broaden the peaks. This is a result of the decreased likeliness of an eddy being chopped by multiple blades. Conversely, when eddies are elongated by streamtube contraction, the peaks are expected to become narrower and due to a lower upwash velocity the overall noise reduces. This is illustrated in fig. 2.14. Here, it becomes evident that an elongation of the eddies (streamtube contraction, contraction ratio $C > 1$) leads to an attenuation of the overall sound pressure level and a more peaked spectrum.

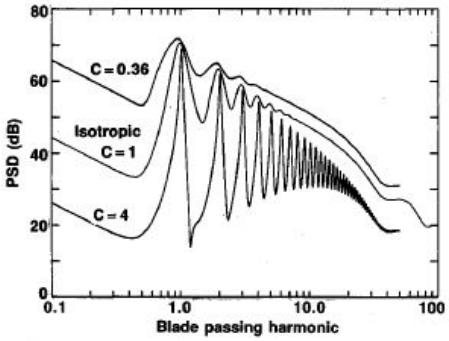

Fig. 10 Superposition of Figs. 7–9.

(a)

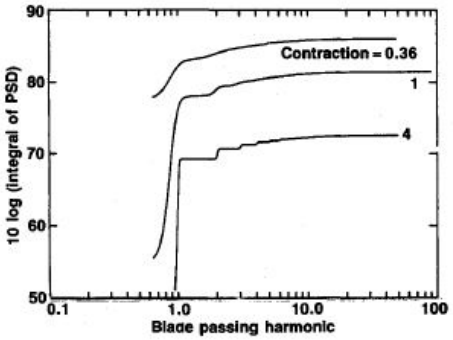

Fig. 11 Acoustic energies of Figs. 7–9.

(b)

Figure 2.14: Effect of streamtube contraction on the acoustics (a) PSD (b) acoustic energy. The turbulence spectrum used in teh model was intitially isotropic. C denotes the contraction ratio. Figure was presented by Amiet et al. [9].

Turbulence can also be distorted due to the presence of a body. More specifically, due to the leading edge of an airfoil. De Santana et al. [60] investigated the interaction of turbulence with a NACA-0012 airfoil. Using stereo PIV the turbulence intensity in front of the leading edge was extracted. A case study was performed for the case of large turbulence with respect to the leading edge radius, $\frac{L^z_{uu}}{r_{le}} \approx 10$. The results are presented in fig. 2.15. Here, $\xi = \frac{x}{r_{le}}$ represents the non-dimensional distance in front of the leading edge. Clearly, the upwash component w', which generates the unsteady loading, starts increasing from $\xi = 4$. This is an important result since it suggests that the upstream turbulence intensity does not correctly represent the upwash fluctuations which interact with the airfoil.

The trend of the increasing upwash velocity fluctuation is in line with Hunt's asymptotic theory [44]. However, the same theory states that the streamwise fluctuation u' should decrease, which it does not. This observation is not addressed in the paper.

The authors combined the intensity measurements with a modified Von Kármán spectrum to obtain a better prediction of noise. The correction accounts for the decrease of upwash intensity at high frequency. In fig. 2.16 it can be seen how the rapid distortion affects the sound prediction. Both the spectrum shape and amplitudes have better agreement with the experimental results if rapid distortion is modelled. Especially, for $1 \leq kc \leq 2$. For the modified model it can be seen that for $kc > 2$ the noise is over predicted by $\approx 5dB$. This is an improvement with respect to the original model, which overpredicts up to $20dB$ in that range.

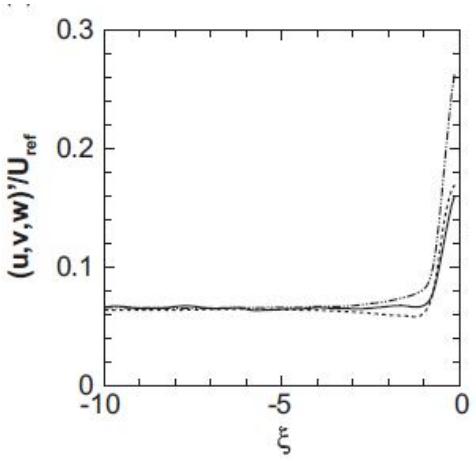

Figure 2.15: Intensity measured upstream of leading edge, u' (plain line, streamwise velocity), v' (dashed line, transverse velocity), w' (dash dot dot line, normal velocity) as function of Ξ

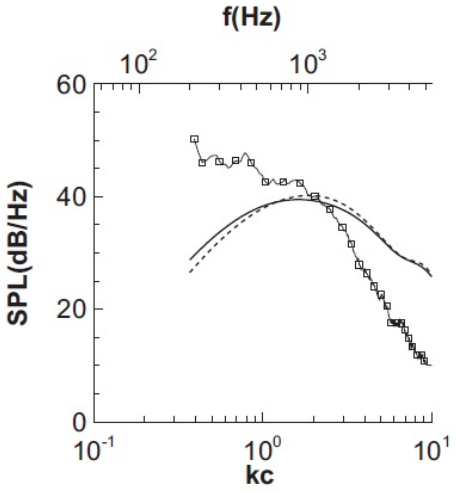

(a) Original Amiet model for leading edge noise. Squares represent experimental results. Plain line with leading edge scatter term. Dashed line also includes a trailing edge scatter term.

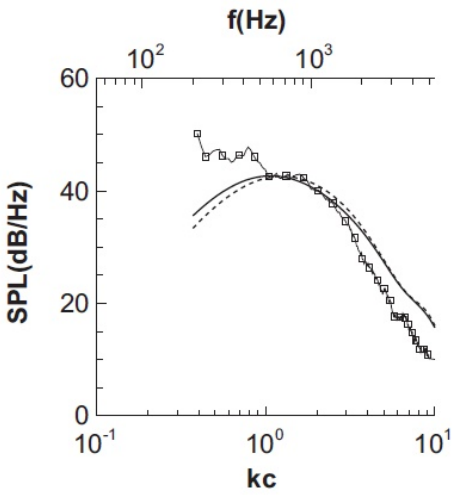

(b) Rapid distortion modified model for leading edge noise. Squares represent experimental results. Plain line with leading edge scatter term. Dashed line also includes a trailing edge scatter term. Same experimental results as in fig. 2.16a

Figure 2.16: Comparison of spectra resulting original model and distortion modified model [60].

2.5. Summary

Turbulence ingestion noise has been researched extensively for helicopters, fans and marine propellers. Both experimentally and analytically. Hanson [40] and Hagen et al. [39] amongst others have found that a given turbulence field can be distorted by the propeller induced flow field. The flowfield stretches the turbulence in streamwise direction thereby elongating the eddies. However, it does depend on operating conditions, for example Scharpf and Mueller [61] did not measure a significant stretching of the turbulence.

The distortion of turbulence can lead to a more tonal noise spectrum, as found by Sevik [63]. That is, elongated eddies cause coherence in the blade loading and observed noise. However, the size of eddies is also important. Small eddies, of order blade chord, tend to increase the broadband component of the noise in the higher frequency regions, as found by Hagen et al.[39].

Turbulence ingestion noise is the dominant noise source up to the 30^{th} BPF. This was found experimentally by Nardari et al. [52]. Factors that affect the noise are the turbulence intensity and integral lengthscale. The noise scales quadratically with the former, as found by Aravamudan and Harris [11] and Hagen et al. [39]. Turbulence integral lengthscale is found to affect the noise as $(L^z_{uu})^{-0.33}$.

It has become evident how turbulence distortion prior to the rotor affects the noise by stretching and

turning of eddies. However, De Santana [60] showed that distortion of turbulence caused by the presence of a body can have a large influence on the noise spectrum as well. As far as the authors' knowledge, this effect has not been studied for UAV propellers.

2.6. Research goals and question

From the previous sections it became clear how noise is generated when turbulence interacts with a helicopter rotor or propeller. Moreover, it was found that the streamtube deforms the incoming eddies and affects the resulting noise spectrum. The deformation process is described by rapid distortion theory. However, a more detailed investigation into the rapid distortion of turbulence showed that turbulence can also be distorted due to the presence of a bluff body i.e. a leading edge.

To shed more light on the importance of these distortion mechanisms and their relation to acoustics, the following research questions are answered in this thesis.

1. What is the distortion of an upstream isotropic turbulence spectrum due to the contracting streamtube as the turbulence approaches a low Reynolds number propeller in low speed forward flight?
    - What is the degree of isotropy at the rotor face? *Isotropy implies that the ratio of streamwise to traverse velocity fluctuations is unity. Downstream anisotropy means that this ratio has changed. This does not happen when turbulence decays naturally in the flow. Hence, it can be deduced that turbulence has been distorted.*
    - What is the change of the streamwise turbulence intensity at the rotor face compared to the upstream turbulence intensity? *The streamwise component is the main component of the upwash fluctuations in the blade frame of reference. A change of this component yields a change in observed sound.*
2. Does the neglecting of leading edge distortion in the analytical model lead to large discrepancies in the computed and observed noise?
    - How does the intensity of the turbulence upwash component evolve as it approaches the leading edge? *This is the main indicator if leading edge distortion is relevant as it governs the emitted noise.*
    - Can the difference in the observed noise be ascribed to the neglecting of the leading edge distortion? *This sheds light on the relevance of leading edge distortion in the analytical model.*

3

Analytical model

The goal of this chapter is to describe the various analytical models used in this thesis. In fig. 3.1 the various components of the complete model are depicted. First, the mean flow model is described in section 3.1. Then, the analytical far-field noise model is presented in section 3.2. After which the theoretical foundations of the distortion mechanisms are presented, see section 3.3. Lastly, in section 3.4 the lift response functions are briefly explained. In fig. 3.1 the relation of the various models with respect to each other are depicted.

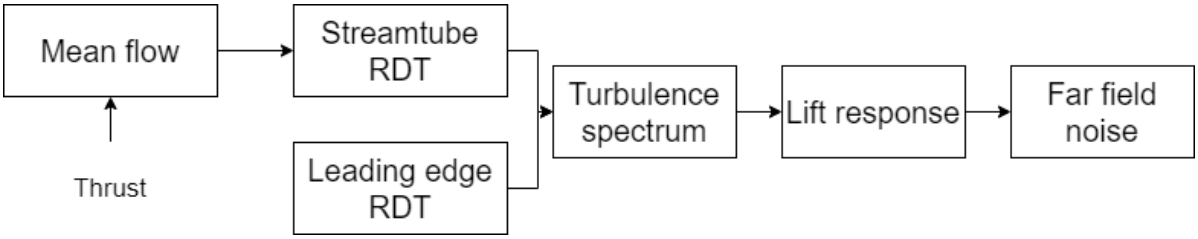

Figure 3.1: Various components of the analytical model. Thrust follows from experiment.

3.1. Mean flow model

In order to have a fully analytical model to compute the noise, it is necessary to include a mean flow model. The reason is that the mean flow in front of the propeller governs the distortion of turbulence before it interacts with the blade. For this distortion mechanism, only the flow upstream is needed and not the details of the flow around the blade. Therefore, a relatively simple actuator disk model developed by Hough and Ordway [42] is used. It has been shown by Yin et al. [78] that such a model can accurately predict the mean flow, at least to the same extend as an unsteady Reynolds Averaged Navier Stokes (uRANS) simulation.

3.1.1. Variable circulation along the actuator disk

The actuator disk is an infinitesimal thin surface where flow discontinuities exist due to the exertion of a force on the flow by a propeller or rotor. The disk might be viewed as a propeller or rotor with an infinite number of blades. Hence, such a model represents the steady forces only and can therefore be used to determine the mean flow.

By defining the circulation as function of radial position, $\Gamma(r)$, the information of each blade section is taken into account. In other words, by allowing the circulation to vary, the blade shape and chord information are implicitly modelled. Hough and Ordway [42] represented a blade by a distribution of circulation. Additionally, a sheet of trailing vortices $-\frac{d\Gamma}{dr}$ is shed as the flow moves with respect to the propeller, see fig. 3.2a. The Biot-Savart law is used to determine the velocities induced by the system of vortices which states that the induced velocity vector equals

$$\mathbf{dV} = \frac{\Gamma}{4\pi}\frac{\mathbf{dl}\times\mathbf{r}}{|\mathbf{r^3}|}, \tag{3.1}$$

where $\mathbf{r}$ equals the distance to an arbitrary point P from a filament of length $\mathbf{dl}$. See fig. 3.2b.

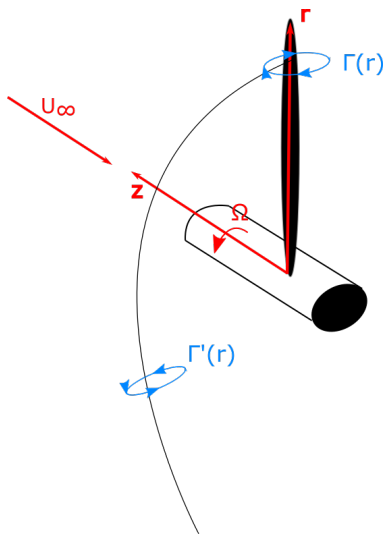

(a)

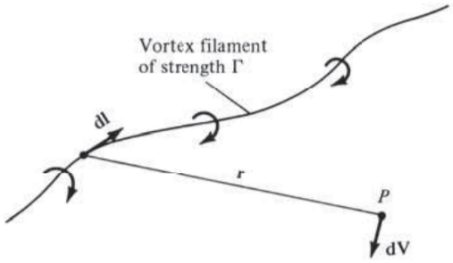

(b)

Figure 3.2: Representation of (a) the Hough and Ordway model and (b) the law of induction.

The function which describes the variable circulation is given as

$$\Gamma(r) = \frac{105}{16}\frac{\pi U_\infty U_d}{B\Omega}\frac{r}{R}\sqrt{1-\frac{r}{R}} \tag{3.2}$$

and differentiating with respect to r yields

$$\Gamma'(r) = \frac{105}{16}\frac{\pi U_\infty U_d}{B\Omega}\frac{1-\frac{3r}{R}}{R\sqrt{1-\frac{r}{R}}}. \tag{3.3}$$

Here, R denotes the total rotor radius, B the number of blades and Ω the rotational speed. Finally, the disk velocity is defined in eq. (3.4).

$$U_d = \frac{T}{\pi R^2 \rho_0 U_\infty} \tag{3.4}$$

It couples the total propeller (or actuator disk) thrust to the circulation. The above form for the circulation matches closely the optimal distribution for minimum energy loss in the wake as defined by Goldstein [35]. Then the upstream induced axial and radial velocities at location (z, r) are given by eq. (3.5) and eq. (3.6).

$$U_{z,induced}(z,r) = \frac{105}{32}\frac{-U_d z}{2\pi r^{3/2}}\int_0^R \frac{\sqrt{r'}}{R}\sqrt{1-\frac{r'}{R}}Q'_{-\frac{1}{2}}(\omega')dr', \quad >0 \tag{3.5}$$

$$U_{r,induced}(z,r) = \frac{105}{32}\frac{U_d}{2\pi\sqrt{r}}\int_0^R \frac{(1-\frac{3r'}{2R})}{R\sqrt{1-\frac{r'}{R}}}\sqrt{r'}Q_{\frac{1}{2}}(\omega)dr'. \tag{3.6}$$

Q_n denotes the Legendre function which, just as ω', is defined in appendix A. From eq. (3.5) and eq. (3.6) it is noted that the induced velocity field does not depend on the blade number B. The only input parameters are the upstream flow velocity, air density and rotor radius.

3.2. Noise of airfoil in circular motion

The foundation theory of this thesis is laid out in appendix A. Amiet [4] developed a model to compute the noise of an airfoil in a turbulent stream. The airfoil is assumed to move in rectilinear motion. This theory is extended to the case of a rotor by assuming that at each instance the rotor blade can be seen as an airfoil in rectilinear motion, and afterwards the results over the whole azimuth are averaged. The airfoil in rectilinear motion and the derivation of the rotor are found in appendix A.

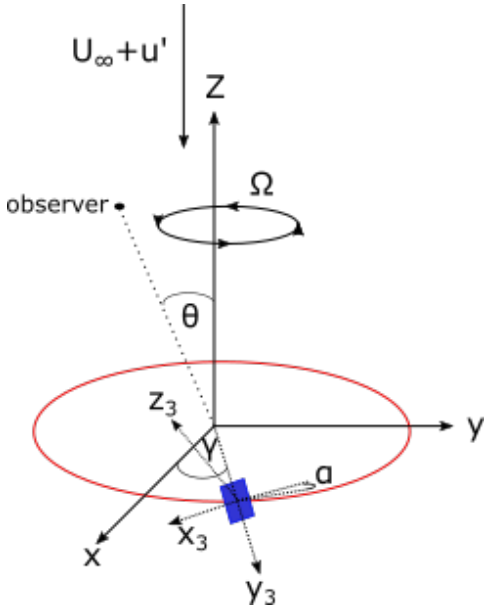

Figure 3.3: Schematic overview of the coordinate system of the rotor noise theory.

Using the result of appendix A, the theory for an airfoil in circular motion, i.e. a propeller, is now presented. The model was developed by Amiet [7]. The idea is that a set of instantaneous spectra is averaged over time. The instantaneous spectra come from the airfoil in rectilinear motion. In order to justify the averaging of the spectra, it must be true that the timescale of the change in instantaneous spectrum is large with respect to the time scale of that spectrum. In other words, an eddy must be completely cut by the rotor blade before the blade has experienced significant rotation. This limits the acoustic frequencies that can be modelled to the rotor rotational frequency, or $\omega > \Omega$ [67] [68].

The power spectral density of a given frequency ω_0 at observer location $\mathbf{x} = (x, y, z)$ equals

$$S_{pp}(\mathbf{x},\omega_0) = \frac{B}{2\pi}\int_0^{2\pi}(\frac{\omega}{\omega_0})^2(\frac{\omega b z \rho_0}{c_0\sigma^2})^2\pi U_a d|\mathscr{L}(\bar{\lambda},\bar{K_y},M)|^2 b^2\overline{u'}^2\Sigma_{-\infty}^{\infty}\Phi_{uu}(\lambda,K_y,K_z^n)\frac{2\pi}{b^2\overline{u'}^2 Z}d\gamma. \tag{3.7}$$

Here, B is the number of blades, ω is the frequency at the blade and $\frac{\omega}{\omega_0}$ is a Doppler factor. The blade its semichord is denoted with b and d is used for the semispan. ρ_0 and c_0 are used to denote the freestream density and speed of sound, respectively. U_a is the advective velocity (depending on radial location) and $\bar{u}^2$ the freestream turbulence intensity. γ is the azimuthal angle and σ and Z are geometric parameters. K_y, K_z and λ are related to ω and the derivation of the parameters can be found in appendix A. The lift function $\mathscr{L}$ is elaborated in section 3.4 and Φ denotes the incoming turbulence spectrum. See fig. 3.3 for the coordinate system used.

3.3. Rapid distortion theory

Rapid distortion theory is concerned with the description of the evolution of velocity and vorticity fluctuations, $\mathbf{u}'$and ω' respectively, as they are transported with mean flow $\overline{\mathbf{U}}$ with mean vorticity $\overline{\Omega}$. The linearised equation for the transport of vorticity is posed in eq. (3.8).

$$(\frac{\delta}{\delta t} + \mathbf{U}\cdot\nabla)\omega' + (\mathbf{u}'\cdot\nabla)\Omega + (\mathbf{u}'\cdot\nabla)\omega' = (\omega'\cdot\nabla)\mathbf{U} + (\Omega\cdot\nabla)\mathbf{u}' + (\omega'\nabla)\mathbf{u}' \tag{3.8}$$

The first simplification is to assume the mean flow is irrotational i.e. $\Omega = 0$. Furthermore, it is assumed that the velocity fluctuations are small compared to the local mean flow, for this recall Taylor's frozen hypothesis in section 2.2. It implies that the vorticity fluctuations are transported only by the local mean flow, and not by the velocity fluctuations. Therefore, the third term on the left hand side drops out. Along the same lines the third term of the right hand side drops out as well. Essentially, it is assumed that on average the effect of the fluctuating velocity $\mathbf{u}'$ is much smaller than $\mathbf{U}$ even if at some times the effect of both terms is comparable.

Note that the viscous terms are neglected as well, meaning the distortion is rapid enough such that viscous dissipation can be neglected. These simplifications reflect the conditions posed in section 2.2.

This yields the following equation.

$$\frac{\mathbf{D}\omega'}{Dt} = (\omega' \cdot \nabla)\mathbf{U} \tag{3.9}$$

Where $\frac{\mathbf{D}}{Dt}$ is the convective derivative associated with the mean flow. Eventually, the goal is to obtain the solution for the velocity fluctuations. The solution is build up from various components, see eq. (3.10).

$$\mathbf{u'} = \mathbf{u'^0} + \mathbf{u'^b} + \mathbf{u'^d} \tag{3.10}$$

Where $\mathbf{u'^0}$ is the upstream velocity fluctuation, $\mathbf{u'^b}$ is the contribution due to the blocking effect and $\mathbf{u'^d}$ is the contribution of the vorticity distortion caused by the mean flow. The blocking effect is best understood as a consequence of the condition that the normal velocity at the body's surface must be zero. That is, the eddies can not pass through the body, hence the velocity fluctuations must change. The vorticity distortion is understood as the stretching of vorticity lines. The stretching, according to Stokes' theorem, changes the vorticity and therefore the induced velocities.

It can be shown that the importance of the blocking and distortion component depends on the lengthscale of the flow, as presented in appendix A.9. The blocking component is dominant for large lengthscales with respect to the body. The vorticity distortion component is governing the small scale distortion.

It is important to realise that this thesis considers both mechanisms, but the respective distortion sources are different. The first distortion is due to the streamtube contraction caused by the rotor. The second distortion is caused by the leading edge radius. Both 'sources' cause a change in turbulence velocity by vorticity distortion and by blocking. However, the importance depends on the lengthscale of turbulence. In the analysis, small scales are assumed for the streamtube contraction. This means that vorticity distortion is considered and not the blocking effect of the rotor. On the other hand, the scales that appear small to the streamtube contraction, can be large with respect to the leading edge, see fig. 3.4. Then, the blocking effect becomes dominant.

According to Britter et al. [18] and Hunt et al. [45] turbulence lengthscales are small with respect to the characteristic body dimension L if $\frac{L^z_{uu}}{L} <= 0.55$. Conversely, lengthscales are considered large if $\frac{L^z_{uu}}{L} >= 5$. Their findings are based on experimental results, and are adopted in this thesis. For ratios between these two values, the behaviour is an intermediate of both asymptotes. That is, both the blocking effect and vorticity distortion play a role.

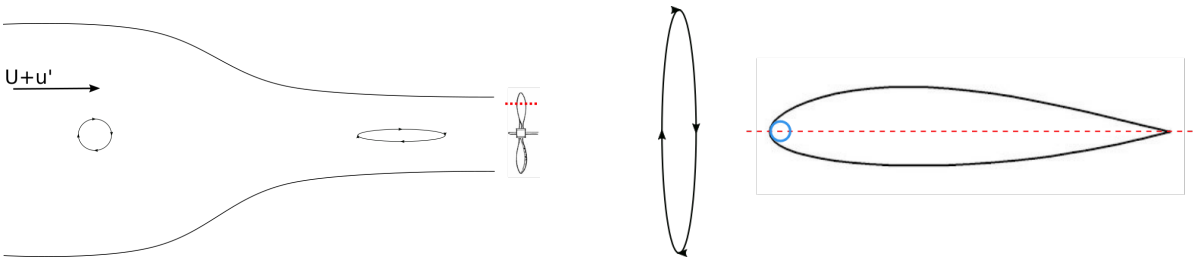

(a) . (b)

Figure 3.4: Qualitative representation of how an eddy small with respect to the streamtube appears large with respect to the leading edge radius. (a) Eddy convected by mean flow and distorted by stream tube and the (b) distorted eddy approaching the blade's leading edge.

3.3.1. Distortion due to streamtube contraction - small lengthscales

The distortion of turbulence caused by the streamtube contraction is valid for lengthscales smaller than the scale of the distortion. In this case, the distortion scale is of order rotor radius R. Hence, it must hold that $\frac{L^z_{uu}}{R} \leq 0.55$. It is important to note that the mechanism below is not valid for lengthscales larger than the rotor radius. However, this is of minor importance as eddies of that size will be seen by the blade as a change in mean flow, rather than a unsteady fluctuation [2].

The analysis starts with the incompressible, inviscid flow assumption. One can then assume that vortex lines follow material lines. Then, using Cauchy's result the upstream vorticity Ω^u_i can be related to the downstream vorticity by eq. (3.11).

$$\Omega_i^u = \Omega_j^d \frac{\delta X_i}{\delta x_j} \tag{3.11}$$

Here, X_i represents the upstream coordinates and x_i the coordinates at the rotor face. Einstein's summation convention for repeated indices is adhered to. The deformation terms $\frac{\delta X_i}{\delta x_i}$ are written in matrix form as in eq. (3.12).

$$\frac{\delta X_i}{\delta x_j} = \begin{bmatrix} \frac{\delta X}{\delta x} & \frac{\delta X}{\delta y} & \frac{\delta X}{\delta z} \\ \frac{\delta Y}{\delta x} & \frac{\delta Y}{\delta y} & \frac{\delta Y}{\delta z} \\ \frac{\delta Z}{\delta x} & \frac{\delta Z}{\delta y} & \frac{\delta Z}{\delta z} \end{bmatrix} \tag{3.12}$$

At this point, the necessity for the mean flow model presented in section 3.1 becomes evident. Namely, the mean flow model generates the velocity field from which the streamlines can be computed by integration of that velocity field. Then, a streamline which ends at the rotor is taken and the time for a particle to travel from the end of the streamline to a distance of $3R$ upstream, T_{trace}, is determined. It has then reached point $\mathbf{X_0^u}$. From the end of the first streamline, located in the rotor plane, a step of δx_i for $i \in [x, y, z]$ is taken. This point serves as the starting point for another streamline, and this line is traced back for the same time t_{trace}. The upstream point of the new streamline $\mathbf{X_1^u}$ is used to determine δX_i. In that manner, the deformation matrix is determined. For every tensor it should hold that $Det(\frac{\delta X_i}{\delta x_j}) = 1$. In this way it is checked that the flow is incompressible, which is required by strain theory.

Equation (3.11) is used to relate the upstream velocity and wavenumbers to the downstream velocity and wavenumbers. This is what is essentially needed: The velocity ratio represents the change in magnitude of the upwash fluctuations, and the wavenumber relation allows to trace back the energy contained by a combination of wavenumbers.

First, the velocity and vorticity fields are described in terms of a Fourier gust component, see eq. (3.13) and eq. (3.14).

$$q(\mathbf{k}, \mathbf{x}) = \mathbf{Q}(\mathbf{k}) e^{i\mathbf{kx}} \tag{3.13}$$

$$\omega(\mathbf{k}, \mathbf{x}) = \mathbf{\Omega}(\boldsymbol{k}) e^{i\mathbf{kx}} \tag{3.14}$$

Using the relation $\omega = \nabla u$ the following is derived.

$$\mathbf{\Omega} = i\mathbf{k} \times \mathbf{Q} \tag{3.15}$$

$$\mathbf{Q} = i\mathbf{k} \times \mathbf{\Omega} / k^2 \tag{3.16}$$

From here, eq. (3.17) and eq. (3.18) are derived.

$$\frac{k^D}{k^U} = (\mathbf{e_3^U})_i (\mathbf{e_3^D})_j \frac{\delta X_i}{\delta x_j} \tag{3.17}$$

$$Q_i^u(\overrightarrow{\mathbf{k^u}}) = Q^d(\overrightarrow{\mathbf{k^d}}) f_1^u \hat{e_2^u} \frac{k^d}{k^u} \tag{3.18}$$

Where Q^d is the magnitude of downstream velocity, and $k^{d,u}$ the magnitude of the down- and upstream wavevectors respectively. The other quantities are explained in appendix A, where a detailed derivation is found.

Both eq. (3.17) and eq. (3.18) are used in the noise model. As explained, the power of the acoustic frequency at an observer is determined by the turbulence spectrum. This spectrum is defined undistorted upstream of the rotor. Now, the values K_x, K_y and K_z^n are defined in the blade frame of reference. To determine the kinetic energy, and in particular of the upwash component, it must be known what the upstream values of those wavenumbers were and the corresponding energy.

Here, the equations eq. (3.17) and eq. (3.18) come into play. The former describes how the wavenumbers are deformed given a deformation tensor, and the latter describes how the turbulence intensity is changed as it is a ratio. The upstream wavenumbers and intensity ratio are plugged into eq. (2.6) to determine the kinetic energy of the upwash fluctuation.

3.3.2. Finite deformation theory

The deformation matrix in eq. (3.12) describes the deformation of a fluid volume. From the deformation matrix it is possible to derive the principle strains, which is the elongation/compression in the three major directions x, y and z. For this, the Lagrangian strain tensor **E** is determined using eq. (3.19).

$$E = \frac{1}{2}(\mathbf{F}^T\mathbf{F} - \mathbf{I}) \tag{3.19}$$

Here, $\mathbf{F} = \frac{dX_i}{dx_i}$ is the deformation tensor and **I** is the identity matrix. Subsequently, the strain $\frac{ds}{ds_0}$ in direction $i \in [x, y, z]$ is computed using eq. (3.20), where λ_i is the i^{th} eigenvalue [54].

$$\frac{ds}{ds_0} = \sqrt{1+2\lambda_i} \tag{3.20}$$

The rotation along the axis in i-direction, $\theta_{j,k}$ is determined using eq. (3.21) for which $i \neq j \neq k$ and $i, k, j \in [1,2,3]$.

$$\theta_{j,k} = -asin(\frac{2E_{j,k}}{\sqrt{1+2E_{jj}}\sqrt{1+2E_{kk}}}) \tag{3.21}$$

3.3.3. Distortion due to the leading edge - large lengthscale

As stated, turbulence can be distorted by two mechanisms. For the streamtube, the vorticity is distorted due to the turning and stretching of material lines. Now, this effect is dominant for lengthscales small with respect to the distortion scale. Eddies affected by the streamtube contraction are an order of magnitude smaller than the streamtube diameter. For the case of distortion caused by the leading edge, the distortion scale is of the order of the leading edge radius.

Hunt [43] described an analytical solution for the large lengthscale analysis to obtain the turbulent velocity fluctuations. The solution holds for a two-dimensional bluff body. The streamwise and normal velocity fluctuations, u' and v' respectively are related to the upstream velocity fluctuations by $\xi = \frac{x}{r_{le}}$ and $\eta = \frac{y}{r_{le}}$, see Zamponi et al. [79], in eq. (3.22) and eq. (3.23)

$$\mathbf{M_{11}^{(0)}}\mathbf{u}'_\infty + \mathbf{M_{12}^{(0)}}\mathbf{v}'_\infty = u' \tag{3.22}$$

$$\mathbf{M_{21}^{(0)}}\mathbf{u}'_\infty + \mathbf{M_{22}^{(0)}}\mathbf{v}'_\infty = v' \tag{3.23}$$

where

$$\mathbf{M_{ij}^{(0)}} = \begin{bmatrix} 1 - \frac{(1-\xi)^2-\eta^2}{((1-\xi)^2+\eta^2)^2} & \frac{2(1-\xi)\eta}{((1-\xi)^2+\eta^2)^2} \\ \frac{-2(1-\xi)^2-\eta^2}{((1-\Xi)^2+\eta^2)^2} & 1 + \frac{(1-\xi)^2-\eta^2}{((1-\xi)^2+\eta^2)^2} \end{bmatrix} \tag{3.24}$$

At the stagnation streamline of the bluff body it yields eq. (3.25a) and eq. (3.25b).

$$u' = u'_\infty(1 - \frac{1}{(1-\xi)^2}) \tag{3.25a}$$

$$v' = v'_\infty(1 + \frac{1}{(1-\xi)^2}) \tag{3.25b}$$

In this asymptotic limit, analogous to the small lengthscale, momentum is conserved. That is, a decrease in streamwise fluctuation leads to an increase in normal velocity fluctuation.

From the above, it is expected that the streamtube contraction will lead to a decrease in upwash fluctuation as seen by the blade. Conversely, the leading edge distortion will increase the upwash velocity. The relative importance of both effects is not known. This holds only if the turbulent lengthscales are small with respect to the rotor radius and large with respect to the leading edge radius.

The analytical expression for leading edge distortion is valid along the stagnation line only. Therefore, the true behaviour of the eddies, and therefore turbulent upwash velocity, might not be accurately described. The analysis also considers a 2-dimensional flow, where the propeller blade is a 3-dimensional object. So, the momentum exchange might also include a third component in the spanwise direction which will influence the results. Another point of attention is the fact that the streamwise velocity of the blade segment varies along the span such that the most outboard part operates above $M = 0.3$. It is not known, what the effect will be of the invalidity of for example the incompressible flow assumption near the tip.

3.4. Lift response function

In order to model the far-field noise it is important to know how an airfoil responds to a gust. The coupling function, known as the lift response function, has been described by Amiet [9] and is repeated here. It is assumed that the incident disturbance is advected with the freestream velocity. For the case of a rotor, the freestream velocity is composed of the rotor's angular velocity and the radial location of the segment, and the flow velocity upstream of the rotor. A natural division is made between two regimes. Those are the low-frequency regime, where the flow is treated as incompressible i.e. the gust reaches the trailing edge instantaneously when interacting with the leading edge. The other regime is the compressible regime or high-frequency regime, where there is a phase difference between the leading and trailing edge interaction.

Suppose an airfoil with chord c is moving at U_∞ and the speed of sound is c_∞. Suppose the frequency of incoming turbulence is ω_0, then the phase shift is $\frac{\omega_0 c}{c_\infty + U_\infty}$ between the pressure at the leading and trailing edge. For incompressible flow, c_∞ tends to infinity. So essentially, there is no phase difference. But, for high frequencies (in the limit towards infinity), this is not true anymore. In general, for an acoustic wavenumber k the criterion for incompresssible flow is given by eq. (3.26).

$$\frac{kc}{1+M} \ll 1 \tag{3.26}$$

This is equivalent to requiring the blade to be compact, see Aeroacoustics of Low Mach Number Flows [34]. Hence, there is need to treat low and high frequencies differently.

The effective lift for low frequencies is given by eq. (3.27)

$$\mathscr{L}(\bar{K}_x, \bar{K}_y, M) = \frac{1}{\beta_{pg}} S(\bar{K}_x{}^\star) e^{i\bar{K}_x{}^\star f(M_\infty)} [J_0(\mu x/\sigma) - i J_1(\bar{\mu} x/\sigma)] \qquad \bar{\mu} < 0.4 \tag{3.27}$$

where, $S(k)$ is the Sear's lift response function, J_0 and J_1 are Bessel functions and $f(M_a) = (1-\beta_{pg})ln(M_a) + \beta_{pg} ln(1+\beta_{pg}) - ln(2)$. The overbar states a normalisation by semichord b. β_{pg} is the Prandtl-Glaeurt correction factor. A more lengthy description can be found in appendix A.

The high-frequency response takes into account two terms: First, the interaction and scattering at the leading edge, $\mathscr{L}_1$, is determined. An additional factor, accounting for the scattering at the trailing edge, $\mathscr{L}_2$ is calculated. These solutions were determined numerically by Amiet using the Schwarzschild theorem. The problem is treated as leading edge scattering on a semi-infinite plate independently of the trailing edge scattering of another semi-infinite plate. A velocity potential is determined using the boundary conditions at the leading edge which are the no penetration condition and zero-velocity potential. This solution is superimposed on the solution found at the trailing edge. The exact details of the lift response derivation are out of this thesis' scope. For a more detailed explanation on this topic the reader is referred to the PhD dissertations of De Santana [25] or Christophe [21].

The resulting lift response functions are given by eq. (3.28) and eq. (3.29).

$$\mathscr{L}_1(\bar{K}_x, \bar{K}_y, M) = \frac{\sqrt{2}}{\pi\sqrt{\bar{K}_x(1+M_\infty)\Xi_1}} E^\star(2\Xi_1) e^{i\Xi_2} \tag{3.28}$$

$$\mathscr{L}_2(\bar{K}_x, \bar{K}_y, M) = \frac{e^{i\Xi_2}}{\pi\Xi_1\sqrt{2\pi\bar{K}_x(1+M_\infty)}} \left[i(1-e^{-i2\Xi_1}) + (1-i)\left(\frac{\sqrt{2}e^{-i2\Xi_1}}{\sqrt{1+(M_a/M_\infty)(x/\sigma)}} E^\star(2\bar{\mu}(M_\infty/M_a + x/\sigma))\right)\right] \qquad \bar{\mu} >= 0.4 \tag{3.29}$$

$E^\star$ symbolises a Fresnell integral, $\Xi_1 = \bar{\mu}(M_\infty/M_a - x/\sigma)$, $\Xi_2 = \bar{\lambda} + \bar{\mu}(M_a - x/\sigma) - \pi/4$. M_a represents the advective Mach number and $M_\infty^2 = M_a^2 - \beta_{pg}^2 K_y^2/K_x^2$.

3.5. Hypothesis

Based on the analytical models above, the following hypothesis are formulated. These will be compared with experimental data to check the validity of each model.

Hypothesis 1. *The mean flow model of H&O accurately predicts the mean flow upstream of the propeller.*

Approach. Only the thrust and freestream velocity are required as input for the model. The thrust follows from load measurements and the freestream velocity is determined using a hotwire. The predicted flow field is compared with planar PIV and hotwire measurements.

Hypothesis 2. *The turbulent velocity fluctuations are sufficiently small such that they are only advected with the local mean flow, and do not change it.*

Approach. This is the equivalent of Taylor's frozen hypothesis and is used in RDT. It is verified by means of hotwire measurements if $\frac{\overline{u'}}{U_\infty} << 1$.

Hypothesis 3. *The distortion of turbulence by the streamtube contraction and leading edge occur sufficiently rapid.*

Approach. The second assumption of RDT is that the distortion is rapid i.e. $\frac{\overline{u'}H}{U_a L^z_{uu}} << 1$. Here, H is the characteristics body dimension. The lengthscales are determined by calculating the temporal autocorrelation of the hotwire signal and integrating the correlation curve. The characteristic body dimensions are the rotor radius R and leading edge radius $r_{l.e.}$.

Hypothesis 4. *The turbulence lengthscale is small with respect to the propeller radius and large with respect to the leading edge radius.*

Approach. Temporal (hotwire) and spatial (PIV) data is used to determine the lengthscales upstream and close to the propeller, respectively. It is checked if $\frac{L^z_{uu}}{R} <= 0.55$ and $\frac{L^z_{uu}}{r_{l.e.}} >= 5$.

Hypothesis 5. *The observer is located in the far-field, where Amiet's theory is valid.*

Approach. For this to hold $kr = \frac{2\pi}{\lambda} r >> 1$, see Aeroacoustics of Low Mach Number Flows [34]. Here, r is the distance to the observer and λ and k the acoustic wavelength and wavenumber, respectively.

4

Experimental set-up

This chapter explains the propeller model and flow conditions. The measurement apparatus together with the test set-up are presented as well.

4.1. Windtunnel, model and flow conditions

The experimental campaign was carried out at the anechoic windtunnel in the TU Delft low speed aerodynamics lab. The windtunnel has a circular nozzle with a diameter of $0.6m$. The freestream velocity at the nozzle has been characterised with a Pitot tube. The freestream velocity equals $U_\infty = 9m/s$ and the propeller is operating at advance ratio $J = 0.225$.

To generate turbulence a grid has been placed at the nozzle exit, see fig. 4.2b. This grid has a mesh size G of $100mm$ and is composed of aluminium rods with a square cross section of $s^2 = 100mm^2$. The distance from the grid to the propeller equals $1.00m$, or $10G$. The angle between the propeller plane and flow in z-direction equals 90°. This has been verified with an inclinometer with 0.01° accuracy.

The propeller has a diameter D of $30cm$ and adopts a NACA-4412 profile along the whole span. The design has been based on an APC 9x6, diameter of 9″ and pitch of 6″. The maximum chord equals $c_{max} = 3.4cm$ and the maximum twist angle $\beta_{max} = 43.6°$, see fig. 4.1. The aluminium alloy propeller has been manufactured with a CNC machine with 0.4 to 0.8μm Ra finish and the blade has been covered with non-reflective paint. A dynamical balancing procedure has been performed to remove mass unbalances in the propeller.

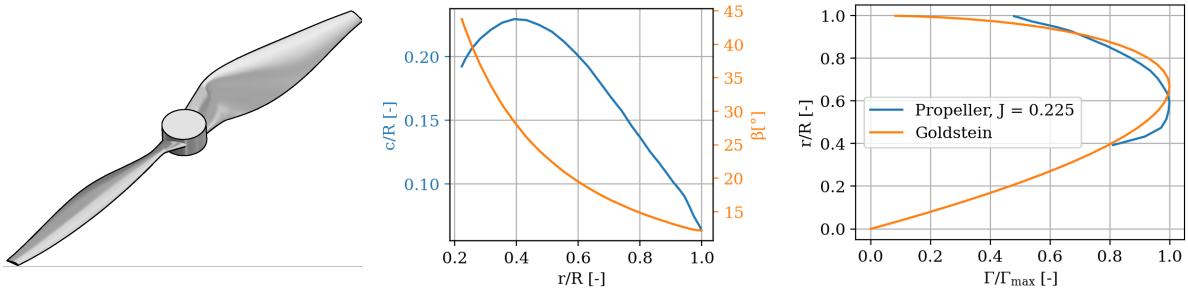

(a) (b) (c)

Figure 4.1: Propeller based on APC 9x6 (a) sketch of propeller (b) blade twist and chord distribution along radius (c) circulation distribution compared with Goldstein's optimum.

The propeller is powered by a LMT 2280/34 brushless inrunner. The motor is attached to an ATI-Mini40 torque/loadcell which measures loads in the z-direction up to $60N$ (0.75% accuracy), and in the x- and y-directions up to $20N$ (1% and 1.25% accuracy, respectively). The resolution is $1/100N$ in the z-direction and $1/200N$ in the x and y direction. The torque can be measured accurately up to $1Nm$ in all three directions with a resolution of $1/8000Nm$. The rotational speed is monitored by a US Digital EM1 encoder combined with a US Digital Disk-1 transmissive rotary encoder disk.

The motor-loadcell configuration has been shielded by a circular nacelle to minimise noise sources other than the propeller, see fig. 4.2c. The nacelle is supported by a $c = 70mm$ chord NACA-0012 wing. Zig-zag tape has been placed at $0.2c$ in order to ensure a turbulent boundary layer on the supporting wing and mitigate tones associated with a laminar boundary layer.

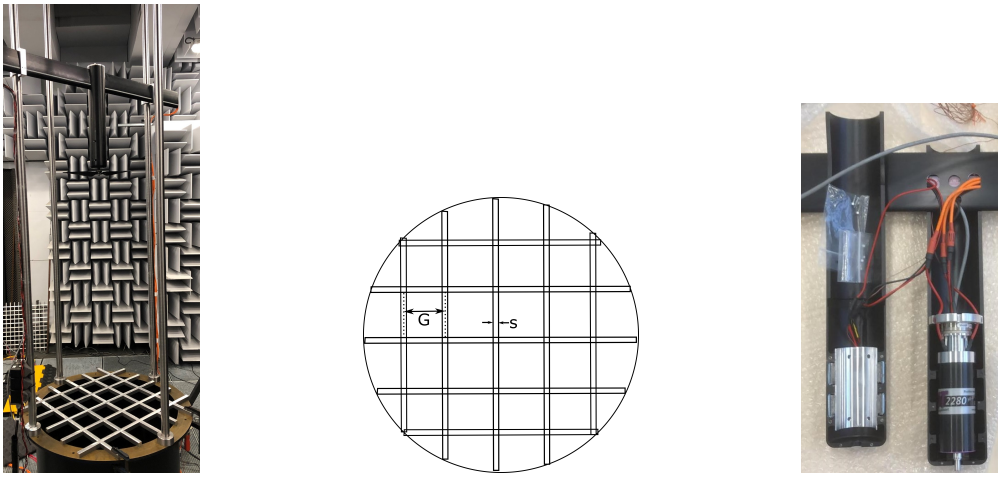

(a) (b) (c)

Figure 4.2: Components of setup. (a) Full set-up (b) schematic representation of grid where G = $0.1m$ and s $0.01m$ (c) motor loadcell configuration.

4.2. Acoustic measurements

An array containing 25 G.R.A.S. 40 pH free-field microphones is installed to perform the far-field acoustic measurements. The frequency response equals $\pm 1dB$, the frequency range is from $10Hz$ to $20kHz$ and the maximum output $135dB$. The reference pressure is $20\mu Pa$ and the microphones have an integrated CCP preamplifier. These microphones are located at $4D$ distance away from the propeller centre in the y direction, see fig. 4.3. The microphones are aligned vertically and extend from $8G$ downstream, to $10G$ upstream of the propeller. Microphone signals are recorded for a total of $20s$ at $51.2kHz$. The data is segmented into Welch blocks with 50% overlap, resulting in a frequency resolution of $10.67Hz$.

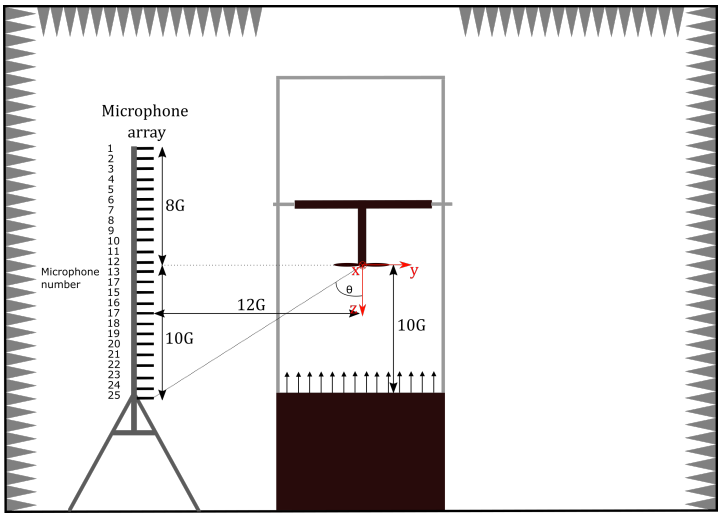

Figure 4.3: Schematic representation of microphone array and set-up. $G = 0.1m$.

4.3. Particle image velocimetry

The flow is seeded with particles using a SAFEX Twin Fog generator, with SAFEX-Inside-Nebelfluid. The average diameter of the seeding particles is $1\mu m$. A Quantel EverGreen200 Double-Pulse Nd:YAG laser is used to illuminate the flow with $200mJ$ per pulse and $532nm$ wavelength. One LaVision sCMOS camera with 2560×2160 pixels is used to capture the particles. A Nikon lens with $200mm$ focal length at a f-stop, $f_\#$, of 8 is used for the measurements. The resulting field of view is $25x25mm^2$. The flow at the leading edge has been measured at $r/R = .4$ of the blade. A total of 2000 double-framed, phase-locked images has been acquired at a frequency of $14.8Hz$.

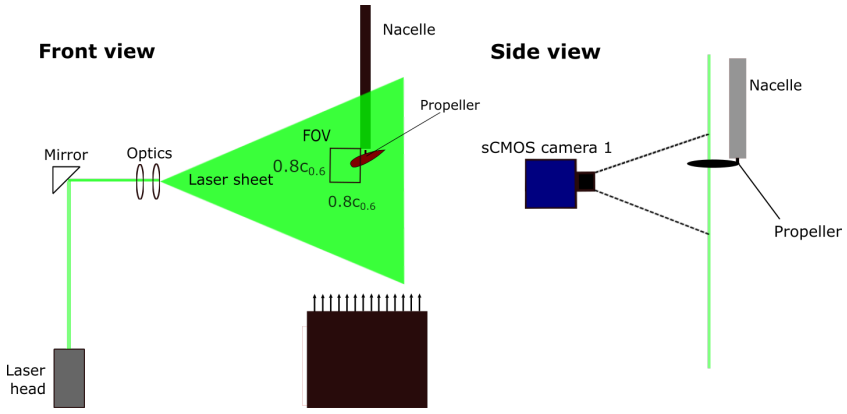

Figure 4.4: Schematic representation of planar PIV setup for phased-locked measurements. $c_{0.6} = 30mm$.

A planar PIV is performed to measure the upstream velocity and turbulence, see fig. 4.5. A second LaVision sCMOS camera is added to enlarge the field of view. The same lenses as for the phased-locked measurements are used. In this set-up $f_\# = 11$ and the resulting total field of view of the two cameras is $400x260mm^2$. At $\approx 14Hz$ a total of 1500 images is acquired. This set-up can be seen in fig. 4.5. The images are processed using LaVision 10.1.0. A summary of both set-ups can be found in table 4.1.

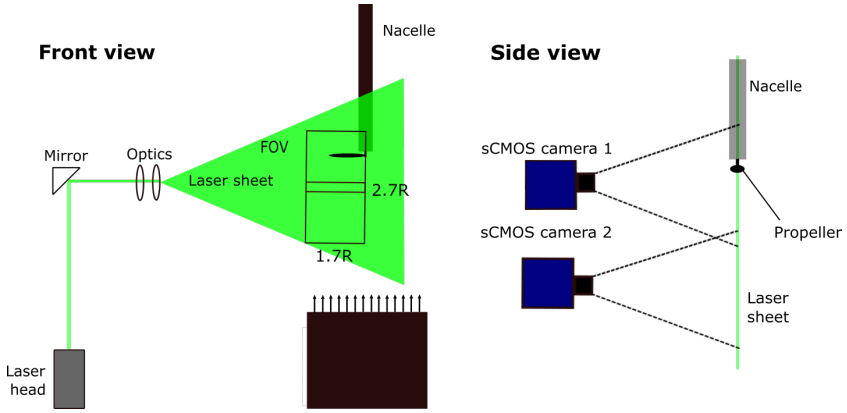

Figure 4.5: Schematic representation of planar PIV setup for inflow measurements. $R = 150mm$.

Parameter	Streamtube	Leading edge
PIV method	Planar	Planar
Frame type	Double-Frame	Double-Frame
Lens focal length	$200mm$	$200mm$
$f_\#$	11	8
Field of View	$\approx 400x260mm^2$	$\approx 25x25mm^2$
Aquisition frequency	$14Hz$	$14.8Hz$
Pulse separation delta t	$70\,\mu s$	$6-7\mu s$
Spatial resolution	$\approx 1.62mm$	$\approx 0.14mm$
Number of recordings	1500	2000
Number of effective recordings	250	150
Final interrogation window	$48x48px^2$	$12x12px^2$

Table 4.1: Summary of PIV set-up

4.4. Hotwire anemonetry

A $5\mu m$ diameter, $1.25mm$ long platinum plated, tungsten wire manufactured by Dantec Dynamics (Type P11, $R_{20} = 3.4$, $R_l = 0.5$, $\alpha_{20} = 0.36$) is installed on a remotely controlled 2D traversing system, see fig. 4.6. The probe is controlled by a constant temperature bridge. Hotwire measurements are performed at a sampling frequency of $51.2kHz$ for a duration of $10s$, except for the line closest to the rotor, where the measurement time equals $30s$. The hotwire was oriented such that the streamwise velocity is measured.

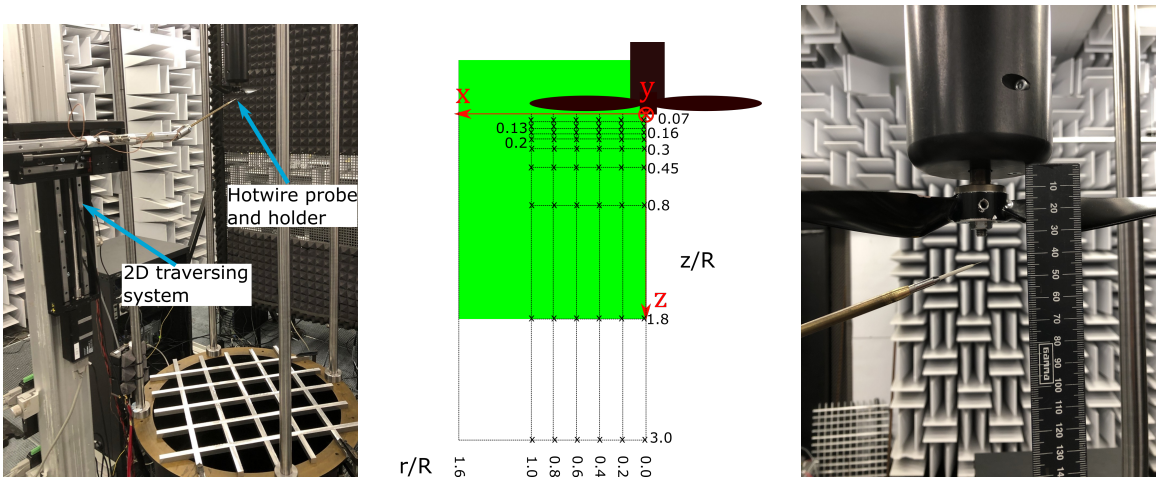

(a) (b) (c)

Figure 4.6: (a) Overview of hotwire set-up including 2D traversing system. (b) Hotwire measurement locations denoted with 'x' and PIV FOV for reference. (c) Close-up of hotwire probe at $z/R = 0.07$.

4.5. Measurement uncertainty

Temperature drift of the freestream is one of the dominant sources contributing to the uncertainty associating with hotwire measurements [16, 22]. This is because the heat transfer, which is the governing principle of a constant temperature hotwire system, is directly proportional to the temperature difference between the flow and sensor. Other errors are related to the calibration, for which a Pitot tube was used. Moreover, a curve fitting procedure is followed during the calibration which induces an error. The total measurement error of the velocity is considered to be 3% for the hotwire, see Jørgensen [46].

The data of PIV measurements contains uncertainties coming from both random and biased components. The former encompasses errors in the cross-correlation, about $0.1px$ as described by Westerweel [74], and the convergence of the statistics as $\frac{\sigma_u}{\sqrt{N}}$, see Sciacchitano [62]. Here σ_u is the standard deviation of the velocity component and N the number of images. An example of biased errors is peak locking, which happens if the particle image diameter $d_\tau < 1px$. Conversely, if $d_\tau >> 1px$, then the individual particle images overlap and resolution is lost. A compromise between the two effects is $d_\tau = 2px$. For the streamtube and leading edge images d_τ equals $2.3px$ and $2.6px$, respectively, meaning that they have a relatively low impact [56]. Hence, it is assumed that the random components are the dominant contributors to the uncertainty for both flow cases.

4.5.1. RPM variability

The RPM for the first two seconds are plotted in fig. 4.7 and is representative for the remainder of the measurement duration. The mean values of the RPM are 7997, 8002 and $7998RPM$ for the clean inflow, turbulent inflow and motor only, respectively. The corresponding standard deviations are 14.6, 37.8 and $13.8RPM$.

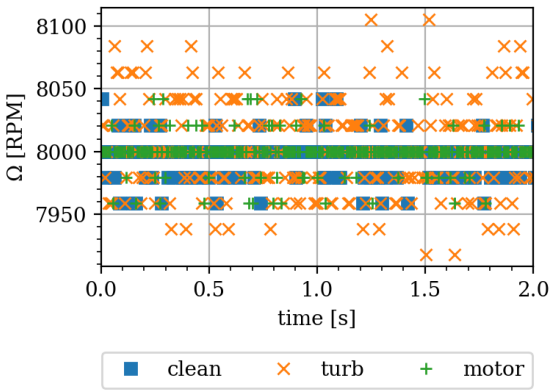

Figure 4.7: RPM variability for 1) clean inflow 2) turbulent inflow 3) motor only.

There is no variation in mean RPM between the clean and turbulent inflow case. However, the observed relatively large fluctuations for the turbulent case (up to $100RPM$) can have an effect on the acoustic spectrum as it is unsteady loading. Hence, the difference in spectra between turbulent and clean inflow can not be fully ascribed to the turbulence interacting with the blade. The effect of RPM variation on BPF 1 has been shown by Grande et al. [38]. A variation of $0.4-0.65dB$ at $J = 0.24$, depending on the microphone location, was found.

The fluctuations of RPM explains why the effective recordings for the leading edge case is so low. Namely, a variation in RPM will change the blade's location in the image and therefore these images can not be used to compute the flow field close to the leading edge as it is essentially a different flow case.

5

Results & discussion

The aim of the chapter is to describe and discuss the experimental results. First, the thrust measurements are discussed in section 5.1. Following are the mean flow and turbulence statistics in section 5.2. Both the thrust and mean flow velocity serve as input for the mean flow model, which is validated in section 5.3. The mean flow model predicts a streamtube which is used to analytically model the distortion of turbulence in section 5.4. Distortion caused by the leading edge is discussed in section 5.5, where the asymptotic theory of Hunt [43] is validated with experiments. The results are used in section 5.6, where the experimental and analytical spectra are presented and compared. In section 5.7 the hypothesis of the analytical model are assessed on their validity.

5.1. Thrust

The evolution of thrust coefficient over time is plotted in fig. 5.1. The load measurements were started after the rotor was operating sufficiently long to assume that steady conditions were established. The C_t measurements have been filtered using a moving average in order to improve readability. The thrust coefficients were measured for three cases: 1) Turbulence generating grid installed 2) Clean inflow 3) Turbulence generating grid installed with hotwire probe in flow. The first two cases are used to check if the grid changes the thrust of the propeller. This affects the steady loading noise of the blade and needs to be quantified in order to isolate turbulence ingestion noise. The latter case is used to assess the influence of the hotwire on the thrust. It is assumed that the influence of the hotwire is largest at the distance most close to the rotor and when the probe fully spans the blade radius. This corresponds to ($z/R = 0.07, r/R = 0$) in fig. 4.6b and fig. 4.6c. Therefore, this location is used during the thrust measurements.

Over the course of the measurement time the thrust coefficient increases 0.38%, 0.27% and 0.18%, and the measured mean C_t equals 0.1097, 0.1109 and 0.1114 for the grid, no grid and grid with hotwire, respectively. The mean C_t increased with 1.5% when the hotwire was ingested fully into the flow. The mean C_t of the clean inflow case is 1% higher than for the turbulent inflow case.

The thrust is calculated using eq. (2.1), where $D = 0.3m$, $\rho = 1.225kg/m^3$ and $n = 133.3Hz$. It follows that $T_{exp} = 19.4N$. This is the value that is used to calculate U_d in eq. (3.4) and the propeller induced velocities upstream in order to validate the analytical mean flow model.

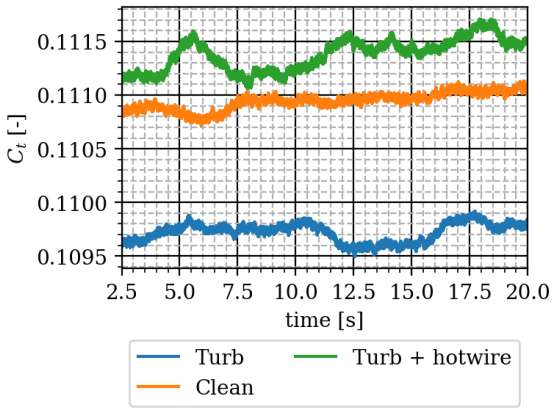

Figure 5.1: Thrust coefficients as function of time for the 1) turbulent inflow 2) clean inflow 3) turbulent inflow with hotwire at $0.07z/R$ upstream and $r/R = 0$.

5.1.1. Discussion

The observed increase of C_t over time is ascribed to temperature drift of the loadcell during the measurements. The maximum observed temperature increase of the loadcell was $5.2°C$. A maximum gain error of 0.5% can therefore be expected, as provided by manufacturer ATI [12]. Similar observations for a closed motor-nacelle-loadcell (fig. 4.2c) structure have been made by Van Arnhem et al.[73].

The effect of placing the hotwire in the flow is marginal. Moreover, the flow intrusion is largest at the specific location. When placing the hotwire more outboard and upstream, there is less disturbance of the flow as a smaller part of the radius is operating in the disturbance caused by the hotwire. Moreover, the flow has more time to recover when further upstream. Therefore, it is assumed in the subsequent sections that the propeller induced flow field does not change when performing the hotwire measurements.

5.2. Mean flow characterisation

To calibrate the windtunnel a Pitot tube was used. This was done without the grid present. The freestream flow characteristics are acquired at $3R$ upstream of the propeller plane using the hotwire, as depicted in fig. 5.2. Neither the average flow velocity nor the turbulence intensity is homogeneous in radial direction. The axial velocity ranges from $\approx 8m/s$ to $\approx 10m/s$ from inboard to outboard. The average velocity $\overline{U} = 9m/s$, hence U_∞ is set to $9m/s$. The turbulent velocity ranges from $0.74/m$ to $0.95m/s$ with an average of $0.85m/s$ yielding a turbulence intensity of 9.3%

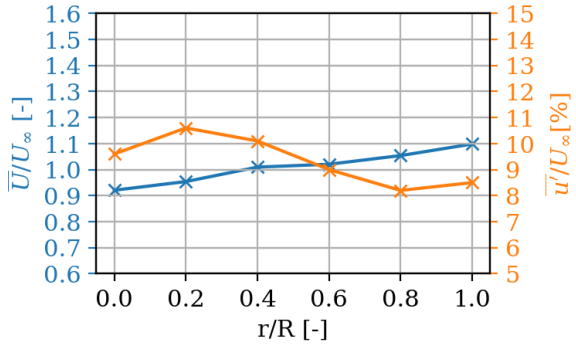

Figure 5.2: Radial distribution of mean flow and turbulence intensity at $z/R = 3.0$. $U_\infty = 9m/s$

5.2.1. Upstream turbulence spectrum

The upstream turbulence spectra are defined at $z/R = 3$ in correspondence with the analytical model of Amiet. For every location, the integral length scale is determined using eq. (5.1).

$$L^z_{uu} = \overline{U} \int_0^\infty \rho_{uu}(\tau) d\tau \tag{5.1}$$

ρ_{uu} is the correlation coefficient resulting from normalising the time delay autocorrelation. The conversion from time to spatial domain rests on Taylor's frozen hypothesis, see section 2.2.

In fig. 5.3 the turbulence spectra are depicted for different radial positions. As reference, the one-dimensional Von Kármán spectrum (V.K., red line) is plotted with representative input parameters. At all radial locations the spectra exhibit the characteristic $f^{-5/3}$ slope. Furthermore, the spectra can be accurately modelled using the Von Kármán turbulence spectrum, albeit with different parameters. The results are tabulated in table 5.1. There is a difference in statistics along the radial positions, indicating that the upstream turbulence field is nonhomogeneous at $z/R = 3$. That is, the average turbulence integral lengthscale equals $0.022m$ and the average turbulence velocity is $0.85m/s$.

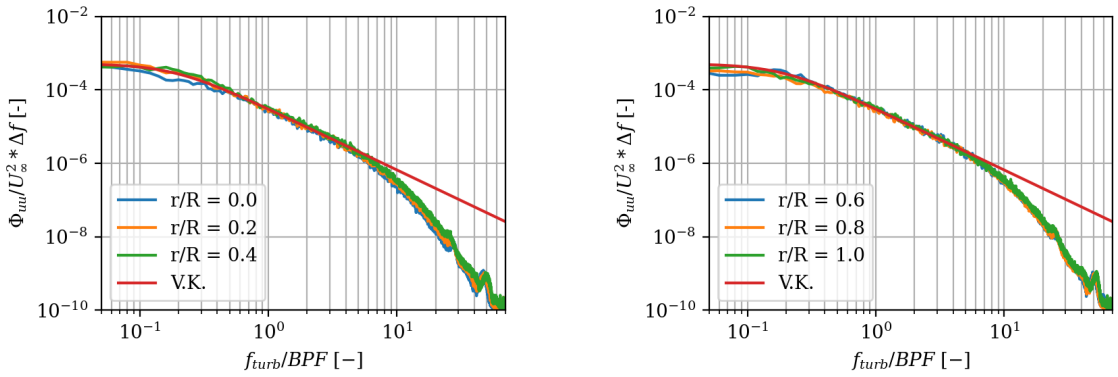

(a) (b)

Figure 5.3: Upstream ($\frac{z}{R} = 3$) turbulence spectra at (a) $r/R = 0,0.2,0,4$ (b) $r/R = 0.6,0.8,1.0$. $U_\infty = 9m/s$, $\Delta f = 5Hz$. Von Kármán spectrum with $L^z_{uu} = 0.022m$ and $\overline{u'} = 0.85m/s$.

r/R	0	0.2	0.4	0.6	0.8	1.0
L^z_{uu} **[m]**	0.021	0.032	0.022	0.016	0.018	0.02
$\overline{u'}$ **[m/s]**	0.86	0.95	0.81	0.74	0.76	0.84

Table 5.1: Turbulence statistics measured at $z/R = 3$.

5.2.2. Discussion

The observed non-homogeneity of the mean flow and turbulence intensity can be explained using empirical results of Roach [57]. Namely, at a distance of $3R$ upstream of the propeller ($5.5G$ downstream of the grid) the turbulence field is not yet fully developed to an homogeneous field. Instead, a distance of at least $10G$ downstream of the grid is required for a homogeneous turbulence field. Also in this case it remains the question if true homogeneity is obtained, as elaborated upon by Ertunç et al. [24].

The upstream homogeneous and isotropic spectrum, as required by Amiet's noise model, is modelled using the average lengthscale and turbulence intensity in the remainder of the thesis. However, as depicted fig. 5.3, this only approximates the average. The radial variance is not taken into account. This means that at radial locations with values below average it is assumed that there is more energy and vice versa for locations with the parameters larger than the average. A consequence is that the modelled turbulence contains more energy at the outboard locations $r/R = 0.4, 0.6, 0.8$ and 1.0. The overestimation can have a significant effect as the outboard locations have a larger contribution to the noise of the propeller.

The windtunnel speed was set at $8m/s$ using the calibration without the grid present. But using this setting, U_∞ was found to be equal to $9m/s$ for the turbulent inflow case. This can be explained by the fact that the grid, with a porosity of 81%, blocks the flow and hence it is accelerated . So besides the turbulence that is added to the flow, the mean flow is increased as well. Hence, $J_{clean} = 0.2$ whereas $J_{turb} = 0.225$. This can explain the observed differences in C_t as described in section 5.1. The effect of the change in J on steady loading and thickness noise is discussed in section 5.6.

5.3. Validation of mean flow model

As explained in section 3.3, the mean flow model of Hough and Ordway (H&O) is used to analytically predict the distortion of turbulence by the streamtube contraction. The comparison of the axial velocities predicted by model with the experimental results is depicted in fig. 5.4. When the measured thrust, $T_{exp} = 19.4N$, is used as input thrust T ($T/T_{exp} = 1$), the model overpredicts the velocities as measured by the PIV and hotwire systems across the whole radius. The difference between the model and hotwire and PIV at $0.4r/R$, $z/R = 0.07$ equals 41% and 49%, respectively.

In order to have a better correspondence between the predicted induced velocities and the measured velocities, the thrust used as input in eq. (3.4) is adjusted. By lowering the thrust, the induced velocities are lower and a more representative analytical flow field is obtained. The value of T such that $T/T_{exp} = 0.52$ yields the predictions that corresponds best to the PIV results at $r/R = 0.4$. The reason to match the predicted and measured velocities at this location is that most elongation, hence distortion, is expected there.

Hough and Ordway's model rests on the assumption that the blade is loaded according to Goldstein's optimal distribution such that energy loss in the slipstream is minimised. However, the blade used in the experiment has not been designed as such, see fig. 4.1c. It can be seen that for Goldstein's optimum the maximum circulation is found at $\approx 0.7r/R$. The blade has this optimum at $0.6r/R$. Furthermore, Goldstein assumes that the blade is loaded from hub to tip. For $J = 0.225$, the inboard part of the propeller blade is in stall and will not contribute to the thrust.

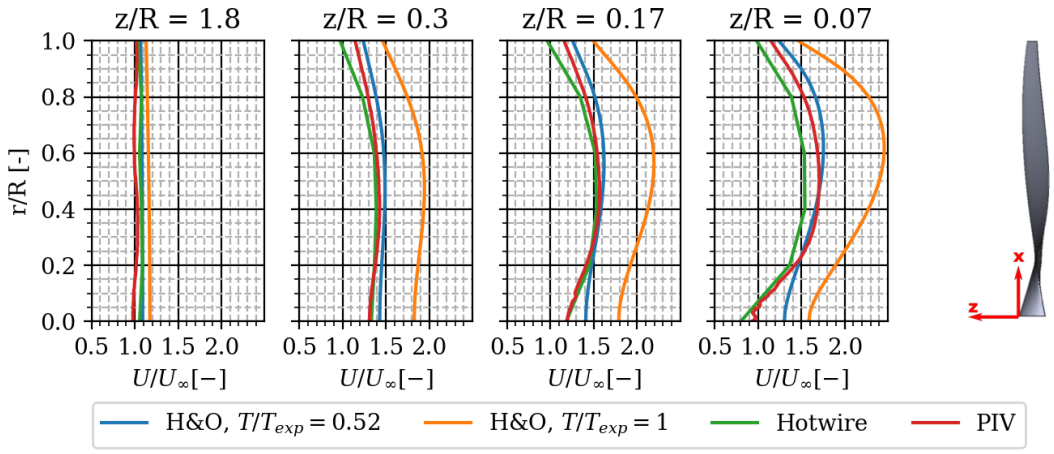

Figure 5.4: Comparison of hotwire, PIV and analytical model. $U_\infty = 9m/s$.

5.3.1. Streamtube contraction

In fig. 5.5a the analytically ($H\&O$) computed streamlines are compared with the experimental streamlines derived from the PIV measurements. The streamlines are computed up to $z/R = 2.0$ instead of $z/R = 3.0$ due to the limited field of view of the PIV set-up. This poses no limitations on the analysis as the analytical model with $T/T_{exp} = 1$ predicts the streamtube radius to be $\approx 1.41R$ whereas at $z/R = 3.0$, which is the upstream location considered in Amiet's model, the streamtube radius $\approx 1.44R$. For the computation that matches the experimental results, i.e. $T/T_{exp} = 0.52$, the difference between $z/R = 2$ and $z/R = 3$ is $0.01R$. The upstream streamtube radius at $z/R = 2$ is $\approx 1.15R$, which follows from the PIV measurements. This indicates a contraction ratio of $C = 1.3$. This is closely approximated by using $T/T_{exp} = 0.52$ in the analytical model. Namely, the streamtube radius at $z/R = 2.0$ equals 1.19.

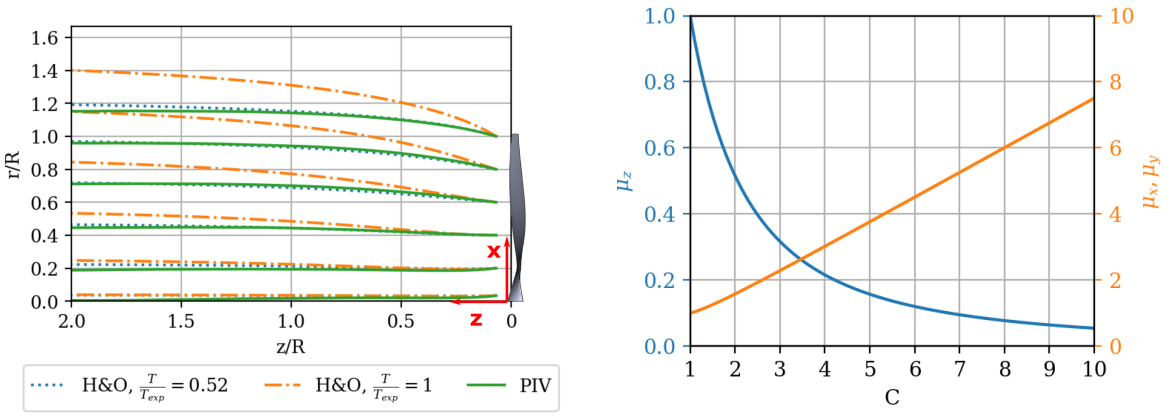

(a) (b)

Figure 5.5: (a) Comparison of streamlines approaching different radial locations. (b) Effect of symmetrical contraction on the energy ratios of the turbulent velocity fluctuations, as predicted by Batchelor and Proudman [13].

5.3.2. Discussion

The fact that the propeller's circulation distribution over the radius differs from Goldstein's optimum can explain why the predicted maximum axial induced velocity is located at $r/R = 0.6$ and that the PIV measurements show this location to be $r/R = 0.4$. Besides, the streamlines show only marginal curvature. This means that velocity fluctuations originally in z-direction, remain dominant in z-direction. This is quantified using the deformation tensor. Using eq. (3.21) the rotation along the y-axis at $r/R = 0.4$ is determined to be $\approx 12°$ using PIV measurements, and $\approx 14°$ using $T/T_{exp} = 0.52$. As a consequence, the largest measurable distortion theoretically occurs at this location. That is, the vorticity lines are stretched most in streamwise direction and the orientation differs only slightly. This means that the decrease in velocity fluctuation in streamwise direction is largest.

As stated, the input thrust was modified in order to better match the measured PIV velocity profile. A similar modification was deemed necessary by Robinson [58]. Given the significant differences between the experimental results and the model of Hough and Ordway, it is evident that this model is not suitable to predict the upstream mean flow for low Reynolds number propellers.

Moreover, the adjusted thrust does still not fully resemble the measured axial velocity profile. It was used to match the location where most elongation is expected. It can be seen in fig. 5.4 that the axial velocity at the outboard and inboard locations are still overpredicted. Therefore, the model is overpredicting the amount of distortion at those locations.

The observed differences between the hotwire and PIV measurements are ascribed to the measurements uncertainties of both techniques. Moreover, an additional error is introduced when the locations of the two techniques are matched.

5.4. Turbulence distortion due to streamtube contraction

In section 5.3.1 the theoretical and experimental streamtubes have been presented. As explained in chapter 2, the stretching and turning of vorticity lines alters the turbulence velocity fluctuations. For a symmetrical contraction, i.e. the off-diagonal terms of the deformation tensor are zero, the ratio of turbulent velocity fluctuations after ($\overline{u_a'^2}$) and before ($\overline{u_b'^2}$) the contraction, $\mu_i = (\frac{\overline{u_a'^2}}{\overline{u_b'^2}})_i$, is a function of the contraction ratio C. The theoretical result of Batchelor and Proudman [13], which is valid for isotropic turbulence, is presented in fig. 5.5b, where $i \in [x, y, z]$.

Since the theory holds for symmetrical contraction, it is instructive to assess the streamlines which remain relatively straight. This is the case for the inboard radial location $r/R = 0.4$, which rotates along the y-axis with $\approx 12°$ as discussed in section 5.3. Therefore, that location is used in the subsequent analysis.

Using eq. (3.19) and eq. (3.20) the contraction ratio at $r/R = 0.4$ is determined to be $C = 1.3$ for the streamtube derived from the PIV data. The corresponding value for μ_z, which represents the squared ratio of the streamwise velocity fluctuations, is equal to 0.8. Consequently, the ratio $(\frac{\overline{u_a'}}{\overline{u_b'}})_z \approx 0.9$. Similarly,

$(\frac{\overline{u'_a}}{\overline{u'_b}})_x = \sqrt{\mu_x} \approx 1.07.$

5.4.1. Experimental results

To assess the distortion of turbulence, the evolution of turbulence integral lengthscales and the turbulent velocities in z and x direction is determined. The turbulent velocities follow straightforwardly from the set of PIV vector images. The procedure to calculate the former is briefly explained. L^m_{ij}, where $m \in [x, y, z]$ and $i, j \in [u, v, w]$ is defined in its most general form in eq. (5.2).

$$L^m_{ij} = \int_0^\infty R_{ij}(m)\delta m \tag{5.2}$$

The definition of the spatial correlation function $R_{ij}(\delta m)$ is reproduced from Hinze [41], see eq. (5.3).

$$R_{ij}(\delta m) = \frac{\overline{i(m)\,j(m+\delta m)}}{i^*(m)\,j^*(m+\delta m)} \tag{5.3}$$

The $\overline{(...)}$ symbolises the time average quantity and $i^* = \sqrt{\overline{(i-\bar{i})^2}}$. It is often impractical to use a large upper bound in eq. (5.2) as the PIV field of view is limited. Instead, the lengthscales are estimated by determining δm such that $R_{ij}(\delta m) = 1/e \approx 0.37$. The same approach has been used by Romano [59], Falchi et al. [27], Nguyen et al. [53] and Matozinhos et al. [49]. The above procedure is illustrated in appendix B. The time averaged quantities are determined by using a phaselocked subset containing $N = 250$ images. This subset is retrieved from the original, non-phaselocked, set of $N = 1500$ images.

At $z/R = 1.8$ the ratio $\frac{\overline{u'}}{\overline{v'}} \approx 1$ regardless the radial location as depicted in fig. 5.6. This is characteristic for isotropic turbulence. For every radial location, a linear trendline is added to capture the evolution of the ratio in a straightforward way. This, however, does not imply that the evolution is linear itself.

The ratios of $\frac{\overline{u'}}{\overline{v'}}$ are found to remain approximately constant as the rotor is approached at all radial locations except $r/R = 0.0$. There, a stronger decrease is observed.

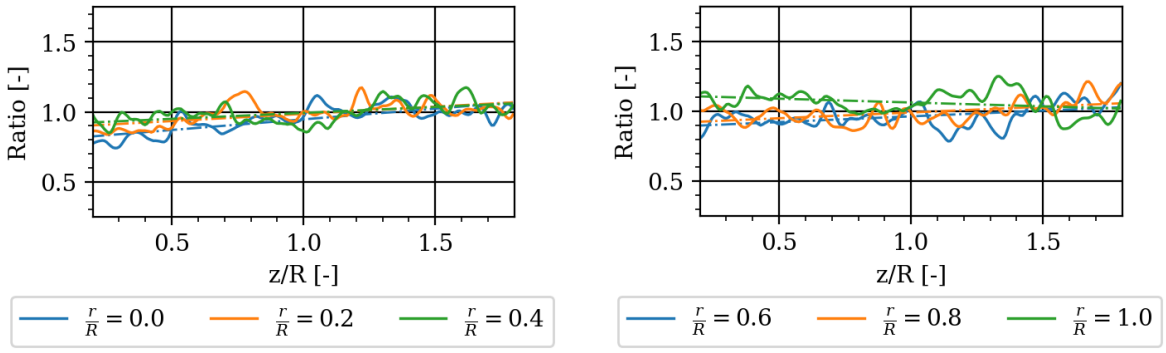

(a) (b)

Figure 5.6: Evolution of the ratio of streamwise to traverse mean velocity fluctuation $\overline{u'}$ and $\overline{v'}$ at (a) $r/R = 0, 0.2, 0, 4$ (b) $r/R = 0.6, 0.8, 1.0$. Linear trendlines depicted with dash dotted line.

The evolution of the streamwise and traverse velocity fluctuations at $r/R = 0.4$ are plotted in fig. 5.7a. Both $\overline{u'}$ and $\overline{v'}$ are found to decrease from $z/R = 1.8$ to $z/R = 0.2$. Moreover, the velocity fluctuations remain of equal magnitude. Similarly, the lengthscales L^x_{uu} and L^z_{vv} remain of equal magnitude and both increase as the rotor is approached, see fig. 5.7b. The evolution of intensities and lengthscales are in good agreement with the empirical results of Roach [57] describing turbulence decay behind a grid.

Both $\frac{\overline{u'}}{\overline{v'}}$ and $\frac{L^x_{uu}}{L^z_{vv}}$ are unity for isotropic turbulence. At $z/R = 1.8$ both ratios are approximately equal to 1. These ratios are conserved up to $z/R = 0.2$ and $z/R = 0.35$ for $\frac{\overline{u'}}{\overline{v'}}$ and $\frac{L^x_{uu}}{L^z_{vv}}$, respectively.

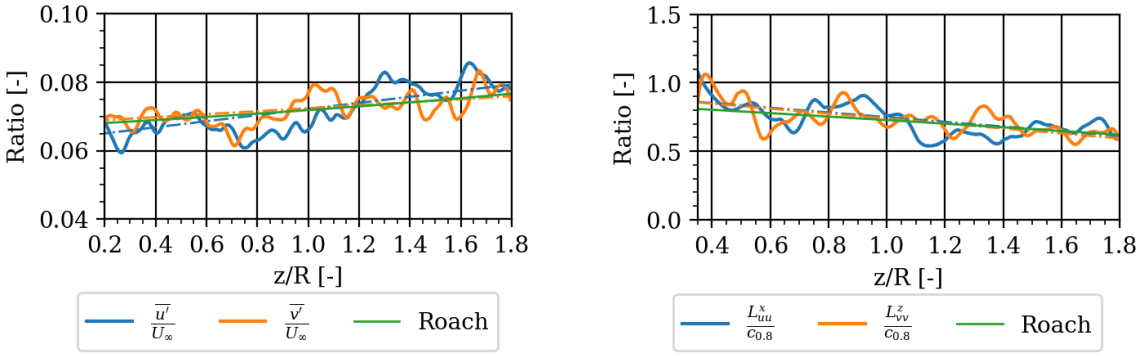

(a) (b)

Figure 5.7: Evolution at $r/R = 0.4$ of (a) streamwise and traverse velocity fluctuations and (b) lengthscales at. $U_\infty = 9m/s$ and $c_{0.8} = 2cm$. Empirical relation of Roach [57] is included.

Figure 5.8 shows the spectrum measured at the equivalent location most closest to the rotor in fig. 5.7. The peaks at the BPF, which are normally present, are removed using a notch filter such that the energy at the BPF and harmonics follows the trend of the surrounding frequencies. The integral under the remaining spectrum is computed to retrieve the turbulence intensity, see eq. (5.4) and recall the definition of E in section 2.2.

$$\overline{u'}^2 = \int_0^\infty E(f_{turb}) df_{turb} \tag{5.4}$$

In essence, the process of removing the spectral data at the BPF and harmonics is phaselocking in the spectral domain. From this procedure it follows that $\overline{u'}/U_\infty = \sqrt{0.297}/9 \approx 0.061$ which is in fair agreement with the PIV results. The integral lengthscale is estimated from PIV results because the blade passing cannot be removed from the hotwire time signal. The experiments match reasonably well with the Von Kármán spectrum (orange dashed line), as seen in fig. 5.8.

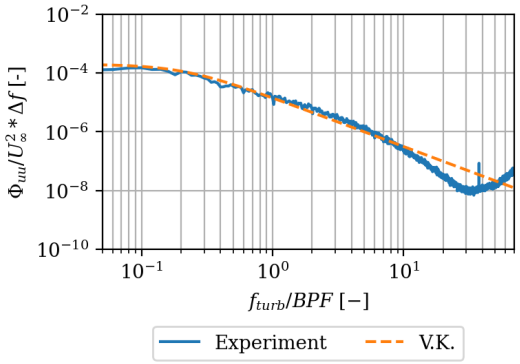

Figure 5.8: Hotwire spectrum compared with the Von Kármán spectrum at $r/R = 0.4$, $z/R = 0.2$. $U_\infty = 9m/s$ and $\Delta f = 5Hz$. Von Kármán inputs are the $\overline{u'} = 0.59m/s$ and $L^z_{uu} = 0.028m$.

5.4.2. Discussion

The largest decrease in $\frac{\overline{u'}}{\overline{v'}}$ is found at $r/R = 0$ in the experiments. This opposes theory, as the axial velocity was found to be lowest at that location. Hence, the vorticity lines undergo the least stretching. In fact, as the rotor is approached, the axial velocity decreases close to the rotor due the the blocking of the nacelle. The compression of vorticity lines theoretically leads to an increase of $\frac{\overline{u'}}{\overline{v'}}$. In the acoustic framework, however, this observation is of little importance as there is no turbulence interaction noise at $r/R = 0.0$.

The decrease of $\overline{u'}$ at $r/R = 0.4$ is in line with rapid distortion theory as there is stretching of the vorticity lines in streamwise direction. Analogously, an increase of L^z_{vv} is expected from RDT. However, the fact that $\frac{\overline{u'}}{\overline{v'}}$ and $\frac{L^x_{uu}}{L^z_{vv}}$ remain equal to 1 indicates that isotropy is conserved. Besides, still a good fit is observed with

the Von Kármán spectrum. This means that the distribution of turbulent kinematic energy over the turbulent frequencies does not change. The spectrum is expected to change when turbulence is distorted [28].

The evolution of the standard deviations and lengthscales at $r/R = 0.2, 0.6, 0.8$ and 1.0 are similar to what has been presented for $r/R = 0.4$. This claim is bolstered by the fact that at those locations the ratios presented in fig. 5.6b do not undergo a significant change. This implies that the turbulence spectrum remains isotropic across the radial locations as the rotor is approached. So there is no distortion of turbulence due to streamtube contraction.

The decay of the streamwise and traverse turbulence intensity, as well as the increase of the respective lengthscales, are in line with the evolution of turbulence behind a grid as described by Roach [57] and Ertunç [24]. This means that natural decay of turbulence plays a role. This violates one of the assumptions underlying rapid distortion theory. Therefore, when modelling the distortion of turbulence by the streamtube of an UAV propeller, one must take into account that the distortion is not rapid enough.

It is acknowledged that a set of $N \geq 300$ images is preferred for fully converged flow statistics. However, it was not possible to increase the number of images in the subset without losing confidence in the data. That is, the number of images in the subset could be increased. However, this means that there is more difference in the physical location of the blade between the images. This artificially increases the standard deviation of the velocity in the images, especially near the rotor plane, as it is then assumed that different flow situations are the same.

5.5. Turbulence distortion due to leading edge

During the acquisition the blade will not always be exactly at the same location. This increases the standard deviation but does not represent the physical situation, as described previously in section 5.4.2. In order to minimise the difference between the location of the blade between the images and gain confidence in the flow statistics, the set of 2000 images is processed. A subset of N = 150 images is retrieved. The images are taken at $r/R = 0.4$. In addition to $J = 0.225$, another flow case is analysed at $J = 0.3$. In both cases $U_\infty = 9m/s$. The argument for this is that the asymptotic solution presented in section 3.3.3 yields a function for the distortion depending on the leading edge radius along the stagnation streamline. In other words, the distortion of turbulence due to the leading edge along the stagnation streamline does not depend on relative velocity. Hence, the second flow case simply provides additional data on the distortion.

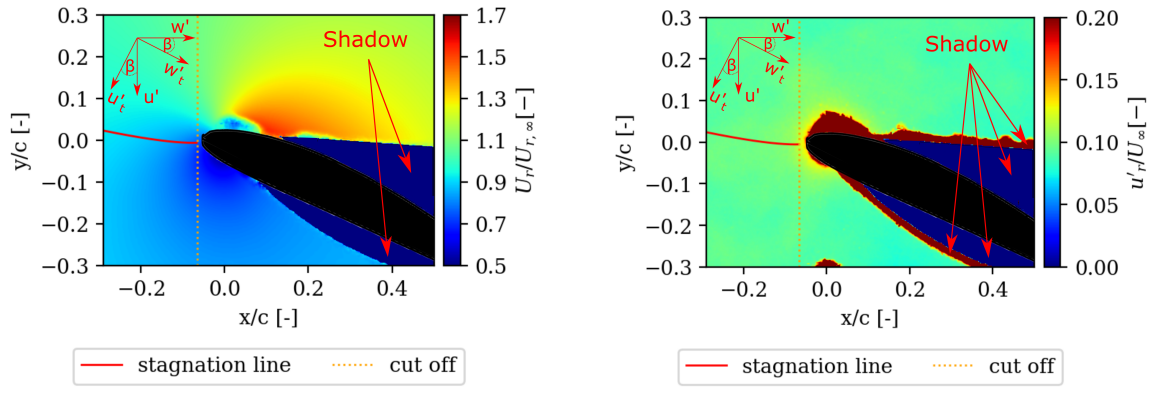

(a) (b)

Figure 5.9: (a) Mean velocity field and (b) standard deviation. $J = 0.3$, $U_r = \sqrt{U_\infty^2 + (\Omega r)^2}$, $U_\infty = 9m/s$, $r/R = 0.4$, $u'_r = \sqrt{u'^2 + w'^2}$. NACA-4412 airfoil in black.

In fig. 5.9, the mean velocity and standard deviation fields are given for $J = 0.3$ at $r/R = 0.4$. Due to the laser arrangement, there is a shadow on the suction side. On the pressure side there is the more inboard part occupying the image. Both effects lead to areas in the image where the in focus particles can not be detected. These areas are denoted with 'Shadow'. In both plots, the stagnation line is plotted. In order to choose this line, a mean velocity field is determined. The stagnation streamline is chosen as the line which approaches the leading edge, and does not curve around it.

The cut-off line represents the location up to which the standard deviation is assumed to be correct. As can be seen in fig. 5.9b, close to the leading edge of the measurements are corrupted. This is ascribed to the

effect of blade movement which affects the vectors most close to the leading edge.

To determine the velocity fluctuations in the blade frame of reference, u'_t, w'_t, the velocity fluctuations u', w', are transformed using eq. (5.5), where $\beta = 27°$ is based on fig. 4.1. This value for β aligns the velocity fluctuations in the direction parallel and perpendicular to the chord. This is done in order to remain in agreement with Amiet, of which a flat plate at zero angle of attack is the foundation.

$$\overline{u'^2_t} = \overline{u'^2} sin(\beta)^2 + \overline{w'^2} cos(\beta)^2 - 2cos(\beta)sin(\beta)\overline{u'w'} \tag{5.5a}$$

$$\overline{w'^2_t} = \overline{w'^2} sin(\beta)^2 + \overline{u'^2} cos(\beta)^2 + 2cos(\beta)sin(\beta)\overline{u'w'} \tag{5.5b}$$

The experimental and analytical ratios $\kappa_z = \frac{\overline{u'_t}}{\overline{u'}_{t,\infty}}$ and $\kappa_y = \frac{\overline{w'_t}}{\overline{w'}_{t,\infty}}$ are plotted in fig. 5.10. $\overline{u'}_{t,\infty}$ and $\overline{w'}_{t,\infty}$ are determined by averaging the first 50 points of the respective quantity along the stagnation streamline.

In both cases κ_z, which represents the upwash as experienced by the blade, follows a similar trend. From $x/r_{le} = -7.5$ it starts to increase up to the cut-off line which lies at $x/r_{le} \approx -2$ for both cases. The value for both cases is $\kappa_z \approx 1.25$. The increase is faster than expected from theory, and for that purpose eq. (3.25a) and eq. (3.25b) are modified with a factor $\alpha = 0.5$ as in eq. (5.6a) and eq. (5.6a).

$$\kappa_z = (1 + \frac{1}{(1-\alpha\xi)^2}) \tag{5.6a}$$

$$\kappa_y = (1 - \frac{1}{(1-\alpha\xi)^2}) \tag{5.6b}$$

For $J = 0.225$, κ_y increases slightly, but no clear trend can be identified. The behaviour of κ_y for $J = 0.3$ is different. Indeed, it first decreases to 0.9 after which it starts to increase again.

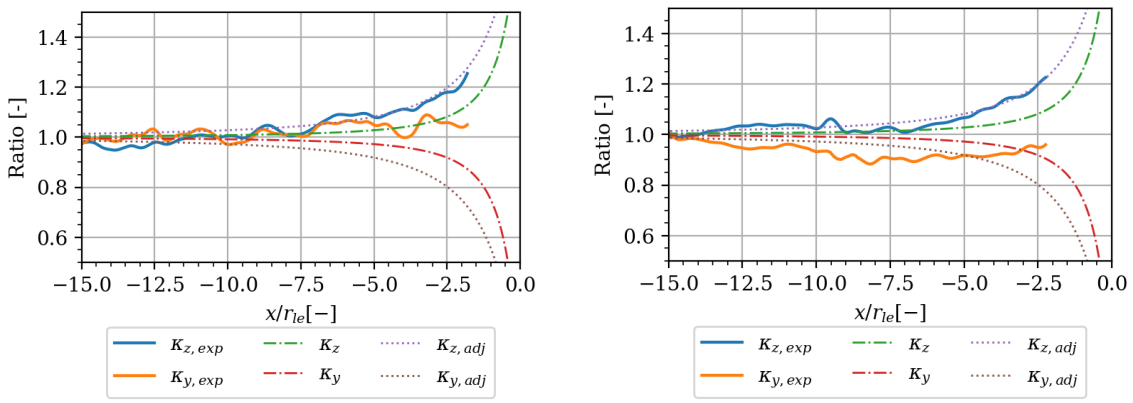

(a) (b)

Figure 5.10: Evolution of κ_z and κ_y. Experiment compared with original and adjusted asymptotic solutions of Hunt [43] at (a) $J = 0.225$ and (b) $J = 0.3$, where $U_\infty = 9m/s$.

5.5.1. Discussion

The factor $\alpha = 0.5$ in eq. (5.6a) and eq. (5.6b) can be interpreted as the doubling of the leading edge such that $\xi^* = \xi\alpha = \frac{x}{2r_{le}}$. It is known that boundary layers effectively increase a body's dimension [10]. However, it is unlikely that the boundary layer doubles the leading edge radius. Namely, near the stagnation point of a cylinder it thin enough to be neglected, as explained by Britter et al. [18]. At this point there is no evidence of a physical reason other than a better match with the experiments and it should be interpreted as such. Nevertheless, it demonstrates that the value $\overline{u'}$ should be modified in the definition of the Von Kármán spectrum eq. (2.6). This hypothesis is tested in section 5.6.

The correspondence with theory as shown by κ_z, albeit with a modification, does not hold for κ_y. From asymptotic theory it is expected to decrease. The trend of a stronger increasing upwash and a marginally increasing streamwise turbulent velocity has been observed by De Santana et al.[60] as well, see fig. 2.15. It is noted that their results are for a steady, symmetrical airfoil at zero angle of attack. This might indicate that the measured effect is truly the distortion of turbulence. However, measurements with clean inflow at the same

RPM should be performed using the propeller in order to isolate turbulence distortion from unsteadiness of the set-up. Moreover, the results of κ_y are within 10% of the upstream value at x/r_{le}. Since measurement uncertainty is related to $\frac{\overline{u'}}{\sqrt{N}}$, it is not possible to make definite statements about κ_y. In terms of acoustics it is of lesser importance how $\overline{w'_t}$ behaves as it is the upwash component $\overline{u'_t}$ that predominantly alters the loading of the blade.

Due to the uncertainty of the velocity very close to the leading edge, there is uncertainty in the determination of the stagnation line. Therefore, the standard deviation of a set of 10 possible stagnation lines is determined. For each line the value of κ_z is appended. The standard deviation of the value for κ is found to be 0.01, or 1% which is acceptable. Note that the standard deviation is dimensionless as κ_z represents a ratio. Upstream of the leading edge, $\overline{u'}_\infty$ and $\overline{w'}_\infty$ are of virtually equal magnitude. This bolsters the claim that isotropy is conserved up to the rotor plane.

5.6. Acoustics

The acoustic spectra are plotted in fig. 5.11 for microphone number 25. This is the microphone most perpendicular to the rotor rotational plane (x-y plane). Here, the turbulence ingestion noise is expected to have the largest effect, as has been shown analytically by Amiet [7] and experimentally by Simonich et al. [67]. The data from microphone 25 is used to validate the noise model in section 5.6.1 and to assess whether or not the findings on the distortion of turbulence improve the prediction.

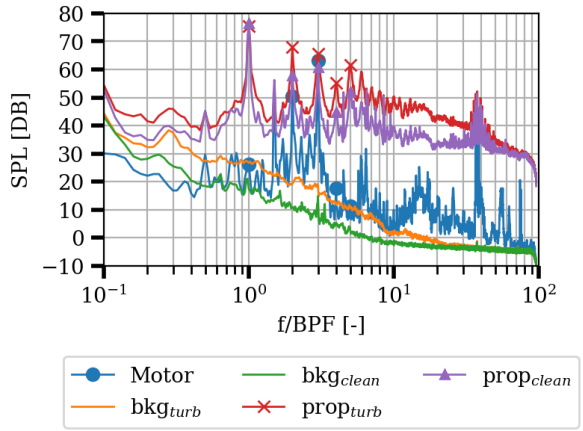

Figure 5.11: Acoustic spectra measured at microphone 25. $J_{turb} = 0.225$, $J_{clean} = 0.2$ and $\Omega = 8000RPM$. Markers are added for clarity purposes.

To isolate the aerodynamically generated noise it is necessary to characterise the contribution of the motor, the windtunnel and the grid. The two background noise spectra, denoted by bkg in fig. 5.11, show that the presence of the grid adds $10dB$ from BPF 0.1 to BPF 8. At higher BPF, the spectra quickly coincide. The minimal signal to noise ratio of the background noise in the windtunnel for clean inflow is equal to $5dB$ and found in the low-frequency range. At BPF 0.5 the ratio is $20dB$ and increases for higher frequencies. The signal to noise ratio for the turbulent flow case behaves similar as for the clean inflow case. The minimum signal to noise ratio found in the low-frequency range is $10dB$ for this case.

The motor spectrum shows a tone of $30dB$ at BPF 0.5, which is characteristic for such a spectrum as it resembles the (motor) rotational frequency Ω. Analogously, at BPF 1.5, a tone of $49dB$ is present. At BPF 2 and BPF 3, tones of $50dB$ and $60dB$ are measured. These tones are related to the number of poles $N_{poles} = 2$. This is a characteristic feature of brushless motors with harmonics of $\frac{\Omega N_{poles}}{60}$ [48]. In the high-frequency range, between BPF 30 and BPF 40, a series of spikes, associated with electrical motor noise, is present. At BPF 2 the signal to motor noise ratio (SNR) is $18dB$ and $8dB$ for the turbulent and clean case, respectively. At BPF 3 the SNR is $2dB$ for the turbulent and $-3dB$ clean inflow case. The minimum SNR in the high-frequency range equals $6dB$ for the clean inflow and $8dB$ for the turbulent inflow.

The respective background noise for turbulent inflow and motor noise are subtracted from the measurements at microphone 25 denoted with $prop_{turb}$, see fig. 5.11. The tone at BPF 1 is the same for both inflow cases. The tones at BPF 2 to BPF 20 are consistently higher for turbulent inflow, with a value of $10dB$, and

also broader. Moreover, the peak tones decrease with increasing BPF harmonic. Only BPF 4 does not fit this trend.

In order to appreciate the difference between the clean and turbulent inflow, the effect of the change in freestream velocity from $8m/s$ to $9m/s$ on steady loading and thickness noise is assessed. The velocity difference between the clean and turbulent inflow case is ascribed to the blocking of the grid, as explained in section 5.2. By means of a blade element momentum theory based noise model, the steady loading and thickness components for the propeller are computed at $J_{grid} = 0.225$ and $J_{clean} = 0.2$, where $\Omega = 8000rpm$. In this specific case, $J_{grid} = 0.225$ refers to the the freestream velocity only. No turbulence has been imposed on the flow in the steady simulation. A detailed description of the code is given by Casalino, Grande, Romani et al. [19]. The tonal and broadband spectra computed at the equivalent microphone location 25 are depicted in fig. 5.12a and fig. 5.12b, respectively.

It is evident that the difference of both the steady tonal and broadband components between the two velocities are small. Hence, the differences in SPL between the turbulent and clean inflow conditions, respectively prop_{turb} and prop_{clean}, in fig. 5.11 are ascribed to turbulence ingestion noise.

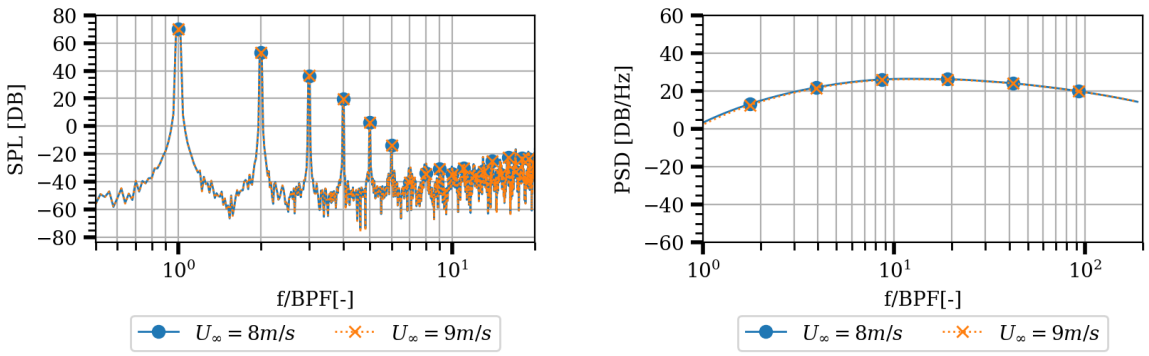

(a) (b)

Figure 5.12: Steady noise simulation at microphone 25 of (a) tonal noise SPL and (b) broadband noise PSD. $\Omega = 8000rpm$, $J_{grid} = 0.225$ and $J_{clean} = 0.2$. A set of points is marked with a circle and cross respectively for clarity purposes.

5.6.1. Analytical

In section 5.4 it was found that the there is almost no distortion of turbulence due to the streamtube contraction. The change in turbulence intensity and integral lengthscale is ascribed to natural decay of turbulence behind a grid. In addition, the results in section 5.5 suggest a 25% increase of the upwash fluctuation's magnitude which is a consequence of turbulence distortion caused by the leading edge. To assess the importance of both distortion mechanisms, the analytical model of section 3.2 is used. The modifications only concern the turbulence intensity, which serves as input for the turbulent spectrum. The steady noise predictions depicted in fig. 5.12 are added on top of that.

Based on those findings four cases, tabulated in table 5.2, are assessed. Case 1 defines the input as originally done by Amiet at $z/R = 3.0$. Case 2 models the same upstream turbulence spectrum, but now the distortion tensors following from $H\&O$ using $T/T_{exp} = 0.52$ are used to get insight on the theoretical effect. Case 3 uses the decayed spectrum as input for the noise model. The increase of turbulence intensity due to the leading edge is added on top of that in case 4. If the denoted tensor is 'none', then the distortion is not modelled.

Case	1	2	3	4
L^z_{uu} **[m]**	0.021	0.021	0.28	0.28
$\overline{u'}$ **[m/s]**	0.85	0.85	0.59	0.59
LE factor	1	1	1	1.25
Tensor	None	$C_{0.52}$	None	None

Table 5.2: Parameters used in analytical noise simulation.

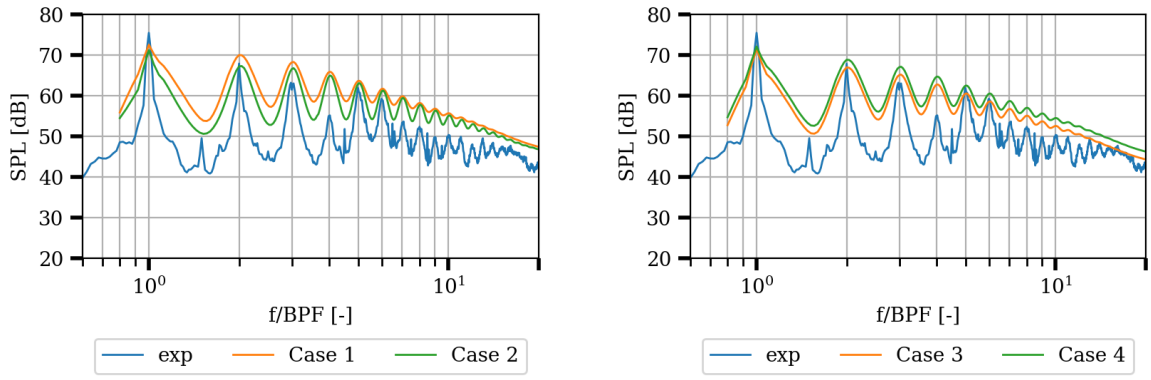

(a) (b)

Figure 5.13: Experimental spectrum measured at microphone 25 for $J = 0.225$ compared with analytical solution (a) case 1 and case 2 (b) case 3 and case 4.

The turbulence ingestion noise is modelled up to BPF 20. After that, the prediction decays rapidly. This poses no problem as airfoil self noise becomes dominant from there on, see fig. 5.12 or Amiet [6].

In fig. 5.13a the experimental spectrum with the background noise subtracted for the turbulent inflow is compared with the analytical model. It can be seen that the model underpredicts BPF 1 with 3.5 and $4dB$ respectively for case 1 and 2. The former overpredicts BPF 2 with $2dB$ where the latter is on point. Both cases overpredict the remainder of the tones up to BPF 20. Moreover, from BPF 5 onward, there is no difference between the predicted peak tones. The throughs, or the lows of the SPL, at the BPF half harmonics however, are substantially lower for case 2.

The predictions for cases 3 and 4 are presented in fig. 5.13b. The first BPF is underpredicted with $4.5dB$ and $2dB$ for case 3 and 4, respectively. At BPF 2, the differences are $1.7dB$ and $3.7dB$. Both modelled cases are in reasonable agreement with the experiment from BPF 3 up to BPF 6, except at BPF 4. From BPF 7 to BPF 20, the predictions of case 3 are more accurate than those of case 4. A maximum difference of $2.5dB$ is observed between case 3 and experiment in that range. The throughs at all half harmonics are overestimated by at least $8dB$ for both cases.

For all modelled cases, the width of the peaks at the BPF and harmonics are broader than what is measured experimentally.

5.6.2. Discussion

The motor noise is measured without freestream velocity and propeller. Therefore, it does not fully represent the motor noise. As described by Finley [29], the winding and mechanical noise should not increase by adding loads. The electromagnetic noise, however, does increase as more current is required to achieve the same rpm under loading. This induces a stronger magnetic field, hence stronger vibrations. Moreover, the interaction between the nacelle configuration and motor changes due to the propeller. Whether or not the latter effect adds or dampens the measured noise is not known for this experiment.

The low SNR at BPF 3 indicates that the spectra prop_{clean} and prop_{turb} are compromised by the motor noise at the location of microphone 25. Hence, the aeroacoustic noise can not be distinguished from the motor noise at BPF 3. Therefore, this tone is discarded from the analysis.

In fig. 5.11, it can be seen that at BPF 1 there is no difference between the turbulent and clean inflow case. This is confirmed by fig. 5.12, where the tone at BPF 1 is equal for both flow cases. This suggests that the steady loading and thickness noise are dominant at BPF 1, as expected. From BPF 2 onward the contribution of turbulence ingestion noise becomes clear. The tones up to BPF 20 are consistently higher for turbulent inflow, as is the broadband part of the spectrum up to BPF 40. This is in line with what has been found by Hagen et al. [39] and Amiet [6] for helicopters. However, Yauwenas et al. [77] did not find this distinct difference between both the tonal and broadband part of the spectrum for an UAV propeller. The tone at BPF 4 is lower than BPF 5. This does not correspond with the findings of Hagen et al.[39]. The fact that the same behaviour is observed for the clean inflow case suggests that it is related to the propeller and the operating conditions. Similarly, at BPF 15 to 20 there is a small hump in the clean and turbulent inflow spectra. These correspond with the hump found in the motor spectrum and is ascribed to the motor, just as the peaks at BPF 30.

Recalling the RPM variability in fig. 4.7, it was found that the RPM is varying more when turbulence is added to the flow. Besides the unsteady loading noise caused by the interaction with the turbulence, the varying RPM is in itself also a form of unsteady loading. Moreover, the larger the change in RPM, the larger the change in blade loading. The effect of RPM fluctuations on the unsteady loading noise can not be separated from the unsteady loading noise using the experimental acoustic data.

Case 1 and 2 in fig. 5.13a use the same upstream turbulence parameters, but the distortion of turbulence by the streamtube contraction is modelled using the results of section 5.1 in case 2. For case 1, it is assumed that the turbulence does not distort due to streamtube contraction. It can be seen that BPF1 to 4 are higher for case 1 than for case 2. This follows from the fact that stretching of vorticity lines decreases the streamwise velocity fluctuations which are associated with the upwash velocity of the blade. This is represented by case 2. Additionally, more blade-to-blade coherence is expected for case 2 as the eddies are stretched. This can explain why the energy is more centred around the harmonics than for case 1.

The computed spectra for the two flow case 3 and 4 in fig. 5.13b exhibit the same shape. This is expected because the only difference between the two is the amount of turbulent kinetic energy. In fact, only the magnitude is different with $10log_{10}(1.25^2) \approx 1.9$ as the square of the turbulence intensity is used in the Von Kármán definition. The underlying assumption is that from $z/R = 0.2$ to $z/R = 0.0$ there is no further change of the turbulent spectrum. This can not be confirmed by the PIV measurements as there is too much noise in that region. However, it is not known what location is the ideal location to define the spectrum. Therefore, the current location is assumed to be correct. Above all, there is already fair agreement between predictions and measurements at the BPF and harmonics.

The throughs are also predicted significantly higher than measured and the peaks are wider for all cases. Therefore, the model is not suitable to determine the overall sound pressure level (OASPL).

The use of the Von Kármán spectrum with turbulence statistics retrieved at $z/R = 0.2$ is justified by the fact that in fig. 5.8 good agreement is found with the experiment. However, it is not confirmed if this accurately represents the turbulence spectrum across the radius. Namely, in section 5.2 it was found that at $z/R = 2.0$ the turbulence intensity was lower at more outboard parts of the blade. If this is still true at $z/R = 0.2$, then the predictions can improve as currently the tones are predicted too high.

5.7. Assessment of analytical hypothesis

In section 3.5 a set of hypothesis was presented which serve as the ground for the analytical models. These will be held against the experimental results presented above. The hypothesis are repeated below.

Hypothesis 1. *The mean flow model of H&O accurately predicts the mean flow upstream of the propeller.*

False. It was found that in order to match the predicted streamtube contraction with the experimental results from PIV, the input thrust in eq. (3.4) should be 52% of the thrust that was measured using the loadcell.

Hypothesis 2. *The turbulent velocity fluctuations are sufficiently small such that they are only advected with the local mean flow, and do not change it.*

True. The ratio $\frac{\overline{u'}}{U_\infty} = .093$ at $z/R = 3.0$ and $\frac{\overline{u'}}{U_\infty} = 0.065$ at $z/R = 0.2$. This satisfies Taylor's frozen hypothesis. The same holds for the turbulence intensity in front of the leading edge, as can be seen from fig. 5.9b.

Hypothesis 3. *The distortion of turbulence by the streamtube contraction and leading edge occur sufficiently rapid.*

False. For the distortion due to the streamtube contraction it is found that $\frac{\overline{u'}R}{U_a L^z_{uu}} \approx 0.55$, which is not 'much smaller' than 1. Here, $U_a = 9m/s$ Therefore, the distortion is not rapid enough. For the distortion by the leading edge $\frac{\overline{u'}r_{l.e.}}{U_a L^z_{uu}} \approx 0.003$. In this case, $U_a = 37.5m/s$ for $J = 0.3$. So, this distortion mechanism is rapid.

Hypothesis 4. *The turbulence lengthscale is small with respect to the propeller radius and large with respect to the leading edge radius.*

True. Based on the hotwire measurements at $z/R = 3.0$, $\frac{L^z_{uu}}{R} = 0.15 \leq 0.55$. The PIV measurements yield $\frac{L^z_{uu}}{r_{l.e.}} = 60 \geq 5$ at $r/R = 0.4$. Hence, the vorticity distortion and blocking effects described in section 3.3 can be used for the distortion of turbulence by streamtube and leading edge, respectively.

Hypothesis 5. *The observer is located in the far-field, where Amiet's theory is valid.*

True. Microphone 25 is at 1.55m from the propeller centre. For BPF 1, the acoustic wavenumber $kr = \frac{2\pi}{\lambda} r = \frac{2\pi}{1.28} * 1.56 = 7.6[1/m]$. Here, λ is the acoustic wavelength and r the distance to the microphone. Since $kr >> 1$, the microphone is in the far-field and predictions Amiet's theory can be compared with the microphone data.

6

Conclusions and recommendations

In this chapter the main findings are summarised by answering the research questions and additional results are reported. The chapter ends with a set of recommendations for future research.

6.1. Conclusions

A small-scale UAV propeller operating at $10^4 < Re_c < 10^5$ has been subjected to an isotropic turbulent flow generated by a grid placed at the windtunnel nozzle. The freestream velocity was equal to $9m/s$ and $\Omega = 8000RPM$. A mean flow model has been used to analytically describe the distortion of turbulence by the streamtube contraction. This has been compared with experimental data coming from PIV and hotwire measurements. Similarly, the distortion of turbulence due to the leading edge has been modelled analytically and has been compared with phaselocked PIV measurements at $r/R = 0.4$. The information of turbulence that has been retrieved was coupled to farfield noise measurements by means of Amiet's rotor noise model.

The findings are coupled to the research questions stated in chapter 2 which are repeated here.

1. What is the distortion of an upstream isotropic turbulence spectrum due to the contracting streamtube as the turbulence approaches a low Reynolds number propeller in low speed forward flight?

   - What is the degree of isotropy at the rotor face? *Isotropy implies that the ratio of streamwise to traverse velocity fluctuations is unity. Downstream anisotropy means that this ratio has changed. This does not happen for when turbulence decays naturally in the flow. Hence, it can be deduced that turbulence has been distorted*

     It is found that the contraction ratio is $C = 1.3$, which is small. Hence little distortion is expected based on the theory of Batchelor and Proudman. The PIV measurements confirm this. It reveals that the ratios $\frac{\overline{u'}}{v'}$ and $\frac{L^x_{uu}}{L^z_{vv}}$ are unity at $z/R = 1.8$ and remain so up to $z/R = 0.2$ for the former and $z/R = 0.35$ for the latter. Closer to the rotor the data is influenced by the blade and no distinction can be made between the upstream turbulence and velocity fluctuations coming from the blade. Since a change in $\frac{\overline{u'}}{v'}$ implies a change in $\frac{L^x_{uu}}{L^z_{vv}}$ according to rapid distortion theory, it is concluded that turbulence is not distorted by the streamtube contraction. Consequently, it is not required to model this phenomenon for this flow case.
   - What is the change of the streamwise turbulence intensity at the rotor face compared to the upstream turbulence intensity? *The streamwise component is the main component of the upwash fluctuations in the blade frame of reference. A change of this component yields a change in observed sound.*

     The upstream turbulence intensity equals 9.3% at $z/R = 0.3$ and reduces to 6.5% at $z/R = 0.2$, as followed from both hotwire and PIV measurements. The decrease of intensity is accompanied by an increase of lengthscale. As stated before, isotropy is conserved so the change in the respective parameters is not caused by the contraction of the streamtube. Rather, the observation is ascribed to the natural decay of turbulence behind a grid as has been described by Roach [57].

2. Does the neglecting of leading edge distortion in the analytical model lead to large discrepancies in the computed and observed noise?

- How does the intensity of the turbulence upwash component evolve as it approaches the leading edge? *This is the main indicator if leading edge distortion is relevant as it governs the emitted noise.*

  The upwash component in the blade frame of reference, $\overline{u_t'}$, starts to increase from 7.5 leading edge radii upstream of the blade. At $x/r_{le} = -2$ the component is 25% higher than the upstream value. This is observed for two flow cases at $J = 0.225$ and $J = 0.3$, respectively. The trend that is seen does not follow the asymptotic results of Hunt[43]. However, when the theoretical results are modified with a factor $\alpha = 0.5$, good agreement is found with experiments. No physical reason for this factor is known other than a better match with experiments.

- Can the difference in the observed noise be ascribed to the neglecting of the leading edge distortion? *This sheds light on the relevance of leading edge distortion in the analytical model.*

  The difference between the observed noise and the prediction can not be ascribed to leading edge distortion. Four sets with different input parameters for the turbulence spectrum were used. It is found that the tones are already overpredicted when the leading edge distortion is not taken into account. Hence, an additional increase in turbulence intensity, which is in line with observations, lead to a larger difference between the model and experiment.

In addition to the above, other conclusions can be drawn from the experimental and analytical campaign:

- A significant difference between the mean flow model of Hough and Ordway (H&O) and the experiments is found. In order to match the experimentally derived upstream mean flow field the input thrust T had to be 52% of the experimental value T_{exp}. Similar corrections were deemed necessary in literature, see Robinson [58]. Besides, the difference in streamtube and velocity at the rotor, the circulation distribution for the propeller is different than what is assumed in H&O.

  Therefore, it is concluded that this model is not suitable to predict the upstream flow field induced by the small-scale UAV propeller.

- The analytical predictions are in reasonable agreement with the experimental results at the blade passing frequency (BPF) and higher harmonics. When the decay of turbulence is accounted for, the predictions matches best. BPF 1 is underpredicted, but this is associated with steady loading and thickness noise. The maximum difference between prediction and experiment is $3dB$ for BPF 2 to BPF 6. Except, at BPF 4, there the experimental tone is significantly lower which is not in line with theory. The maximum difference for BPF 7 to BPF 20 is $8dB$.

  This shows that the decay of turbulence is an important phenomena as the propeller is approached. Moreover, it violates one of the assumptions of rapid distortion theory (RDT) which shows that RDT is not be valid for the distortion of turbulence by streamtube contraction.

  The model performed poorly at the half harmonics, which were overestimated. Moreover, the width of the peaks is wider than experiment. Hence, Amiet's model in its original form should not be used for OASPL purposes.

6.2. Recommendations

- To assess the leading edge distortion it is advised to triple the number of PIV images to 6000 such that a subset of at least 300 images remains after filtering. Alternatively, a lower RPM can be chosen such that the RPM fluctuations become less detrimental. In this way, more certainty in the results can be achieved. Then, the physical meaning, if any, of the factor α can be investigated as well.

- Following the previous point, a set of images should be taken without turbulent inflow. This has been done for the more outboard locations, but the fluctuations in RPM resulted in too little images and artificial velocity fluctuations purely because of the blade's movement. The clean inflow case sheds more light on the questions whether the observed distortion is due to the leading edge, or due to unsteady effects. An example of such an unsteady effect is the RPM fluctuation, which are always present when working with propellers.

- The experiments were performed in the limits of PIV in the sense that the observed change in standard deviation is of similar order as the uncertainty. To investigate the turbulence distortion and in order to appreciate the results, the turbulent fluctuations should be higher with respect to the mean flow.

This can be achieved by modifying the grid and flow parameters. Another suggestion is to scale up the propeller such that higher resolution is obtained in terms of leading edge radii. That is, most distortion is expected close to the leading edge. Thus, if the leading edge is larger, the absolute distance at which significant changes can be observed is larger and the effect of the blade movement becomes smaller.

- More flow cases have to be tested in order to generalise the conclusion of streamtube distortion not being important. It might be that for specific operating conditions the distortion is rapid enough and does play a significant role.
- The motor used in the experiment contaminated the acoustic spectrum of the propeller at BPF 2 and BPF 3. This is related to the number of poles, which is 2. For future experiments it is advised to use a brushless motor with at least 10 poles or more. In that way, the dominant tones up to BPF 5 will most likely not be affected.
- The chocking effect of the turbulence grid must be characterised before the propeller is turned on. Then, the windtunnel's RPM can be adjusted in such a way that the freestream velocity is the same for both clean and turbulent inflow conditions. In this way a more fair comparison can be made between the clean and turbulent inflow conditions.
- The lengthscales were determined using PIV. This is achieved by spatial correlation. If there is a change in flow along the correlation distance, such as the presence of the blade, the turbulent fluctuations can not be correlated. Hence, $z/R = 0.35$ is the closest location where lengthscale information could be retrieved. To solve this, the hotwire can be coupled to the encoder such that the time signal is not corrupted by the blade's passage. Then, using time correlation the lengthscales can be determined.
- A further study on the effect of the varying RPM on the measured noise should be quantified. In that way, the turbulence interaction noise can be fully isolated.

A

Supplementary to mean flow model

A.1. Legendre functions

The Legendre fucntion Q and its derivative Q' with respect to ω are given by

$$Q_{n-1/2}(\omega) = \int_{-\pi/2}^{\pi/2} \frac{cos(2n\alpha)}{\sqrt{2(\omega-1)+4sin^2(\alpha)}} d\alpha \tag{A.1}$$

$$Q'_{n-1/2}(\omega) = -\int_{-\pi/2}^{\pi/2} \frac{cos(2n\alpha)}{(2(\omega-1)+4sin^2(\alpha))^{3/2}} d\alpha \tag{A.2}$$

and w' by

$$w' = 1 + \frac{x^2 + (r-r')^2}{2rr'} \tag{A.3}$$

A.2. Airfoil in rectilinear motion

Assume a gust is of the form

$$\tilde{w_g} = w_R(k_x, k_y) e^{-i(k_x(x-U_c t)+k_y y)} \tag{A.4}$$

is interacting with the airfoil. The complete Fourier representation of the velocity field is

$$w_g(x - U_c t, y) = \int\int_{-\infty}^{\infty} \tilde{w_g} dk_x dk_y \tag{A.5}$$

where $x - U_c t$ means that the gust is convected with velocity U_c. Because of the no flow condition through the airfoil, a surface dipole distribution is induced to oppose the flow. This leads to a pressure jump

$$\Delta p(x, y, t; k_x, k_y) = 2\pi\rho_0 U_c w_R(k_x, k_y) g(x, \bar{k_x}, \bar{k_y}, M) e^{i(k_x U_c t - k_y y)}. \tag{A.6}$$

This is valid for a flat plate. In other words, the theory models the airfoil as an unloaded flat plate responding to an unsteady upwash fluctuation.The total pressure jump is caused by the contribution of all wavenumbers i.e.

$$\Delta p(x, y, t) = 2\pi\rho_0 U_c \int\int_{-\infty}^{\infty} w_R(k_x, k_y) g(x, \bar{k_x}, \bar{k_y}, M) e^{i(k_x U_c t - k_y y)} dk_x dk_y. \tag{A.7}$$

Of more interest is the frequency of the total pressure jump, as this is associated with the observed acoustic frequency, hence a Fourier transform to the frequency domain is performed to obtain

$$\Delta p(x, y, \omega) = 2\pi\rho_0 U_c \int_{-\infty}^{\infty} w_R(\lambda, k_y) g(x, \bar{\lambda}, \bar{k_y}, M) e^{-ik_y y} dk_y \tag{A.8}$$

where $\lambda = \omega / U_a$. This last statement means that a certain frequency component of the pressure jump is generated by the chordwise turbulence wavenumber. The pressure jump Δp can be viewed as the result of a

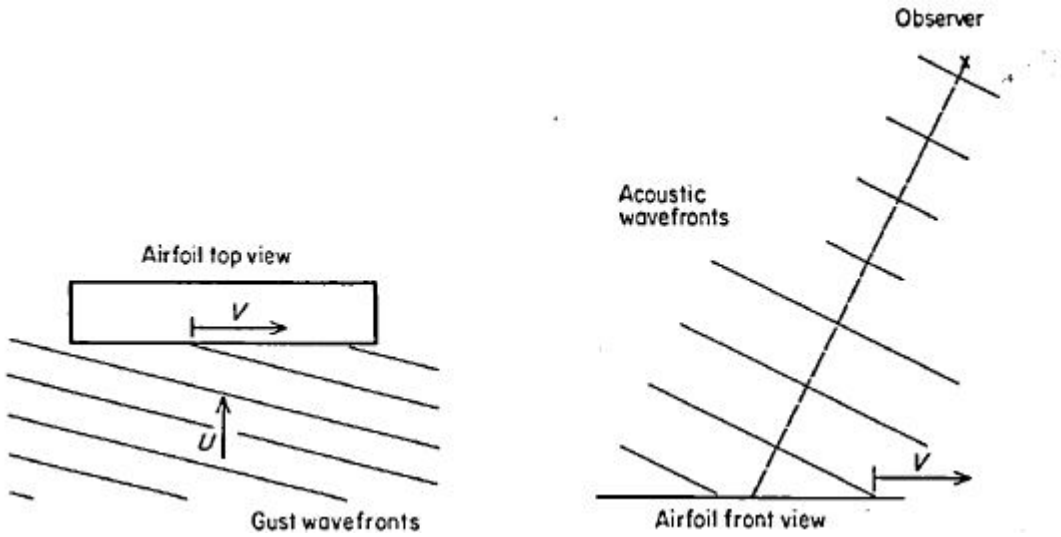

Figure A.1: Caption

force imposed on the medium leading to a dipole pressure response. For a point dipole with strength $F_z e^{i\omega t}$ located at (x_1, y_1) the far field pressure equals

$$p_0 = \frac{iF_z\omega z}{4\pi c_0\sigma^2} e^{i(\omega t+\mu(Mx-\sigma))} e^{-i\mu(Mx_1-(xx_1+\beta^2 yy_1)/\sigma)}. \tag{A.9}$$

The force is described by eq. (A.8) and is substituted in eq. (A.9). To obtain the total far-field pressure, the expression is integrated over the chord and span leading to

$$p(\mathbf{x},\omega) = \frac{i\omega z\rho_0}{2c_0\sigma^2} e^{i(\omega t+\mu(Mx-\sigma))} \int_{-d}^{d}\int_{-b}^{b} e^{-i\mu(Mx_1-(xx_1+\beta^2 yy_1)/\sigma)} \int_{-\infty}^{\infty} w_R(\lambda,k_y) g(x,\bar{\lambda},\bar{k_y},M) e^{-ik_y y} dk_y dx_1 dy_1 \tag{A.10}$$

Now, an effective lift function $\mathscr{L}$ is defined which can be interpreted as the coupling between the incoming turbulence and observed sound

$$\mathscr{L}(\bar{\lambda},\bar{k_y},M) = \frac{1}{b}\int_{-b}^{b} g(x_1,\bar{\lambda},\bar{k_y},M) e^{-i\mu x_1(M-x/\sigma)} dx_1. \tag{A.11}$$

The integration over the span is yields a factor Λ, where it is assumed that there is little variation of the airfoil along the span (on the scale of turbulence disturbance).

$$\Lambda = \frac{\sin^2(d(k_y-\mu\beta^2 y/\sigma))}{(k_y-\mu\beta^2 y/\sigma)^2} \tag{A.12}$$

Hence, eq. (A.9) can be written as

$$p_T\mathbf{x},\omega = i\frac{b\omega z\rho_0}{c_0\sigma^2} e^{i(\omega t+\mu(Mx-\sigma))} \int_{-\infty}^{\infty} w_R(\lambda,k_y)\mathscr{L}(\bar{\lambda},\bar{k_y},M)\Lambda dk_y \tag{A.13}$$

. The integral in eq. (A.13) cannot be integrated exactly. However, when it is assumed that the upwash disturbance is small with respect to the airfoil span i.e. λd$\gg 1$, the integral will show oscillating behaviour of which the contributions cancel each other except at $k_y = \mu\beta^2 y/\sigma = K_y$. Moreover, if d is large with respect to semichord b, then $\lim_{d\to\infty}\Lambda = \delta(k_y-\mu\beta^2 y/\sigma)$. So, the integral only produces a non-zero result if $k_y = \mu\beta^2 y/\sigma = K_y$. The physical interpretation is the fact that only a wave normal to the line joining the observer and airfoil is heard by the observer, as shown in fig. A.1.

Furthermore, according to Graham[36], if $MK_x \gg k_y$ the lift response function $\mathscr{L}$ and the gust w_R become independent of k_y so those can be taken out of the integral. This yields

$$p_T(\mathbf{x},\omega) = i\frac{\pi\omega bz\rho_0}{c_0\sigma^2} w_R(\lambda,K_y)\mathscr{L}(\bar{\lambda},\bar{K_y},M) e^{i\mu(Mx-\sigma)} \tag{A.14}$$

. Turbulence, however, is not a deterministic quantity. Therefore, w_R is not a single value. Without going into the mathematical foundations, the following relations are used to couple the expected values of a statistical quantity like turbulence to the far field spectrum

$$E[p_T(\omega)p_T\star(\omega)] = (T/\pi)S_{pp}(\omega) \tag{A.15}$$

$$E[w_R(\lambda,K_y),w_R\star(\lambda,K_y)](Rd/\pi^2)\Phi_{ww}(\lambda,K_y) \tag{A.16}$$

. The farfield power spectral density function for an airfoil interacting with turbulence described by an upwash spectrum Φ_{ww} is

$$S_{pp}(\omega) = (\frac{\omega bz\rho_0}{c_0\sigma^2})^2\pi U_c d|\mathscr{L}(\bar{\lambda},\bar{K_y},M)|^2\Phi_{ww}(\lambda,K_y) \tag{A.17}$$

A.3. Extension to rotor

For a rotor that chops an eddy multiple times there will be correlation between the instanteneaous spectra. The correlation function is written as

$$R_{pp}(\mathbf{x},\gamma,\tau) = \Sigma_{n=-\infty}^{\infty}R_{pp}^n(\mathbf{x},\gamma,\tau-nT2) \tag{A.18}$$

, where $T2$ is the time, as heard by the observer, between the chopping of a given eddy by the blades. The derivation of T_2 is found in appendix A. The correlation can be transformed to a spectral density by a Fourier transform

$$S'_{pp}(\mathbf{x},\gamma,\omega_0) = \Sigma_{n=-\infty}^{\infty}S_{pp}^n(\mathbf{x},\gamma,\omega_0)e^{in\omega_0T_2} \tag{A.19}$$

. This function is the spectral density with movement relative to the observer, indicated with $'$. It can be related through a Doppler factor $\frac{\omega}{\omega_0}$, where ω_0 is the frequency at the blade, as

$$S'_{pp}(\mathbf{x},\omega) = \frac{\omega}{\omega_0}S_{pp}(\mathbf{x},\omega_0,\gamma) \tag{A.20}$$

so that from eq. (A.17)

$$S_{pp}^{'(n)}(\mathbf{x},\gamma,\omega_0) = \int_{-\infty}^{\infty}\frac{\omega}{\omega_0}(\frac{\omega bz\rho_0}{c_0\sigma^2})^2\pi U_c d|\mathscr{L}(\bar{\lambda},\bar{K_y},M)|^2\Phi_{ww}(\lambda,K_y,K_z)e^{ik_znZ}dk_z \tag{A.21}$$

. The factor e^{ik_znZ} is required since a third dimension in terms of wavenumbers is added to the original two-dimensional i.e. k_x,k_y analisys of an airfoil in rectilinear motion. The wavenumber k_z accounts for the possiblity of multiple choppings of a single eddy. The function in eq. (A.21) denotes the acoustic spectrum of the n^{th} chop of a given eddy.

eq. (A.21) is supstituded in eq. (A.19). By realizing that $\Sigma_{n=-\infty}^{\infty}e^{in2\pi(\frac{k_zZ+\omega_0T_2}{2\pi})} = \Sigma_{n=-\infty}^{\infty}\delta(n+(\frac{k_zZ+\omega_0T_2}{2\pi}))$ it can be derived that the integral over k_z is only defined where $K_z^n = \frac{\omega_0T_2+2\pi n}{Z}$. Hence, the final result is

$$S_{pp}^{'}(\mathbf{x},\gamma,\omega_0) = \frac{\omega}{\omega_0}(\frac{\omega bz\rho_0}{c_0\sigma^2})^2\pi U_c d|\mathscr{L}(\bar{\lambda},\bar{K_y},M)|^2b^2\bar{u^2}\Sigma_{-\infty}^{\infty}\Phi_{ww}(\lambda,K_y,K_z^n)\frac{2\pi}{b^2\bar{u^2}Z} \tag{A.22}$$

The power spectral density is obtained by averaging eq. (A.22) over the azimuth and multiplying it by the number of blades B

A.4. Frame of reference transformation

In the analysis the axial flow has a Mach number M_z, and the side flow M_f. The blade segment is at angle γ from the x-axis and the side flow comes at an angle Ψ. See fig. 3.3 for reference. Since in the analysis the blade is assumed to be an unloaded flat-plate, the angle of attack α equals

$$cot(\alpha) = \frac{M_t+M_f\cos(\gamma+\Psi)}{M_z} \tag{A.23}$$

where M_t is the local tip Mach number of the blade segment. For skewed inflow, the blade will experience a spanwise component of flow over the blade

$$\mathbf{M_a} = -M_f\sin(\gamma+\Psi)(\hat{i}\cos\gamma+\hat{j}\sin(\gamma)) \tag{A.24}$$

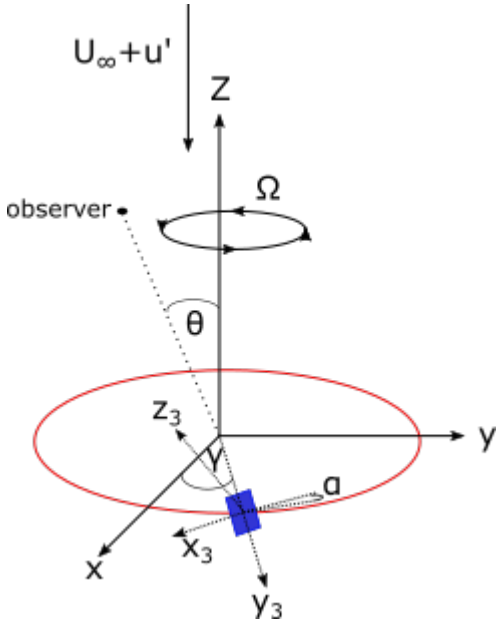

Figure A.2: Caption

and so the flow experienced by the blade segment is

$$\mathbf{M_b} = [M_t + M_f \cos(\gamma + \Psi)](-\hat{i}\sin(\gamma) + \hat{j}\cos(\gamma)) + \hat{k}Mz \tag{A.25}$$

. In order to use eq. (A.17), the observer coordinates must be transformed to the blade frame of reference. Additionally, when the observer hears the sound burst, at time T_e, the source has moved. Initially the observer is at

$$\mathbf{x_0} = r(\hat{i}\sin(\theta) + \hat{k}\cos(\theta)) \tag{A.26}$$

and the distance to the retarded source point $\mathbf{x_s}$ is

$$r_e^2 = (r\sin(\theta) - x_s)^2 + y_s^2 + (r\cos(\theta) - z_s)^2 \tag{A.27}$$

. Note that $\mathbf{Mz} = -M_z\hat{k}$, $\mathbf{M_f} = -M_f(\hat{i}\sin(\Psi) + \hat{j}\cos(\Psi))$ and $T_e = r_e/c_0$. Then

$$\mathbf{x_s} = [-M_f r_e \sin(\Psi), -M_f r_e \cos(\Psi), -M_z r_e] \tag{A.28}$$

. The distance to the retarded source point can subsequently be expressed in flow parameters as

$$r_e = r(M_s\cos(\Theta) + \sqrt{1 - M_s^2\sin^2(\Theta)})/(1 - M_s^2) \tag{A.29}$$

where $Ms^2 = M_f^2 + M_z^2$ and $M_s\cos(\Theta) = M_f\sin(\Psi)\sin(\theta) + M_z\cos(\theta)$. The present source position can then be found using $\mathbf{x_p} = \mathbf{x_s} + \mathbf{M_b}c_0T_e$. For this position of the source, the observer is at $\mathbf{x_1} = \mathbf{x_0} - \mathbf{x_p}$. The rotation to arrive from the rotor hub frame of reference to the blade frame of reference is

$$\mathbf{x_3} = \begin{bmatrix} \sin(\gamma)\cos(\alpha) & -\cos(\gamma)\cos(\alpha) & -\sin(\alpha) \\ \cos(\gamma) & \sin(\gamma) & 0 \\ \sin(\alpha)\sin(\gamma) & -\cos(\gamma)\sin(\alpha) & \cos(\alpha) \end{bmatrix} = \mathbf{x_1} \tag{A.30}$$

A.5. Doppler factor

The Doppler factor is defined by Amiet[3] as

$$\frac{\omega_0}{\omega} = 1 + \frac{\mathbf{M_t}\hat{\mathbf{SO}}}{1 - \mathbf{M_r}\hat{\mathbf{SO}}} \tag{A.31}$$

where $\mathbf{M_t} = M_t(-\hat{i}sin(\gamma)) + \hat{j}cos(\gamma)$ is the Mach number of the source relative to the observer and $\mathbf{M_r} = \hat{i}(M_f sin(\Psi) - M_t sin(\gamma)) + \hat{j}(M_f cos(\Psi) + M_t cos(\gamma)) + \hat{k}M_z$ the Mach number of the source relative to the fluid. $\hat{SO}$ is the unit vector from the retarded source position to the observer.

Hence, the Doppler factor can be rewritten as

$$\frac{\omega_0}{\omega} = 1 + \frac{M_t(xsin(\gamma) - M_f r_e cos(\gamma + \Psi))}{1 - (r_e(M_s^2 + M_t M_f cos(\gamma + \Psi)) + M_z z + xM_f sin(\Psi) - M_t sin(\gamma)x)} \tag{A.32}$$

It is shown by Amiet [5] that eq. (A.31) can be rewritten to

$$\frac{\omega}{\omega_0} = \frac{1 + M_t x'/r}{1 - M_z cos(\theta)}. \tag{A.33}$$

This equation reduces to the well known Doppler factor for a non-rotating source if $M_t = 0$.

A.6. Derivation of T2

The time T_2 is the time between the chops of a given eddy as heard by the observer. In fig. A.3 the process is depicted. The blade moves along line AD with velocity $V_t = \Omega R$. After time T_1 the blade has moved

$$FE = T_1 V_z, \tag{A.34}$$

where V_z is the convective velocity of the eddy at the rotor plane. The eddy has also moved

$$FC = T_1 V_f cos(\gamma + \Psi) \tag{A.35}$$

in the rotor plane. Here, V_f is the skewed inflow velocity component at the rotor plane. The distance

$$BC = (T - T_1)V_t \tag{A.36}$$

where T is the time of blade 1 at point C. Using Pythagoras theorem, the distance Z, which is the shortest distance of the blade paths in the fluid, is determined as

$$Z^2 = BF^2 + FE^2 = T_1^2 V_z 2 + ((T - T_1)V_t - T_1 V_f cos(\gamma + \Psi))^2 \tag{A.37}$$

$$Z^2 = T^2 V_t^2 - T_1^2(V_z^2 + (V_t + V_f cos(\gamma + \Psi))^2) \tag{A.38}$$

Solving simultaneously yields

$$Z = TV_t sin(\alpha) \tag{A.39}$$

$$T_1 = T(V_t/V_z)sin(\alpha)cos(\alpha). \tag{A.40}$$

T_2 is T_1 plus the time difference between the sound from point B and point C to reach the observer. The time from point C to reach the observer τ_0

$$\tau_0 = \frac{M_b x - \sigma}{c_o \beta_b^2} \tag{A.41}$$

replacing x by $x + BC$ and y by $y - T_1 V_f sin(\gamma + \Psi)$ gives T_1. So

$$T_2 = T_1 + BC(M_b - x/\sigma)/(\beta_b^2 c_0) + Y y/(c_0 \sigma) \tag{A.42}$$

where $Y = T_1 V_f sin(\gamma + \Psi)$.

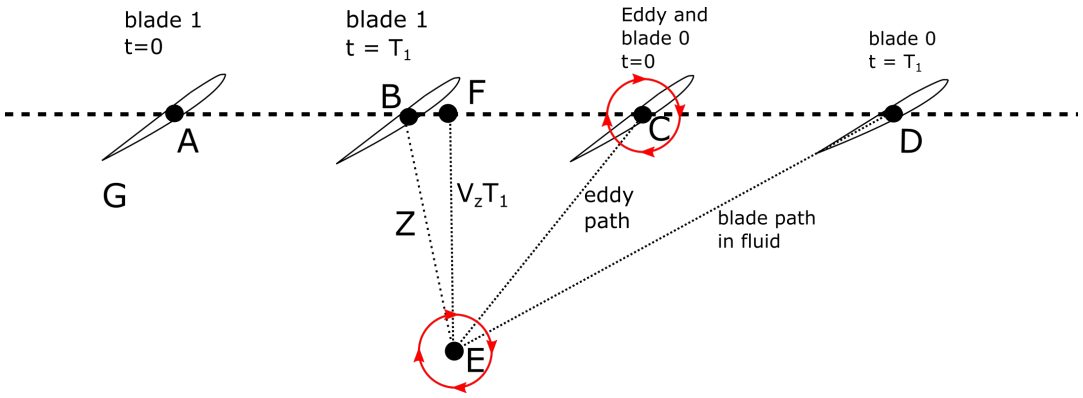

Figure A.3: Schematic representation of the multiple chopping of an eddy

A.7. Wavenumber and velocity relation

To model the distortion i.e. relate the upstream turbulence wavenumbers and vorticity to the downstream ones the following analysis is presented by Amiet[9].

The turbulence wavevector is defined by

$$\mathbf{k} = \hat{\imath} k_x + \hat{\jmath} k_y + \hat{k} k_z. \tag{A.43}$$

The velocity field $\mathbf{q}$ of a single wavevector Fourier component can be written as

$$\mathbf{q}^d(\mathbf{k}^d, \mathbf{x}) = \mathbf{Q}^d(\mathbf{k}^d) e^{i\mathbf{k}^d \mathbf{x}}. \tag{A.44}$$

The superscript d is used to denote the downstream location whearas u will be used to denote the upstream location. The first assumption is that flow is incompressible, this implies that $\mathbf{k^{d,u}}$ and $\mathbf{Q^{d,u}}$ are orthogonal and therefore

$$\mathbf{Q}(\mathbf{k}) = \mathbf{k} \times \mathbf{P}(\mathbf{k}) \tag{A.45}$$

for some vector $\mathbf{P}$. This relation holds for both the upstream and downstream region. The vorticity ω is defined as

$$\boldsymbol{\omega} = \bigtriangledown \times \mathbf{q} = i\mathbf{k} \times \mathbf{Q}(\mathbf{k}) e^{i\mathbf{k}\bullet\mathbf{x}} = i\mathbf{k}(\mathbf{k} \bullet \mathbf{P} - \mathbf{P}k^2) e^{i\mathbf{k}\bullet\mathbf{x}} \tag{A.46}$$

which follows from the divergence operator. The vorticity itself can be written as

$$\boldsymbol{\omega}(\mathbf{k}, \mathbf{x}) = \boldsymbol{\Omega}(\mathbf{k}) e^{i\mathbf{k}\bullet\mathbf{x}}. \tag{A.47}$$

Using eq. (A.46)

$$\boldsymbol{\Omega}(\mathbf{k}) = i(\mathbf{k}(\mathbf{k} \bullet \mathbf{P}) - \mathbf{P}k^2) \tag{A.48}$$

and taking the cross product with k yields

$$\mathbf{k} \times \boldsymbol{\Omega} = -ik^2 \mathbf{k} \times \mathbf{P} = -ik^2 \mathbf{Q}. \tag{A.49}$$

This provides two relations between the Fourier components of vorticity and velocity

$$\boldsymbol{\Omega} = i\mathbf{k} \times \mathbf{Q} \tag{A.50}$$

$$\mathbf{Q} = i\mathbf{k} \times \boldsymbol{\Omega} / k^2 \tag{A.51}$$

Using Cauchy's result of the fluid deformation tensor the upstream and downstream vorticity is

$$\boldsymbol{\Omega}_i^d = \boldsymbol{\Omega}_j^u \frac{\delta X_i}{\delta x_j} \tag{A.52}$$

where $\frac{\delta X_i}{\delta x_j}$ is given by eq. (3.12). This can be used since vorticity lines follow material lines.

First, define vectors $\hat{e}_1^{d,u}$, $\hat{e}_2^{d,u}$, $\hat{e}_3^{d,u}$ along $\boldsymbol{\Omega}^{d,u}$, $\mathbf{Q}^{d,u}$ and $\mathbf{k}^{d,u}$. The relation for $\hat{e}_1^{d,u}$ follows directly from eq. (3.11). Let $\mathbf{f_1}$ define the direction of $\hat{e}_1^u$, then

$$(f_1^u)_i = (e_1^d)_j \frac{dX_i}{dx_j}, \quad (e_1^u) = \frac{\mathbf{f_1^u}}{|\mathbf{f_1^u}|} \tag{A.53}$$

where i, j indicate the components of the respective vectors.

To find $\hat{e_2^u}$ define

$$(f_2^u)_i = (e_2^d)_j \frac{dX_i}{dx_j}. \tag{A.54}$$

Now, since an orthogonal system has to be formed

$$\hat{e_3^u} = \hat{e_1^u} \times \mathbf{f_2^u} / |\hat{e_1^u} \times \mathbf{f_2^u}|. \tag{A.55}$$

Subsequently,

$$\hat{e_2^u} = \hat{e_3^u} \times \hat{e_1^u}. \tag{A.56}$$

Note that first $\hat{e_3^u}$ was found and afterwards $\hat{e_2^u}$. The reason is that $\mathbf{f_2^u}$ is not necessarily orthogonal to $\hat{e_1^u}$, but it does define a plane between $\hat{e_2^u}$ and $\mathbf{f_2^u}$ to which $\hat{e_3^u}$ must be orthogonal. Then, $\hat{e_2^u}$ is in turn orthogonal to $\hat{e_3^u}$ and $\hat{e_1^u}$.

Now define

$$k^u = 2\pi/\lambda^u, \quad k^d = 2\pi/\lambda^d \tag{A.57}$$

for which $\mathbf{k^d}$ and $\mathbf{k^u}$ are by definition parallel to $\hat{e_3^d}$ and $\hat{e_3^u}$, respectively. Consider a vector $\lambda^d \hat{e_3^d}$. If the begin is on a wave crest of the wavevector, then the end is as well, see fig. A.4. The corresponding upstream vector begins on and ends on the same crest, but does not have to have the shortest distance. Denote the upstream vector by $\mathbf{h_3^u}$ then

$$(h_3^u)_i = \lambda^d (e_3^d)_j \frac{dX_i}{dx_j}. \tag{A.58}$$

The component of $\mathbf{h_3^u}$ in the direction of $\hat{e_3^u}$ has the same length as λ^u so

$$\lambda^u = \mathbf{h_3^u} \bullet \hat{e_3^u} = \lambda^d (e_3^u)_i (e_3^d)_j \frac{dX_i}{dx_j}. \tag{A.59}$$

Using eq. (A.57) the relation between the magnitude of the upstream and downstream wavenumber can be determined

$$\frac{k^d}{k^u} = (e_3^u)_i (e_3^d)_j \frac{dX_i}{dx_j}. \tag{A.60}$$

The above relation can be used to determine the velocity magnitude relation as

$$Q_i^u(\mathbf{k}^u) = Q^d(\mathbf{k}^d) f_1^u(e_2^u) \frac{k^d}{k^u}. \tag{A.61}$$

Here, $Q^d(\mathbf{k}^d)$ is the magnitude of vector $\mathbf{Q^d}$ and $Q_i^u(\mathbf{k}^u)$ the i^{th} vector component of the upstream velocity vector.

A.8. Lift response function

The derivation of the lift response function is repeated from Amiet [7][2]. For an airfoil between $-1 < \bar{x} = x/b < 1$

$$g(x, \bar{K_x}, 0, M) = \frac{1}{\pi\beta} \sqrt{\frac{1-\bar{x}}{1+\bar{x}}} S(\bar{K_x}) e^{i\bar{K_x}(M^2\bar{x} + f(M))} \tag{A.62}$$

where $f(M) = (1-\beta)ln(M) + \beta ln(1+\beta) - ln(2)$. Here, $K_x^* = Kx/\beta^2$ and $S(K)$ Sears' function. An itterative procedure is followed to satisfy the leading and trailing edge boundary condtions. The first two terms are

$$g_1(x, \bar{K_x}, 0, M) = \frac{1}{\pi\sqrt{\pi(1+M)\bar{K_x}(1+\bar{x}}} e^{-i\theta_3 \Xi} \tag{A.63}$$

$$g_2(x, \bar{K_x}, 0, M) = \frac{1}{\pi\sqrt{2\pi(1+M)\bar{K_x}}} [(1+i)E(2\bar{\mu}(1-\bar{x})) - 1] e^{-i\theta_3 \Xi}. \tag{A.64}$$

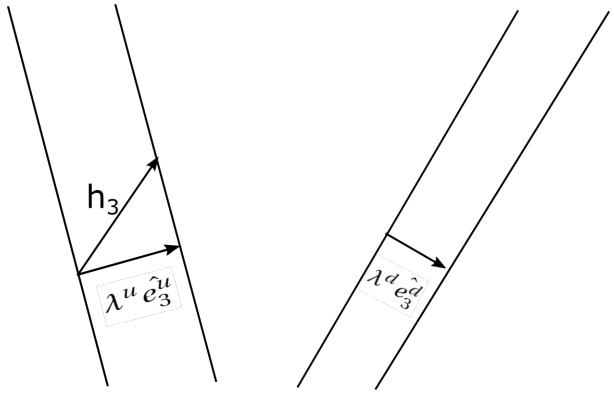

Figure A.4: Caption

In eq. (A.63) and eq. (A.64) $\Xi = \bar{\mu}(1-M)(1+\bar{x}) + \pi/4 - \bar{K_x}$ and $E(x) = \frac{1}{\sqrt{2\pi}} \int_0^x e^{-i\xi} \frac{d\xi}{\sqrt{\xi}}$.
These hold for parallel gusts ($k_y = 0$) and can be related to non-parallel gusts using

$$g(x, \bar{K_x}, \bar{K_y}, M) = \frac{\beta_\infty}{\beta} g(x, \bar{K_x}, 0, M) e^{ixK_y^2/K_x} \tag{A.65}$$

.

Casting eq. (A.65) into eq. (A.11) gives the expressions in eq. (3.27) and eq. (3.28).

A.9. RDT Magnitude Analysis

An order of magnitude analysis, adopted from Hunt [43], is now presented to see why small lengthscales are indeed not affected by the blocking and why large lengthscales are not affected by the mean flow.

Suppose an eddy with velocity $\mathbf{u}'_\infty$, vorticity ω'_∞ and length l moves with the mean flow. If $l \geq R_{le}$, then the change in ω' occurs within a distance of $\sim a$. So, $|\mathbf{u}^{(\mathbf{d})}| \sim |a\omega'_\infty|$. On the other hand, if $l << a$ then these changes occur over a distance l implying $|\mathbf{u}^{(\mathbf{d})}| \sim |l\omega'_\infty|$. The freestream disturbance $\mathbf{u}'^\infty \sim |l\omega'_\infty$ (see Biot-Savart law of induced velocity), so

$$\frac{|\mathbf{u}^{(\mathbf{d})}|}{\mathbf{u}'^\infty} \sim \frac{a}{l}, \quad l \geq a \tag{A.66}$$

$$\frac{|\mathbf{u}^{(\mathbf{d})}|}{\mathbf{u}'^\infty} \sim 1, \quad l \ll a \tag{A.67}$$

which shows that for large l $\mathbf{u}^{(\mathbf{d})}$ is negligible with respect to $\mathbf{u}'^\infty$.

On the other hand, there is the boundary condition that the turbulent velocity normal to the body equals 0. Such a boundary condition can be satisfied mathematically by describing a set of sources on the body. Since these sources give rise to $\mathbf{u}'^{\mathbf{b}}$ in eq. (3.10) and they oppose $\mathbf{u}'^\infty$, they will be of order $\sim |\mathbf{u}'^\infty|$. Then, from eq. (3.10) it can be derived that

$$\mathbf{u}'^{\mathbf{b}} \gg \mathbf{u}'^{\mathbf{d}}, \quad l \gg a \tag{A.68}$$

$$\mathbf{u}'^{\mathbf{b}} \sim \mathbf{u}'^{\mathbf{d}}, \quad l \ll a \tag{A.69}$$

. So for lengthscales large with respect to the body, the blocking effect is dominant and the mean flow distortion can be neglected. For lengthscales small with respect to the body, is of the same order as the mean flow distortion of vorticity. But since the source velocity caused by the boundary decays as $\sim e^{-k\Xi}$, where Ξ is the non-dimensional distance to the body, this effect can be neglected for most of the flow.

Hunt [43, 45] developed the analogy that leading edge distortion can be viewed as turbulence approaching a two-dimensional round body. This circle represents the leading edge radius and thereby the interaction of turbulence with an airfoil is modelled. As said, two main distortion mechanisms are identified. The blocking one is obvious whereas the vorticity distortion is less trivial. Therefore, the latter is explained in more detail with the aid of fig. A.5.

It is known that vorticity follows material lines. Suppose a set of material lines $d\mathbf{l}_{1,2,3}$ is convected towards the leading edge along the stagnation streamline. As the leading edge is approached, $d\mathbf{l}_1$ is compressed

wheareas $d\mathbf{l}_3$ is elongated. Following Stokes' theorem and Kelvin's law, it must be that the vorticity is increased in the direction of $d\mathbf{l}_1$. Similarly, the vorticity in the direction of $d\mathbf{l}_2$ is decreased. In the analysis, the spanwise vorticity following $d\mathbf{l}_3$ remains unaltered. Now, the vorticity in the direction of $d\mathbf{l}_i$, $d\boldsymbol{\omega}_i$ induces velocity fluctuations in the perpendicular directions. That is, in the directions of $d\mathbf{l}_{j,k}$. In this way, the upwash velocity fluctuations, which generate the unsteady loading noise, are altered. This effect is significant for scale small with respect to the object i.e. leading edge radius and tends to decrease the upwash fluctuations.

Although the above analogy used a solid body, the same holds for the streamtube contraction which is explained in section 3.3.1. That is, the small lengthscale analysis is based on the change in vorticity due to the mean flow lines. It does not matter how the change in flow lines is established, so it is equally valid for the streamtube contraction.

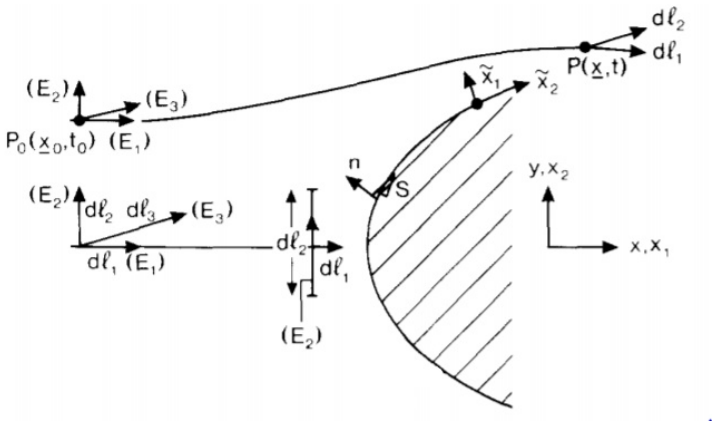

Figure A.5: Distortion of material lines which translates to a change in vorticity.

B

Supplementary calculations

B.1. Deformation tensor

The deformation tensors coming from PIV, H&O ($T/T_{exp} = 1$) and H&O ($T/T_{exp} = 0.52$) are used to determine the principle strains at $r/R = 0.4$. These are 1.25, 1.27 and 1.64 in the z-direction,respectively. Clearly, the original form of Hough and Ordway overpredicts the elongation of the material lines. As a sanity check the determinants are determined. These are 0.993, 1.0008 and 0.96 for $T/T_{exp} = 0.52$, $T/T_{exp} = 1$ and PIV respectively. The PIV shows a slight deviation from 1 which is ascribed to the fact that the PIV streamlines are derived from experimental data wheareas the other two follow directly from a smooth velocity field.

$$\mathbf{F_{PIV}} = \begin{bmatrix} 1.15 & 0 & 0 \\ -0.006 & 1.23 & -0.12 \\ -0.07 & 0.09 & 0.67 \end{bmatrix} \quad \mathbf{F_1} = \begin{bmatrix} 1.37 & 0 & 0 \\ 0.003 & 1.63 & -0.029 \\ -0.028 & 0.11 & 0.45 \end{bmatrix} \quad \mathbf{F_{0.52}} = \begin{bmatrix} 1.17 & 0 & 0 \\ 0.007 & 1.27 & -0.007 \\ -0.03 & 0.015 & 0.66 \end{bmatrix} \tag{B.1}$$

B.2. Spatial lengthscale computation

For every z/R at a specific r/R, the average $R_{ij}(\delta m)$ is computed for a band $[r/R - \Delta r/R, r/R + \Delta r/R]$. See fig. B.1 for a schematic overview of the procedure as well as a typical average correlation graph. As can be seen the average correlation is determined for the lines in the bandwidth. Using the mean line the point is found such that $R_{uu}(\delta z) = 0.37$.

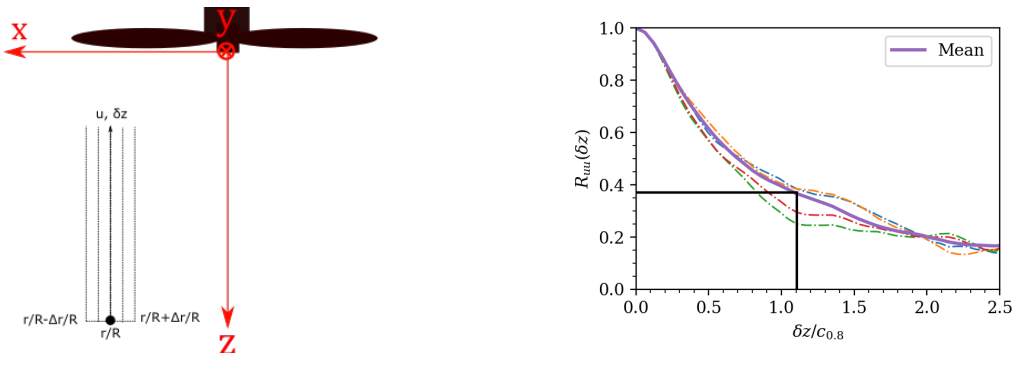

(a) (b)

Figure B.1: (a) A point at $[r/R, z/R]$ with band $\Delta r/R$ for which $R_{uu}(\delta z)$ is calculated. (b) The individual spatial corerlation curves and the resulting mean. The lengthscale is determined by finding $\delta z/c_{0.8}$ such that the mean $R_{uu}(\delta z) = 0.37$

C

Verification of noise model

The authors of the noise model provided a sample calculation which can be used to verify the code. In fig. C.1 the sample calculation is denoted with verification and compared with the code written during this thesis. Good agreement is found. The small differences can be ascribed to rounding errors as at the time of publication of [8]. The software at that time did ,for example, model π as 3.1415 whereas now Python estimates π up to 17 digits. Analogously for the trigonometric functions.

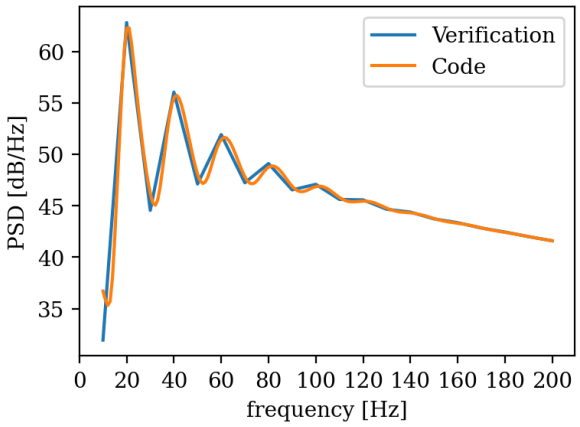

Figure C.1: Sample calculation from [8] (verification) compared with code

Bibliography

[1] F. Al-Turjman. *Unmanned Aerial Vehicles in Smart Cities*. Springer Nature Switzerland AG, Cham, Switzerland, 2020.

[2] R.K. Amiet. Compressibility effects in unsteady thin-airfoil theory. *AIAA Journal*, 12(2):252–255, 1974.

[3] R.K. Amiet. Frame of reference considerations for the forward flight noise problem. Technical Report N212775-1, United Technologies Research Center, East Hartford, CT, November 1974.

[4] R.K. Amiet. Acoustic radiation from an airfoil in a turbulent stream. *Journal of Sound and Vibration*, 41: 407–420, 1975.

[5] R.K. Amiet. Noise produced by turbulent flow into a propeller or helicopter rotor. In *Proceedings of the 3rd AIAA Aero-Acoustics Conference*, 1976.

[6] R.K. Amiet. Noise due to rotor-turbulence interaction. Technical Report 19780024880, United Technologies Research Center, East Hartford, CT, 1978.

[7] R.K. Amiet. Noise produced by turbulent flow into a rotor: Theory manual for noise calculation. Technical Report NASA-CR-181788, National Aeronautics and Space Administration, East Hartford, CT, June 1989.

[8] R.K. Amiet, C.G. Egolf, and J.C. Simonich. Noise produced by turbulent flow into a rotor: Users manual for noise calculation. Technical Report NASA-CR-181790, National Aeronautics and Space Administration, East Hartford, CT, June 1989.

[9] R.K. Amiet, J.C. Simonich, and R.H. Schlinker. Rotor noise due to atmospheric turbulence ingestion - part 2: Aeroacoustic results. *Journal of Aircraft*, 27(1):15–22, 1990.

[10] J.D. Anderson. *Fundamentals of Aerodynamics*. McGraw-Hill Education, 2 Penn Plaza, New York, 2011.

[11] K.S. Aravamudan and W.L. Harris. Low-frequency broadband noise generated by a model rotor. *Journal of Acoustic Society of America*, 66(2):522–533, 1979.

[12] ATI Industrial Automation. *Six-Axis Force/Torque Sensor System installation and operation manual*. ATI Industrial Automation.

[13] G.K. Batchelor. *The Theory of Homogeneous Turbulence*. Press Syndicate of University of Cambridge, Camebridge, NY, USA, 1953.

[14] G.K. Batchelor and I. Proudman. The effect of rapid distortion of a fluid in turbulent motion. *Quarterly Journal of Mechanics and Applied Mathematics*, 7:83–103, 1954.

[15] S. Baur and M. Hader. Cargo drones the future of parcel delivery. https://www.rolandberger.com/en/Point-of-View/Cargo-drones-The-future-of-parcel-delivery.html. Accessed: 5/9/2020.

[16] P.W. Bearman. Corrections for the effect of ambient temperature drift on hotwire measurements in incompressible flows. *DISA information*, 11:25–30, 1971.

[17] K. Brentner and F. Farassat. Modeling aerodynamically generated sound of helicopter rotors. *Progress in Aerospace Sciences*, 39(2):83 – 120, 2003.

[18] R.E. Britter, J.C.R. Hunt, and J.C. Mumford. The distortion of turbulence by a circular cylinder. *Journal of Fluid Mechanics*, 92(2):269 – 290, 1979.

[19] D. Casalino, E. Grande, G. Romani, D. Ragni, and F. Avallone. Definition of a benchmark for low reynolds number propeller aeroacoustics. *Aerospace Science and Technology*, 113, 2021.

[20] A.W. Christian and R. Cabell. Initial investigations into the psychoacoustic properties of small unmanned aerial system noise. In *Proceedings of the 23rd AIAA/CEAS Aeroacoustics Conference*, 2017.

[21] J. Christophe. *Application of Hybrid Methods to High Frequency Aeroacoustics*. PhD thesis, Von Karman Institute of Fluid Mechanics, Rhode-St-Genese, Belgium, 2011.

[22] J.M. Cimbala and W.J. Park. A direct hot-wire calibration technieque to account for ambient temperature drift in incompressible flow. *Experiments in Fluids*, 8:299–300, 1990.

[23] P.A. Davidson. *Turbulence: An Introduction for Scientists and Engineers*. Oxford University Press, New York, first edition, 2004.

[24] *Ö*. Ertunç, N. *Ö*zyilmaz, H. Lienhart, F. Durst, and K. Beronov. Homogeneity of turbulence generated by static-grid structures. *Journal of Fluid Mechanics*, 654:473 – 500, 210.

[25] L.D. de Santana. *Semi-analytical methodologies for airfoil noise prediction*. PhD thesis, KU Leuven, Leuven, Belgium, 2015.

[26] European Aviation Safety Agency. Introduction of a regulatorty framework for the operation of unmanned aircraft. https://www.easa.europa.eu/, 2021. Online; accessed 3 June 2021.

[27] M. Falchi and G.P. Romano. Evaluation of the performance of high-speed piv compared to standard piv in a turbulent jet. *Exp. Fluids*, 47(3):509–526, 2009.

[28] A.M. Faria, J.Y. Saab Jr., S. Rodriguez, and M. de Mattos Pimenta. A rapid distortion theory-based airfoil turbulent inflow noise prediction method. *Journal of the Brazilian Society of Mechanical Sciences and Engineering*, 42(397), 2020.

[29] W.R. Finley. Noise in induction motors - causes and treatments. *IEEE Transactions on Industry Applications*, 27(6):1204–1213, 1991.

[30] F. Gae-Aguilera, R. Karve, J. Gill, X. Zhang, and D. Angland. On the effects of anisotropic turbulence on leading edge noise. *Journal of Sound and Vibration*, 495, 2020.

[31] A.R. George. Helicopter noise: State-of-the-art. *Journal of Aircraft*, 15(11):707–715, 1978.

[32] A.R. George and S.T. Chou. Comparison of broadband noise mechanisms, analyses and experiments on rotors. *Journal of Aircraft*, 21(8):583 – 592, 1984.

[33] A.R. George and Y.N. Kim. High-frequency broadband rotor noise. In *Proc. of 3rd AIAA Aero-Acoustics Conference*. American Institute of Aeronautics and Astronautics, 1976.

[34] S. Glegg and W. Devenport. *Aeroacoustics of Low Mach Number Flows*. Elsevier, San Diego, CA, 2017.

[35] S. Goldstein. On the vortex theory of screw propellers. In *Proceedings of the Royal Society of London*, 1929.

[36] J.M.R. Graham. Similarity rules for thin aerofoils in non-stationary subsonic flows. *Journal of Fluid Mechanics*, 43:753–766, 1970.

[37] J.M.R. Graham. Rapid distortion of turbulence into an open turbine rotor. *Journal of Fluid Mechanics*, 825(1):764–794, 2017.

[38] E. Grande, G. Romani, D. Ragni, F. Avallone, and D. Casalino. Aeroacoustic investigation of a propeller operating at low-reynolds numbers. unpublised, 2021.

[39] Martin J. Hagen, Gloria K. Yamauchi, David B. Signor, and Marianne Mosher. Measurements of atmospheric turbulence effects on tail rotor acoustics. *NASA Technical Memorandum*, 1994.

[40] Donald B. Hanson. Spectrum of rotor noise caused by atmospheric turbulence. *The Journal of the Acoustical Society of America*, 56(1):110–126, 1974.

[41] H.O. Hinze. *Turbulence*. McGraw-Hill, New York, NY, 1975.

[42] G.R. Hough and D.E. Ordway. The generalized actuator disk. In *Proceedings of the Second Southeastern Conference on Theoretical and Applied Mechanics*. Therm Advanced Research, Inc., 1964.

[43] J.C.R. Hunt. A theory of turbulent flow round two-dimensional bluff bodies. *Journal of Fluid Mechanics*, 61(4):625–706, 1973.

[44] J.C.R. Hunt. A theory of turbulent flow round two-dimensional bluff bodies. *Journal of Fluid Mechanics*, 61:625–706, 1973.

[45] J.C.R. Hunt, H. Kawai, S.R. Ramsey, G. Pedrizetti, and R.J. Perkins. A review of velocity and pressure fluctuations in turbulent flows around bluff bodies. *Journal of Wind Engineering and Industrial Aerodynamics*, 35:49–85, 1990.

[46] F.E. Jørgensen. *How to measure turbulence with hotwire enemometers*. Dantec Dynamics, 2002.

[47] T. Von Karman. Progress in the statistical theory of turbulence. In *Proceedings of the National Academy of Sciences*, volume 34, pages 530–539. National Academy of Sciences, 1948.

[48] K.S. Kim, C.M. Lee, G.Y. Hwang, and S.M. Hwang. Effect of the number of poles on the acoustic noise from bldc motors. *Journal of Mechanical Science and Technology*, 25(2):273–277, 2011.

[49] C.F. Matozinhow, G.G.Q. Tomaz, T. Nguyen, and Y. Hassan. Experimental investigation of turbulent flow characteristics in cross-flow planes of a 5x5 rod bundle with a space grid. *Internation Journal of Heat and Fluid Flow*, 87, 2021.

[50] V. Mugundhan, R.S. Pugazenthi, N.B. SPeirs, R. Samtaney, and S.T. Thoroddsen. The alignment of vortical strucutres in turbulent flow through a contraction. *Journal of Fluid Mechanics*, 884:A51 – A536, 20250.

[51] C.W. Murray and D. Andersono. A cfd-based procedure for airspace integration of small unmanned aircraft within congested areas. *International Journal of Micro Air Vehicles*, 9(4):235–252, 2017.

[52] Clement Nardari, Damiano Casalino, Frencesco Polidoro, Vedran Coralic, Johnd Brodie, and Phoi-Tack Lew. Numerical and experimental investigations of flow confinement effects on uav rotor noise. In *Proceedings of the 25th AIAA/CEAS Aeroacoustics Conference*. American Institure of Aeronautics and Astronautics, 2019.

[53] T. Nguyen and Y. Hassan. Stereoscopic particle image velocimetry meassurements of flow in a rod bundle with a spacer grid and mixing vanes at a low reynolds number. *Int. J. Heat Fluid Flow*, 67:202–219, 2017.

[54] X. Oliver and C. Agelet de Saracibar. *Continuum Mechanics for Engineers. Theory and Problems*. UPC/BarcelonaTech, Barcelona, 2017.

[55] R.W. Paterson and R.K. Amiet. Noise of a model helicopter rotor due to ingestion of turbulence. Technical Report NASA-CR-3214, National Aeronautics and Space Administration, East Hartford, CT, November 1979.

[56] M. Raffel, C.E. Willert, and J. Kompenhause. *Unmanned Aerial Vehicles in Smart Cities*. Springer-Verlag Berlin Heidelberg New York, Heidelberg, Germany, 1998.

[57] P.E. Roach. The generation of nearly isotropic turbulence by means of grids. *International Journal of Heat and Fluid Flow*, 8:82–92, 1986.

[58] R.A.V. Robinson. *Turbulence Ingestion Noise of Open Rotors*. PhD thesis, University of Cambridge, Cambridge, UK, October 2011.

[59] G.P. Romano. Analysis of two-point velocity measurements in near-wall flows. *Experimental Fluids*, 20 (2):68–83, 1995.

[60] L.D. Santana, J. Christophe, C. Schram, and W. Desmet. A rapid distortion theory modified turbulence spectra for semi-analytical airfoil noise prediction. *Journal of Sound and Vibration*, 383:349–363, 2016.

[61] D.F. Scharpf and T.J. Mueller. An experimental investigation of the sources of propeller noise due to the ingestion of turbulence at low speeds. *Experiments in Fluids*, 18:277–287, 1995.

[62] A. Sciacchitano and B. Wieneke. Piv uncertainty propagation. *Measurement Science and Technology*, 27, 2016.

[63] M. Sevik. Sound radiation from a subsonic rotor subjected to turbulence. *Fluid Mechanics, Acoustics and Design of Turbomachinery*, 34(2):493–512, 1974.

[64] H. Shakhatreh, A. H. Sawalmeh, A. Al-Fuqaha, Z. Dou, E. Almaita, I. Khalil, N. S. Othman, A. Khreishah, and M. Guizani. Unmanned aerial vehicles (uavs): A survey on civil applications and key research challenges. *IEEE Access*, 7:48572–48634, 2019.

[65] R.K. Shenoy, F.W. Kohlhepp, and K.P. Leighton. Acoustic characteristics of 1/20-scale model helicopter rotors. Technical Report NASA-CR-177355, Sikorsky Aircraft, East Hartford, CT, August 1986.

[66] J.C. Simonich, R.K. Amiet, R.H. Schlinker, and E.M. Greitzer. Rotor noise due to atmospheric turbulence ingestion - part 1: Fluid mechanics. *Journal of Aircraft*, 27(1):7–13, 1990.

[67] John C. Simonich, Roy K. Amiet, Robert H. Schlinker, and Edward M. Greitzer. Helicopter rotor noise due to ingestion of atmospheric turbulence. Technical Report NASA-CR-3973, National Aeronautics and Space Administration, East Hartford, CT, May 1986.

[68] S. Sinayoko, M. Kingan, and A. Agarwal. Trailing edge noise theory for rotating blades in uniform flow. *Proceedings of the royal society*, 469, 2013.

[69] J.K. Staubs. *Real Airfoil Effects on Leading Edge Noise*. PhD thesis, Virginia Polytechnic Institue and State University, Blacksburg, Virginia, May 2008.

[70] James H. Stephenson, Daniel Weitsman, and Nikolas S. Zawodny. Effects of flow recirculation on unmanned aircraft system acoustic measurements in closed anechoic chambers. *Journal of Acoustical Society of America*, 145(3):1153–1155, 2019.

[71] S. Sunada, K. Ozaki, M. Tanaka, T. Yasuda, K. Yasuda, and K. Kwachi. Airoil characteristics at a low reynolds number. *Journal of Flow Visualization and Image processing*, 164:476–490, 1938.

[72] G.I. Taylor. The spectrum of turublence. *Proceedings of the rotyal society A: Mathematical, Physical and Engineering Scieces*, 7(3), 2000.

[73] N. van Arnhem, R. de Vries, T. Sinnige, R. Vos, and L.L.M. Veldhuis. Aerodynamic performance and static stability characteristics of aircraft with tail-mounted propellers. Journal of Aircraft (accepted manuscript), 2021.

[74] J. Westerweel. Fundamentals of digital particle image velocimetry. *Measurement Science and Technology*, 8(12), 1997.

[75] J. Winslow, H. Otsuka, B. Govindarajan, and I. Chopra. Basic understanding of airfoil charactereistics at low reynolds numbers. *Journal of Aircraft*, 55(3):1–12, 2017.

[76] John P. Wojno, Thomas J. Mueller, and William K. Blake. Turbulence ingestion noise, part 1: Experimental characterisation of grid-generated turbulence. *AIAA Journal*, 40(1):16–25, 2002.

[77] Yendrew Yauwenas, Jeoffrey Fischer, Danielle Moreau, and Con Doolan. The effect of inflow disturbance on drone propeller noise. In *Proc. of 25th AIAA/CEAS Aeroacoustics Conference*. AIAA, 2019.

[78] J. Yin and A. Stuermer. Noise radiation from installed pusher propeller using coupling of unsteady panel method, actuator disk and fw-h methodology. In *Proc. of 16th AIAA/CEAS Aeroacoustics Conference*. AIAA, 2010.

[79] R. Zamponi, S. Satcunanathan, S. Moreau, D. Ragni, M. Meinke, W. Schroder, and C. Schram. On the role of turbulence distortion on leading-edge noise reduction by means of porosity. *Journal of Sound and Vibration*, 485, 2020.

[80] Nikolas S. Zawodny, D. Douglas Boyd Jr., and Casey L. Burley. Acoustic chracterization and prediciotn of representative, small-scale rotary-wing unmanned aircraft system components. In *Proc. of 72nd American Helicopter Society International Annual Forum 2016*. American Helicopter Society, 2016.